TECHNICAL REPORT STANDARD PAGE

1. Title and Subtitle
   Quality Management of Cracking Distress Survey in Flexible Pavements Using LTRC Digital Highway Data Vehicle
2. Author(s)
   Zhong Wu and Mostafiz Emtiaz
3. Performing Organization Name and Address
   Louisiana Transportation Research Center
   4101 Gourrier Avenue
   Baton Rouge, LA 70808
4. Sponsoring Agency Name and Address
   Louisiana Department of Transportation and Development
   P.O. Box 94245
   Baton Rouge, LA 70804-9245
5. Report No.
   FHWA/LA.21/659
6. Report Date
   March 2022
7. Performing Organization Code
   LTRC Project Number: 16-6P
   SIO Number: DOTLT1000107
8. Type of Report and Period Covered
   Final Report
   April 2016 – September 2021
9. No. of Pages
   125
10. Supplementary Notes
    Conducted in Cooperation with the U.S. Department of Transportation, Federal Highway Administration
11. Distribution Statement
    Unrestricted. This document is available through the National Technical Information Service, Springfield, VA 21161.
12. Key Words
    PMS/Pavement Condition Survey, Cracking index, Automated Survey, Manual Survey, Accuracy
13. Abstract

The Louisiana Department of Transportation and Development (DOTD) began to collect its Pavement Management System (LA-PMS)'s pavement condition data using a vendor's 3D automatic system in 2017. For each 0.1-mile subsection on a flexible pavement, the vendor's 3D automated cracking data reported in LA-PMS consists of various cracking amounts in terms of the alligator, longitudinal, and transverse cracks at different severity levels (e.g., low, medium, and high). The objectives of this study include two-folds: (1) to evaluate and assess the accuracy and precision of the 3D automated cracking data on flexible pavements through comparison with manual measurements on high-resolution pavement images; (2) to develop an image analysis application in pavement cracking identification on high-resolution pavement images collected by the Louisiana Transportation Research Center (LTRC)'s high-speed data vehicle. To achieve these objectives, a comprehensive manual cracking survey based on the DOTD's distress identification protocol was conducted on twenty-three flexible pavement sections (totally 28.6 miles long) and nine 0.5-mile calibration sites, using the vendor's high-resolution pavement images collected during the 2017 DOTD's pavement condition data collection cycle. By directly

comparing the manual measurements and the 2017 reported cracking data in LA-PMS, results indicated that the automated cracking measurements based on 0.1-mile long sections tend to over-estimate the medium severity level of cracking amounts for all flexible pavement crack types (alligator, longitudinal, and transverse). However, when the automated cracking measurements were re-grouped based on 50-ft. long subsections, the overall estimation errors without differentiating the cracking severity levels could be significantly reduced due to a smaller standard deviation of the measurement errors and a shorter section length. Based on 50-ft. subsections, false positive errors produced by the automated system were found to be 8.5%, 9.8%, and 8.8% for alligator, longitudinal, and transverse cracking, respectively and the corresponding missed crack errors were 5.0%, 7.9%, and 1.4% respectively in this study. Statistical tests based on the mean measurement errors and equality of variance were conducted to qualitatively evaluate the accuracy and precision of the collected cracking data. In general, based on 50-ft. subsections, the automated system could produce significantly accurate results for high severity transverse cracking and significantly precise results for low severity alligator cracking. On the other hand, based on 0.1-mile subsections, the automated system was found not able to produce significantly accurate estimation of pavement cracking at different severity levels but provide significantly precise cracking measurements at low severity levels for all crack types. Since the overall results indicated that the 3D automated cracking measurements were statistically different from the manual measurements, which possibly led to a smaller cracking index estimation and different treatment selection, an artificial neural network (ANN) model was developed using the cracking measurements in this study. The ANN model aimed at adjusting the automated cracking measurements towards the manual cracking measurements at a 0.1-mile interval used in the LA-PMS, specifically for the flexible pavement cracking measurement data found in 2017 LA-PMS database. Finally, a MATLAB-based imaging analysis computer program was developed to generate an automated cracking report from high-resolution 2D pavement images collected by LTRC.

Project Review Committee

Each research project will have an advisory committee appointed by the LTRC Director. The Project Review Committee is responsible for assisting the LTRC Administrator or Manager in the development of acceptable research problem statements, requests for proposals, review of research proposals, oversight of approved research projects, and implementation of findings.

LTRC appreciates the dedication of the following Project Review Committee Members in guiding this research study to fruition.

LTRC Administrator/Manager

Zhongjie "Doc" Zhang, Ph.D., P.E.
Pavement and Geotechnical Research Manager

Members

Christophe Fillastre
Ashley Horne
Patrick Icenogle
Jeff Lambert
Xingwei Chen
Mark Chenevert
Mark Kelley, District 61
Arturo Aguirre, FHWA

Directorate Implementation Sponsor

Christopher P. Knotts, P.E.
DOTD Chief Engineer

Quality Management of Cracking Distress Survey in Flexible Pavements Using LTRC Digital Highway Data Vehicle

By
Zhong Wu
Mostafiz Emtiaz

Louisiana Transportation Research Center
4101 Gourrier Avenue
Baton Rouge, LA 70808

LTRC Project No. 16-6P
SIO No. DOTLT1000107

conducted for

Louisiana Department of Transportation and Development
Louisiana Transportation Research Center

March 2022

Abstract

The Louisiana Department of Transportation and Development (DOTD) began to collect its Pavement Management System (LA-PMS)'s pavement condition data using a vendor's 3D automatic system in 2017. For each 0.1-mile subsection on a flexible pavement, the vendor's 3D automated cracking data reported in LA-PMS consists of various cracking amounts in terms of the alligator, longitudinal, and transverse cracks at different severity levels (e.g., low, medium, and high). The objectives of this study include two-folds: (1) to evaluate and assess the accuracy and precision of the 3D automated cracking data on flexible pavements through comparison with manual measurements on high-resolution pavement images; (2) to develop an image analysis application in pavement cracking identification on high-resolution pavement images collected by the Louisiana Transportation Research Center (LTRC)'s high-speed data vehicle.

To achieve these objectives, a comprehensive manual cracking survey based on the DOTD's distress identification protocol was conducted on twenty-three flexible pavement sections (totaling 28.6 miles long) and nine 0.5-mile calibration sites, using the vendor's high-resolution pavement images collected during the 2017 DOTD's pavement condition data collection cycle. By directly comparing the manual measurements and the 2017 reported cracking data in LA-PMS, results indicated that the automated cracking measurements based on 0.1-mile long sections tend to over-estimate the medium severity level of cracking amounts for all flexible pavement crack types (alligator, longitudinal, and transverse). However, when the automated cracking measurements were re-grouped based on 50-ft. long subsections, the overall estimation errors without differentiating the cracking severity levels could be significantly reduced due to a smaller standard deviation of the measurement errors and a shorter section length. Based on 50-ft. subsections, false positive errors produced by the automated system were found to be 8.5%, 9.8%, and 8.8% for alligator, longitudinal, and transverse cracking, respectively and the corresponding missed crack errors were 5.0%, 7.9%, and 1.4%, respectively in this study. Statistical tests based on the mean measurement errors and equality of variance were conducted to qualitatively evaluate the accuracy and precision of the collected cracking data. In general, based on 50-ft. subsections, the automated system could produce significantly accurate results for high severity transverse cracking and significantly precise results for low severity alligator cracking. On the other hand, based on 0.1-mile subsections, the automated system was found not able to produce significantly accurate estimation of pavement cracking at different

severity levels but provide significantly precise cracking measurements at low severity levels for all crack types. Since the overall results indicated that the 3D automated cracking measurements were statistically different from the manual measurements, which possibly led to a smaller cracking index estimation and different treatment selection, an artificial neural network (ANN) model was developed using the cracking measurements in this study. The ANN model aimed at adjusting the automated cracking measurements towards the manual cracking measurements at a 0.1-mile interval used in the LA-PMS, specifically for the flexible pavement cracking measurement data found in 2017 LA-PMS database. Finally, a MATLAB-based imaging analysis computer program was developed to generate an automated cracking report from high-resolution 2D pavement images collected by LTRC.

Acknowledgments

This study was funded by the Louisiana Transportation Research Center (LTRC Project No. 16-6P) and the Louisiana Department of Transportation and Development (DOTD) (SIO No. DOTLT1000107). The authors would like to express thanks to all those who provided valuable help in this study. Specifically, Christophe Fillastre and Angella Murrell from DOTD provided great help in understanding DOTD's PMS system and data collection. Mitchell Terrell and Terrell Gorham from LTRC collected the additional pavement cracking data using LTRC's digital highway data vehicle.

Implementation Statement

The results of this study demonstrated the potential improvement in data quality and accuracy in the flexible pavement cracking survey in Louisiana. The findings of the research can be implemented in making a reliable and cost-effective project selection and budget allocation for pavement maintenance and rehabilitation. The more accurate pavement cracking data can be also used in the local-calibration of the Pavement ME's load-induced cracking models currently implementing in DOTD and the project-level cracking distress evaluation analysis by researchers.

- For DOTD's 2017 LA-PMS database, the developed ANN model may be used in adjusting the existing cracking measurements including the alligator, longitudinal, transverse, and random cracking when the computed cracking indices are to be used for a project's treatment selection. Due to the difference between the LCMS3D and LCMSRange images, cautions shall be taken when the predicted cracking indices are significantly different from the LCMSRange provided results.
- Pavement researchers can use the developed ANN model in obtaining an accuracy-improved cracking data for flexible pavement sections in the 2017 LA-PMS for a pseudo project-level cracking distress evaluation.
- For LTRC's digital highway data vehicle (DHDV) collected 2-D cracking images, the developed MATLAB based software can be used to obtain a pavement cracking classification report at a network level data accuracy. However, further research is still warranted when a project-level cracking data is needed from the DHDV.

Table of Contents

List of Tables

List of Figures

Introduction

The Louisiana Department of Transportation and Development (DOTD) has been using a 3D technology automatic pavement condition survey for its pavement management system (LA-PMS) since 2017. LA-PMS uses a digital highway data collection vehicle to survey the existing pavement conditions every two years for its entire pavement network, in which, for the flexible pavement sections, the collected condition data includes the alligator cracking, longitudinal cracking, transverse cracking, rutting, international roughness index (IRI), and patching data for each 0.1-mile long subsection. While the PMS-collected pavement condition data are commonly used by pavement engineers and managers in making consistent and cost-effective decisions in pavement maintenance and rehabilitation at the network level, more agencies now also consider use of the PMS data in project-level pavement applications, such as the local-calibration of the distress models in the Mechanistic-Empirical pavement design guide (MEPDG) [1-4]. In LA-PMS, the collected pavement condition data are first converted into various distress indices (e.g., alligator index, rutting index, etc.) that can be further used in the pavement treatment selection process based on pre-defined distress trigger values [5].

It is well known that the pavement surface cracking distresses in a network level pavement distress survey are automatically determined from an imaging analysis software using pavement images collected by a digital highway pavement data collection system (or vehicle). Currently, there exists different high-speed pavement image collection systems and image analysis software. Obviously, the accuracy of the automated pavement cracking data in PMS would be largely relied on both the image collection system and the image analysis software selected. McQueen and Timm conducted a study to determine the accuracy of the automated cracking survey for Alabama DOT [6]. It was found that the automated survey under-reported the alligator cracking with the severity of Level 1 (i.e., longitudinal cracking in the wheelpath < 0.28 in. wide), and over-reported the alligator cracking with the severity of Level 3 (i.e., longitudinal cracking in the wheelpath ≥ 0.28 in. wide). The study concluded that the transverse cracking, block cracking, and alligator cracking at all severity levels require greater accuracy. Another study conducted by New Jersey DOT compared the data collected by human raters with those by an automated distress survey equipment [7]. A recent study [8] evaluated three different automated crack detection systems with manual cracking measurements on twenty 550-ft. pavement sections in Texas. The results showed that a large number of false positives and missed cracks were observed between

the manual measurements and those from the three automated systems considered. The false positive indicates that the automatic detection system reports a crack, however, no crack can be detected from manual measurements. Meanwhile, the missed crack refers to an error when the automatic detection system does not report a crack but the crack is detected from manual measurements. This study generally confirms that there still existed a certain degree of inconsistency between the manual and automated cracking measurements under the current state of the practice in high speed data collection technologies. On the other hand, this study also reported that the amount of false positives may be significantly reduced if applying a manual post-processing on the automated cracking measurements. This implies that both the accuracy and quality of the automated cracking measurements may be improved through a manual post-processing procedure.

Due to a concern that using the network level collected PMS distress data in pavement model calibration could potentially affect the future pavement design reliability, this study was focused on the evaluation of the accuracy/precision and possible project level application for the automated cracking data collected in LA-PMS. In addition, Louisiana Transportation Research Center (LTRC) has its own digital highway data vehicle ($DHDV_{LTRC}$) that can collect the pavement condition data including rut depth, IRI, and high resolution pavement images for in-house pavement research purpose. One of the original objectives of this study was to conduct a precision evaluation of the DHDV-collected cracking distresses and use the results to validate the cracking data stored in LA-PMS. However, the accompanying cracking imaging analysis software with the $DHDV_{LTRC}$ became outdated after the start of this research due to a necessary upgrade of the image collection system mounted on the $DHDV_{LTRC}$. Therefore, the scope of this part research had modified and in this report it was considered to develop a MATLAB application for the $DHDV_{LTRC}$ in analyzing the collected 2-D pavement images and provide an automated pavement cracking report.

Literature Review

Manual and Automated Pavement Cracking Distress Identification

The data collection protocols used for the pavement cracking distress classification and measurements in PMS are varied among different state transportation agencies. Currently there exists seven national-level protocols or data collection guidelines for identifying the

pavement cracking distresses in the US. Table 1 provides a list of these pavement cracking collection protocols. Among them, the American Association of State Highway and Transportation Officials (AASHTO) protocols, National Park Service (NPS) protocol, and UK SCANNER protocols can be used in both automated and manual cracking data collection; whereas, the Long-Term Pavement Performance (LTPP) and American Society of Testing Materials (ASTM) protocols can only be applied for a manual pavement cracking survey [9].

Table 1. Cracking protocols at national level summary [9]

Protocol Name	Automated	Types of Pavement	Available Crack Definitions
AASHTO R 85-18	Yes	AC	4
AASHTO R 55-10	Yes	AC	4
ASTM D6433–16 (Highway)	No	AC & PCC	9
ASTM D5340–12 (Airfield)	No	AC & PCC	9
FHWA LTPP	No	AC & JPCP & CRCP	13
FHWA NPS	Yes	All Types	3
UK SCANNER	Yes	All Types	2

The AASHTO R 85-18 and the LTPP protocols are the most used national guidelines by researchers for an automated or manual pavement cracking survey, respectively. In addition, various state agencies have their cracking protocol in place. In the following sections, the LTPP, two AASHTO, and Louisiana pavement cracking distress classification protocols are described in details. Meanwhile, the Mechanistic-Empirical Pavement Design Guide (MEPDG) has its own cracking protocol, which will also be discussed.

LTPP Cracking Protocol

Federal Highway Administration (FHWA) published the “Distress Identification Manual for the Long-Term Pavement Performance Program (Fifth Revised Edition)” to

demonstrate the cracking definitions for the manual survey [10]. The LTPP Distress Identification Manual defines six types of cracking distress in flexible pavements, including fatigue cracking, block cracking, edge cracking, longitudinal cracking, reflection cracking at joints, and transverse cracking. Protocol to identify these six cracking by the manual survey are given below:

Fatigue Cracking: Fatigue cracks occur in the wheel path areas which are under the constant loads of traffic movement. These types of cracking start out as a small series of interconnected fissures and develop different patterns gradually. At each severity level, fatigue cracks are measured in terms of the affected area.

At low severity levels, very few interconnected cracks are visible and there should be no evidence of pumping. Moderate fatigue cracking should show a complete pattern of interconnected cracks and pumping is not evident. If the intense and dense cracks connect to make a complete pattern, then it should be marked as a high severity level of fatigue cracking. In this type of cracking pumping may be evident.

Figure 1. Fatigue cracking protocol (LTPP)

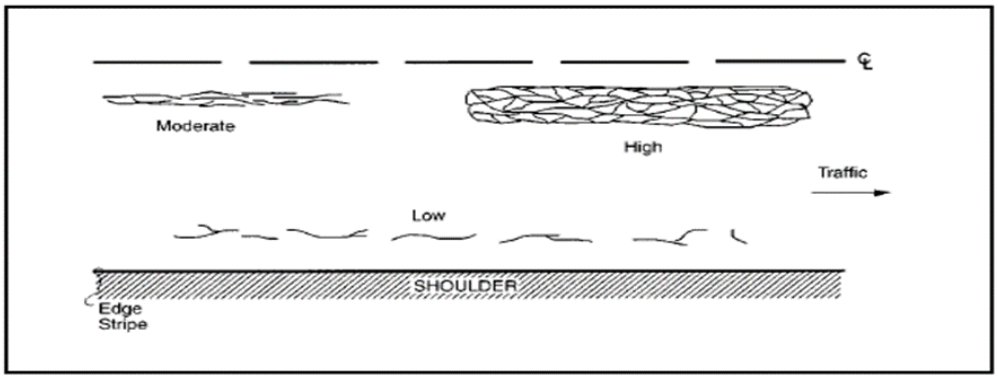

Block Cracking: Block cracks divide the pavement into approximately rectangular pieces and are also measured in terms of the affected area. Cracks with a mean width less than 6 mm are considered as low severe block cracks. Cracks with a mean width between 6 mm to 19 mm are considered as moderate-severe block cracks. Cracks with a mean width greater than 19 mm are considered as high severe block cracks. An occurrence should be at least 15 m long if it is to be rated as a block cracking.

Figure 2. Block cracking protocol (LTPP)

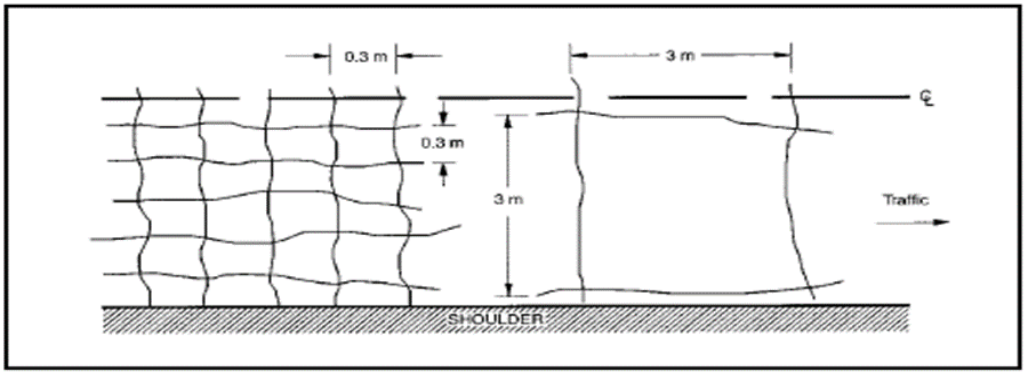

Edge Cracking: Edge cracking is generally crescent-shaped cracks that interconnect with the edge of the pavement. Edge cracking usually occurs within 2 ft. of the pavement edge, adjacent to the shoulder. Cracks with no loss of materials are considered as low severe cracks. Cracks with loss of materials up to 10% of the length of affected pavement length are considered as moderate-severe cracking. Cracks with considerable loss of materials greater than 10% are considered as the high severity level of edge cracking. Unit of edge cracking is the length in meters.

Figure 3. Edge cracking protocol (LTPP)

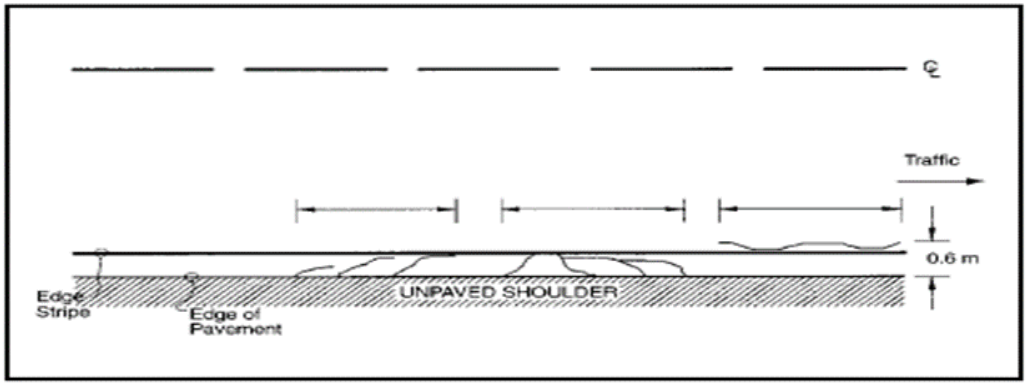

Longitudinal Cracking: Longitudinal cracking, predominately parallel to the pavement centerline, includes wheel path longitudinal cracking and non-wheel path longitudinal cracking. Longitudinal cracking is measured in linear feet (meters).

A crack with a mean width of less than 6 mm is considered as a low severity level of longitudinal cracking. A crack with a mean depth between 6 mm and 19 mm is considered as moderate severity longitudinal cracking. If the average crack depth is greater than 19 mm, it is considered as high severity longitudinal cracking. Figure 4 describes the difference between the wheel path and non-wheel path longitudinal cracking.

Figure 4. Longitudinal cracking protocol (LTPP)

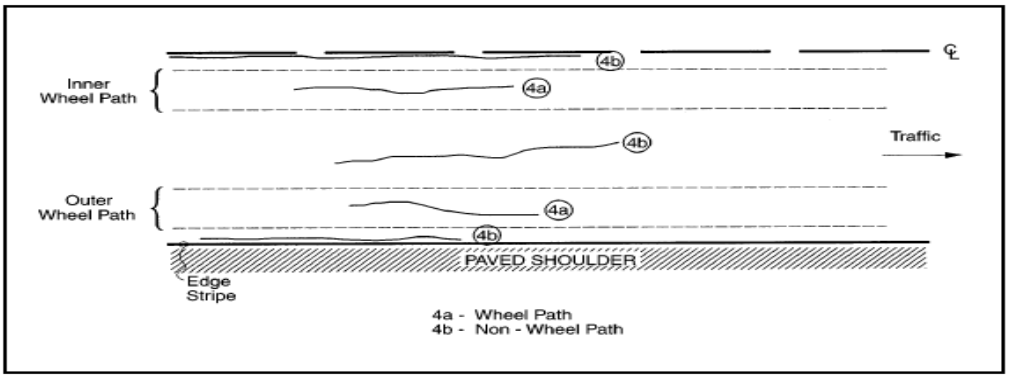

Transverse Cracking and Reflection Cracking at Joints: Transverse cracking is referred to as the cracking predominately perpendicular to the pavement centerline. It is measured in linear feet (meters). When a transverse crack found on an AC overlay surface that occur over a joint in concrete pavements, it is called as reflection crack at joints.

If the mean crack width is less than 6 mm then it is called low severity reflection cracking; if the mean crack width is in between 6 mm to 19 mm then it is called moderate severity reflection cracking; and if the mean crack width exceeds 19 mm then it is called high severity reflection cracking.

Figure 5. Transverse cracking protocol (LTPP)

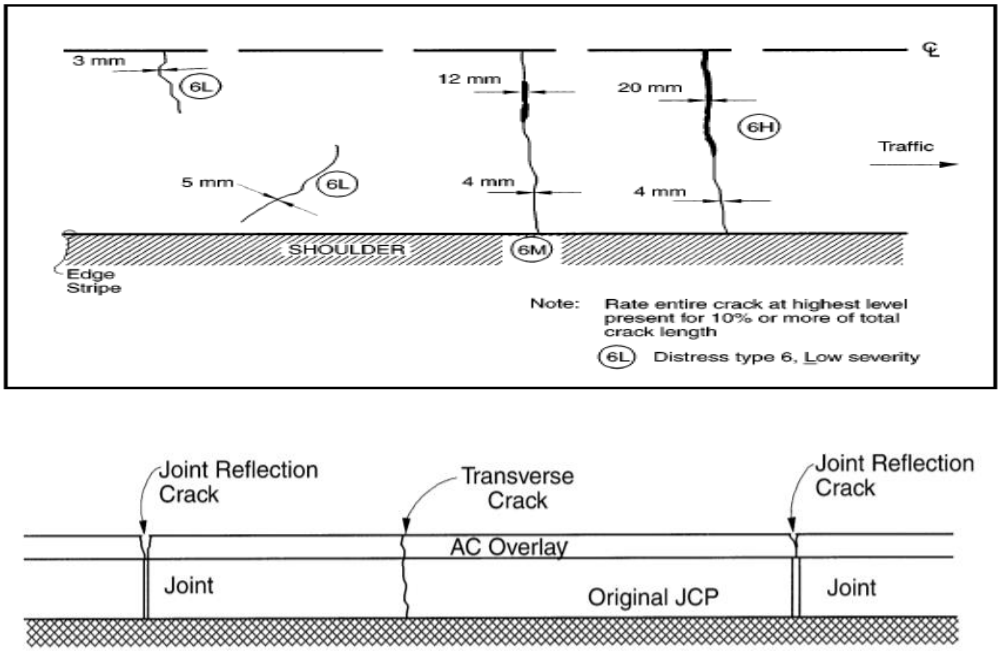

AASHTO R 85-18 Cracking Protocol

The AASHTO R85-18 describes the automated methods to quantify cracking distress in asphalt pavement surfaces [11]. In this procedure, high-resolution pavement surface images are collected using highway data collection vehicle, and the cracks with the dimension 25 mm (length) * 1 mm (width) are reported in this cracking protocol. Four types of asphalt pavement crack definitions (longitudinal, transverse, pattern, and others) were described in this protocol.

Table 2. Cracking protocol in AASHTO R 85-18 [9]

Types of Crack	Dimension of Crack	Crack Orientation
Longitudinal	At least 0.3 m (12”) long	+20 degree to -20 degree relative to center line

Types of Crack	Dimension of Crack	Crack Orientation
Transverse	At least 0.3 m (12”) long	70 degree to 110 degree relative to center line
Pattern	Network of cracks which creates a pattern	N/A
Other	Cracks not detected as pattern, longitudinal, or transverse ones	N/A

In AASHTO R 85-18 protocol, a full pavement section is divided into 5 zones (Figure 6). Zone 2 and Zone 4 depict the inside and outside wheel paths respectively. Any cracking presented in the wheel paths typically reflect the traffic load-related cracking. The sum of the cracking length (meters/feet) in each category and the mean width of the cracking for each type are outlined for each region. A typical summary produced in this protocol is 0.01 mile or less.

Figure 6. Wheel-path definition [11]

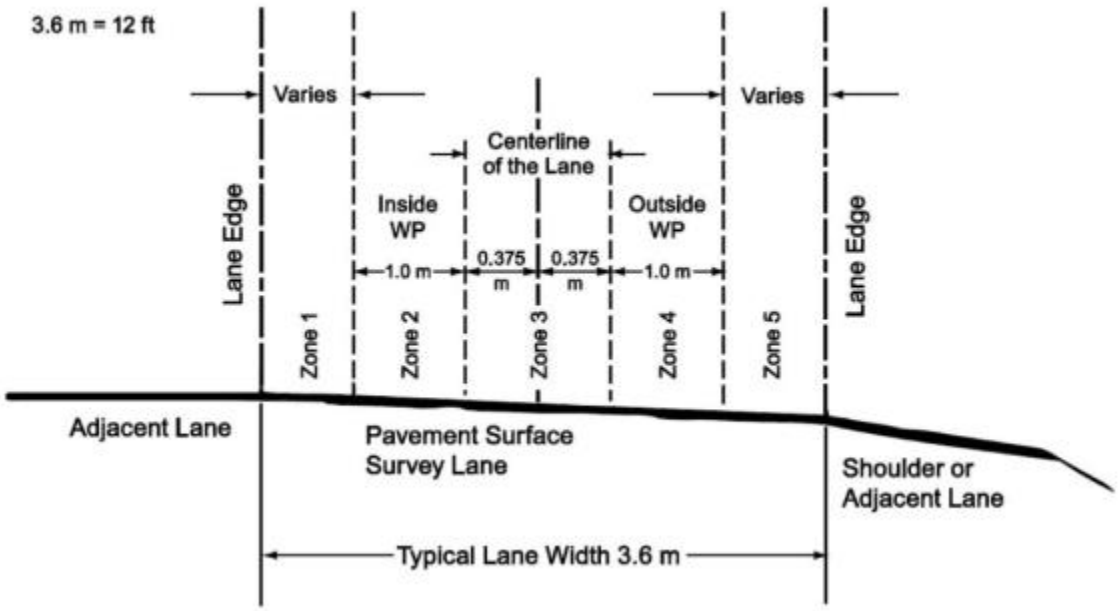

AASHTO R 55-10 Cracking Protocol

AASHTO R 55-10, “Standard Practice for Quantifying Cracks in Asphalt Pavement Surfaces,” describes the automated and manual proceedings to quantify cracking distress in asphalt pavement surfaces for network-level pavement management survey [12]. Similar to the AASHTO R 85-18 protocol, the cracks with the dimension 25 mm (length)*1 mm (width) are reported in this cracking protocol. Cracking within the wheel paths is predominately defined as “load associated or fatigue cracking” on the other hand, cracks outside the wheel path areas are defined as non-load-associated cracks. Figure 7 shows the wheel path definition in the AASHTO R 55-10 cracking protocol, in which the crack distresses are divided into three severity levels. Table 3 shows the crack dimension at each severity level.

Table 3. Severity level definition in AASTHO R 55-10 cracking protocol [12]

Severity Level	Dimension
Level 1	Crack width ≤ 3 mm (1/8”)
Level 2	3 mm (1/8”) ≤ Crack width ≤ 6 mm (1/4”)
Level 3	Crack width ≥ 6 mm (1/4”)

For each defined survey length (survey strip), intensity of cracking is calculated as the total length of cracking per unit area (m/m^2 or $ft./ft^2$)

Figure 7. AASHTO R 55-10 wheel path definition [12]

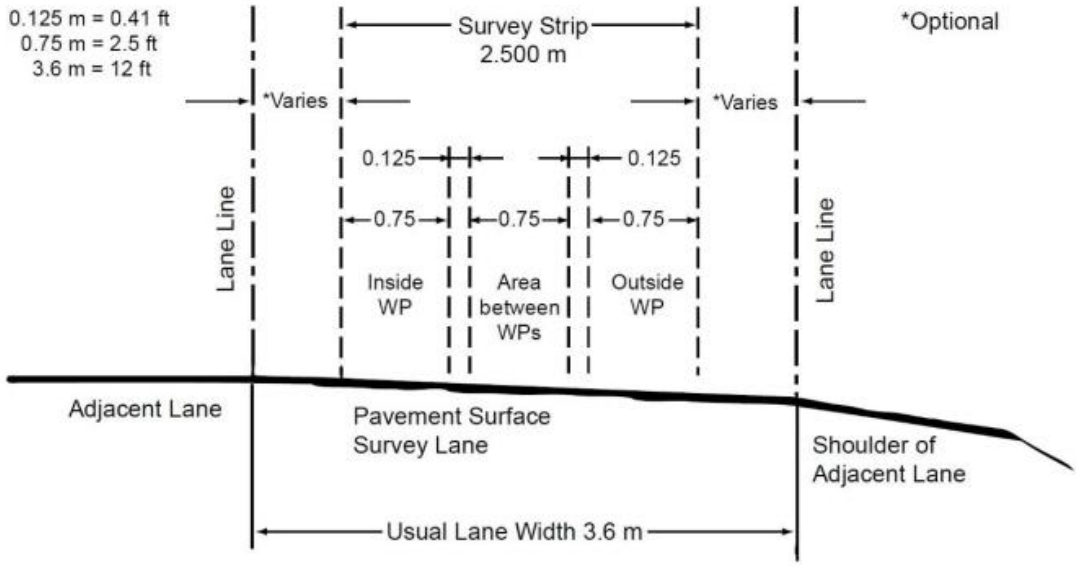

Louisiana PMS Cracking Protocol

Data in the PMS were collected according to the Louisiana Protocol, in which cracking is defined as a discontinuity of pavement [13]. Only two types of cracking are defined: fatigue (alligator) cracking and miscellaneous (random) cracking. Fatigue (alligator) cracking is defined in terms of its area in each wheel path on flexible pavements. The area of each wheel path has a transverse width of 3 ft. Louisiana Protocol clearly defines that longitudinal cracks which occur in the wheel path shall be classified as fatigue cracking.

Fatigue cracking has three severity levels. If there are only longitudinal cracking with very little intersecting transverse ones, then it is rated as low severity fatigue cracking. If there are intersecting longitudinal, transverse, and diagonal cracks and the crack width is less than or equal 0.25 in., then it is rated as medium level severity cracks. If there are intersecting longitudinal, transverse, and diagonal cracks and the crack width is greater than 0.25 in., then it is rated as high-level severity cracks. The cracks may form a network of polygons or blocks and spalling may be evident.

Any cracking not identified as fatigue (alligator) cracking is recorded as the miscellaneous (random) cracking in the PMS. Random or miscellaneous cracking includes types: longitudinal and transverse, each having three severity levels. If there are only longitudinal or transverse cracking (less than 0.25 in.) with no interconnecting cracks, then it is rated as low severity random (longitudinal or transverse) cracking. If

there are longitudinal or transverse cracks with width in between 0.25 in. to 0.50 in., then it is rated as medium-level severity random (longitudinal or transverse) cracks. If there are intersecting longitudinal or transverse cracks with width greater than 0.50 in., then it is rated as high-level severity random (longitudinal or transverse) cracks. Figure 8 shows the three severity levels of fatigue cracking according to Louisiana Protocol.

Table 4. Summary of Louisiana cracking protocol [13]

Crack Types		Crack Location	Measurement Unit	Severity Level	Dimension
Fatigue Cracking (Alligator Cracking)		Wheel Path	ft^2	Low	Interconnected hairlines
				Medium	Hairline ≤ Avg. crack width ≤ 0.25 in.
				High	Avg. crack Width ≥ 0.25 in.
Random Cracking	Longitudinal Cracking	Outside Wheel Path (predominately parallel to the center line)	ft.	Low	Avg. crack width ≤ 0.25 in.
				Medium	0.25 in. ≤ Avg. crack width ≤ 0.50 in.
				High	Avg. crack width ≥ 0.50 in.
	Transverse Cracking	If a crack extends from one-wheel path to another (predominately perpendicular to the center line)	ft.	Low	Avg. crack width ≤ 0.25 in.
				Medium	0.25 in. ≤ Avg. crack width ≤ 0.50 in.
				High	Avg. crack width ≥ 0.50 in.

Figure 8. Louisiana protocol fatigue cracking definition [13]

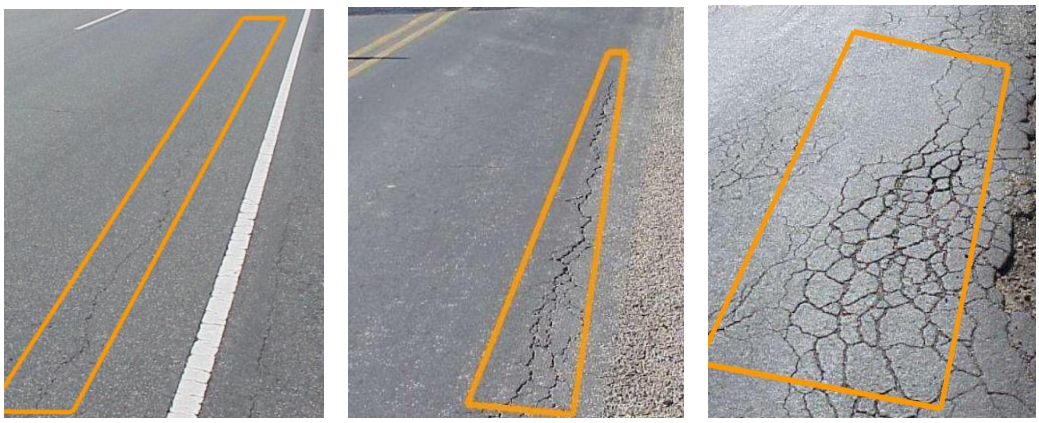

(a) (b) (c)

DOTD Pavement Condition Indices. DOTD uses the deduct value approach to calculate the pavement indices. For each distress type, distress indices are calculated on a scale of 0 to 100 where 100 indicates no distress. For each cracking type (alligator and random) there are different deduct points for each severity level [13]. Equations (1)-(2) are used to calculate the alligator cracking (ALCR) and random cracking (RNDM) indices.

$$ALCR = MIN\left(100, MAX\left(0, 100 - ALG_L DEDUCT - ALG_M DEDUCT - ALG_H DEDUCT\right)\right) \quad (1)$$

$$RNDM = MIN\left(100, MAX\left(0, 100 - RNDM_L DEDUCT - RNDM_M DEDUCT - RNDM_H DEDUCT\right)\right) \quad (2)$$

In which the subscripts H, M, and L refer to the high severity, moderate severity, and low severity cracking, respectively. Except for the wheel path cracking (alligator and longitudinal cracks on wheel paths) all other cracks fall in the random cracking criteria. The high, moderate, and low severity deduct values can be determined from the interpolation of cracking extent ranges shown in Table 5 and Table 6 (Louisiana Protocol, 2014).

Table 5. Alligator cracking deduct values

	Extent (ft^2)					
Severity	0-51	51-701	701-1301	1301-2401	2401-3168	>3168
LOW	0	1-16	16-21	21-25	25-28	28
MED	0	1-21	21-29	29-36	36-49	49
HIGH	0	1-29	29-43	43-50	50-61	61

Table 6. Random cracking deduct values

	Extent (ft.)					
Severity	0-31	31-301	301-1601	1601-5001	5001-6001	> 6001
LOW	0	1-3	3-16	16-18	18-20	20
MED	0	1-16	16-21	21-30	30	30
HIGH	0	1-26	26-28	28-42	42-48	48

Equation (3) can be used to calculate the Pavement Condition Index (PCI) for flexible pavements in Louisiana. For PCI calculation, only ALCR and RNDM cracking indices are used.

$$PCI = MAX\ (MIN(RNDM, ALCR, PTCH, RUFF, RUT\ ),\ [AVG(RNDM, ALCR, PTCH, RUFF, RUT\ ) - 0.85\ STD(RNDM, ALCR, PTCH, RUFF, RUT)]\ ) \quad (3)$$

Where,

RNDM = Random Cracking Index,
ALCR = Alligator Cracking Index,
PTCH = Patching Index,
RUFF = Roughness Index and
RUT = Rutting Index.

MEPDG Cracking Definition

The AASHTOWare Pavement ME Design is the latest pavement design software from AASHTO, which follows the Mechanistic-Empirical Pavement Design Guide (MEPDG) introduced by NCHRP. Three types of cracking distress are defined in the current MEPDG for flexible pavement: alligator cracking, longitudinal cracking, and transverse cracking.

Alligator Cracking (Bottom-up Cracking): The alligator cracking defined in the MEPDG is a form of load-related cracking that initiate at the bottom of the HMA layers. A series of cracks interconnect with each other to form an alligator pattern. These interconnected cracks are initially seen as longitudinal or transverse cracks of different sizes and shapes. MEPDG presumes that the alligator cracking starts at the bottom of the asphalt layers and propagate through the layers to the surface under continuous traffic loading. These cracks predominately appear in the wheel path of the traffic lane and are presented as the % of the lane area in MEPDG [14].

Longitudinal Cracking (Top-down Cracking): The longitudinal cracking defined in the MEPDG is a top-down cracking that initiates from the pavement surface and propagates to the bottom. It is a wheel load-related cracking that occurs within the wheel path and mostly parallel to the pavement centerline. This type of cracking initially shows up as short longitudinal cracks and then become connected with other cracks with continuous truck loadings. Other distress such as raveling and crack deterioration may show up along the crack edges, but they do not develop any pattern. Longitudinal cracking is presented as the total feet/mile by MEPDG. [14]

Transverse Cracking (Thermal Cracking): The transverse cracking defined in the MEPDG is thermal cracking. This type of cracking is primarily non-load related and occurs predominately perpendicular to the pavement centerline. Transverse cracking mainly caused by low temperature or change in thermal cycling. The unit of transverse cracking calculated by the MEPDG is feet per mile (meters per kilometer) [14].

Literature review of the cracking definitions indicates that different federal and state agencies have their own protocols for classifying crack distress. But in general, all the protocols use either a manual or automated system for cracking distress survey.

Past Studies on Pavement Surface Distress Survey

Manual Pavement Distress Survey

In general, a manual pavement survey is performed and recorded by a crew of trained raters to collect surface distresses and crack maps for a pavement section according to a designated distress identification manual [15]. A manual pavement survey may be conducted by a variety of transportation:

- Walking survey**:** Trained raters walk down along pavement test sections to visually identify and perform the manual measurements in terms of the distress types, quantities, and severities.
- Bicycle survey**:** Raters ride along the road and visually record the distress type and severity with estimated quantities.
- Driving or Windshield survey: Inspectors drive their vehicle and record the distresses for each type and severity level. In this method, instead of reporting the quantities of each distress, the raters report the distresses as the percentage of total pavement area or length. Such as 10% of pavement area is affected by alligator cracking or 15% of the total pavement length is affected by the longitudinal cracking.

According to Haas et al. [16], the walking survey performed by an experienced rater or crew can provide the most accurate surface distress identification and measurements among other survey methods. However, the walking survey is also the most time-consuming, costly and unsafe pavement survey method [17]. The walk survey is often only considered in a project level pavement evaluation, in which the pavement performance models may be developed and calibrated using a set of more accurate pavement distress survey results. For a network level pavement survey, the combination of both walking and windshield surveys can a good method to use, in which a randomly selected 15% of a pavement network may be walking-surveyed and the results are checked with those from the windshield survey for the entire network [16].

The NCHRP Synthesis 401 study proposed a semi-automated manual measurement method as the reference values to evaluate the automated distress measurements [18]. According to Kargah-Ostadi et al., in the semi-automated method raters use the high-resolution pavement images to locate and identify pavement cracking distress using a computer, and measure the extent and severity of each cracking distress type. This method is also time-consuming for a network-level pavement survey application and requires most of the human interference [19, 20, 21, 22].

Even though manual distress survey is the typical way to conduct pavement condition surveys, due to the issues of time, cost-effectiveness, and safety, in recent years most of

the state transportation agencies are transitioning towards automated methods of pavement distress data collection.

Automated Cracking Distress Survey

Automated surveys at traffic speed are now performed at network level in many state agencies and other countries for collecting pavement surface condition data. An automated pavement distress evaluation starts by obtaining 2D or 3D pavement images using a high speed survey vehicle and then run an image analysis involving various imaging algorithms to identify and classify pavement distresses. Figure 9 illustrates the typical methodology of the automated pavement distress evaluation, which includes data acquisition, data storage, image display, automatic distress processing, and distress report. One previous imaging analysis software is the Automated Distress Analyzer (ADA), which processes 2D pavement images at 1-mm resolution for cracking information with full-lane coverage at highway speed. Due to varying lighting conditions and low contrast, a 2D pavement image system is usually subjected to a higher level of error in the cracking measurement as compared to a manual rating survey. As 3D survey technologies become mature and reliable, the current pavement cracking survey is mostly using 3D laser cameras.

Figure 9. Automated distress evaluation process [2]

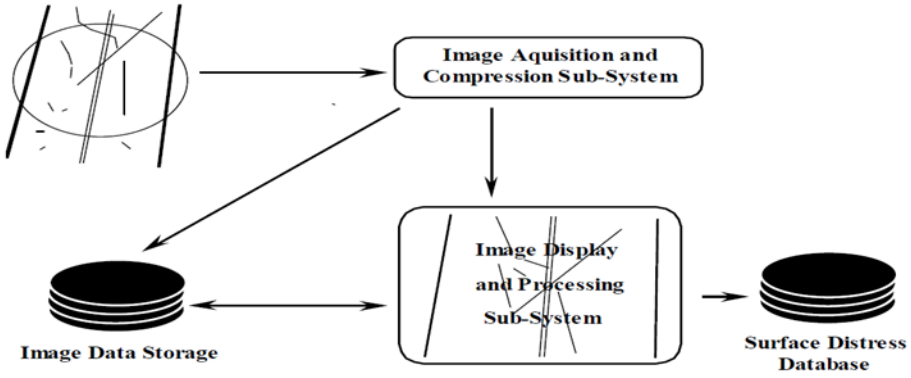

Evolution of Automated Distress Survey Technology

Haas et al. developed the first pavement distress survey vehicle which could collect various pavement distress data. The vehicle was also equipped with 2D cameras to collect pavement images and used an image recognition technology to detect and classify pavement surface cracking [23].

New Mexico researchers developed an automated distress evaluation system in 1994. It uses camcorders on a data collection vehicle to capture pavement images at 15 mph. Collected videos are then digitized into images and the accompanied algorithm classified the cracks in alligator, longitudinal, and transverse categories [24].

Wang et al. introduced digital area scan and line scan cameras in the pavement condition survey vehicle that can collect pavement images at 60 mph. Area scan cameras performed better than line scan cameras and can be integrated into any vehicle. Authors also developed a 2D image processing algorithm to exclude the distress free areas of pavement out of consideration which could potentially save a lot of time [25].

According to Chambon et al. image processing technology plays the most crucial role in distress detection, classification, and quantification. Over the years, pavement image collection systems have improved a lot and it is essential to develop reliable image processing systems to provide useful pavement condition surveys [26].

Zakeri et al., authored a study to discuss the various steps to successfully survey the cracking distress in asphalt pavements. According to this research, there are five main stages of image processing to evaluate pavement cracking distress: pre-processing of images, image segmentation, feature extraction, crack detection, and classification. Image pre-processing is required to eliminate unwanted marks in the pavements, such as oil stains, tire marks, etc. Image segmentation is required to locate the area of interest (location of distress). Feature extraction is necessary to identify useful features for the next two steps: crack detection and classification [27].

Tsai et al. assessed the execution outputs of six different methods for crack segmenting using actual pavement images from Atlanta, Georgia. Six different crack segmentation algorithms were compared against each other both quantitively and qualitatively. According to this research, the Dynamic Optimization-based algorithm performed better than the other five methods. Dynamic optimization method was able to detect hairline cracks which are very useful to select proper preventative measures [28].

Zou et al. proposed ‘CrackTree’ procedure for automatic crack detection from pavement 2D-images. Researchers applied the geodesic shadow removal algorithm to remove shadows from the pavement and get a clean image only highlighting the crack. Threshold-based algorithm and tensor voting was utilized to effectively prepare a crack map. ‘CrackTree’ algorithm can process 1 image with 800*600 resolution within 12 sec [29]

Oliveira et al. developed a fully automated crack detection and characterization system (CrackIT) using 2D pavement images. Unsupervised training of previously sampled crack images was conducted to successfully detect pavement crack. Pavement images were divided into a small block of pixels. Crack detection algorithm used unsupervised training to identify the pixels which contain crack (cracked pixels are typically darker than the surroundings). Then detected crack blocks are characterized according to the Portuguese Distress Catalogue. CrackIT system also provided a way to determine the severity level of each crack. The proposed method can process 56 pavement images in 2 minutes, but the precision of the crack detection algorithm was not good as it provided many false positives results. Collected pavement images contained no shadows from the roadside objects which was another drawback of the proposed method [30].

Hoang et al. authored a comparative study on the performance of six machine learning techniques that are being used for automated pavement crack recognition. Naive Bayesian Classifier, Classification Tree, Backpropagation ANN, Support Vector, Radial Bias Function Neural Network, and Least Squares Support Vector Machine (LSSVM) were compared against each other and the researchers discovered that LSSVM outperformed other classification algorithms [31].

The latest development in automatic pavement distress surveys is the application of 3D laser sensors. In recent years, 3D imaging technology gained favors from state agencies for pavement distress identification because it can measure the depths of the pavement distresses. Thus, research to establish an automated technology platform that can evaluate the key pavement distresses in 3D at highway speed is necessary to conduct [32].

Jiang et al. conducted a study to employ 3D pavement images and an enhanced dynamic optimization algorithm to improve pavement crack segmentation. The three-part optimization algorithm consisted of: applying two-step Gaussian filter to reduce the outliers, rut section and cross slope of the pavement, and identifying the regions which might have crack and determine the orientation of each crack. Four types of pavement cracking (alligator, longitudinal, transverse, and block) were evaluated and compared against the typical optimization algorithm. The researchers found that the enhanced algorithm took $1/4^{th}$ of the computation time and the accuracy of the proposed algorithm was much better than the typical algorithm [33].

Zhang et al. developed a convolutional neural network (CNN) based architecture- ‘CrackNet’ to automatically detect pavement cracks using 3D images. ‘CrackNet’ architecture was trained with 1800 3D pavement images and 200 images were utilized for

the validation purpose. This system does not use the commonly used pooling layers in developing CNN. The developed architecture divides the images into equal pixels and utilizes the feature extractor to define the widths, lengths, and orientation of each pixel. The developed architecture provides class scores for all pixels. Results from this research shows that 'CrackNet' architecture has higher precision, recall, and F-measures scores compared to other crack detection algorithms [34]. Li et al. proposed an improvement of the 'CrackNet' technology by using a deeper architecture and fewer parameters. The newly proposed 'CrackNet-V' architecture performed better when compared to the 'CrackNet' architecture with higher precision, recall, and F-measure scores. Even though, 'CrackNet-V' architecture was most efficient for 3D asphalt pavement crack detection, the results for wide cracks were not satisfying [35].

Commercial Automated Systems and Processing Software

The most important and integral part of the automated pavement condition survey is the data collection vehicle. There are different kinds of data collection vehicles available in the market that follows various technologies to collect distress data from the pavement. All these technologies follow one basic mechanism so that they can collect data from the pavement at a highway speed. Improvement of computer hardware and image processing systems led to the implementation of automated distress detection and classification systems. This part will discuss different vehicles and software that are in use for pavement crack detection and classification.

WiseCraX [25]: This system was developed by Roadware Inc. The system consists of three underlying systems: data collection, crack identification, and crack classification. Automatic Road Analyzer (ARAN) vehicle takes care of the data collection component. ARAN collects continuous pavement images with two video cameras attached at the back of the vehicle and covers the whole survey length. Each camera covers two meters wide area and images from each camera are stored sequentially in a single folder. WiseCrax follows a speed encoding algorithm that allows the camera to collect pavement images even at very high speed (80 km/h) and without shadows.

The crack detection algorithm developed for this system digitizes the photos from both cameras and converts into grayscale images. The detection algorithm identifies the beginning and endpoint of each crack and uses the x-y coordinate system to identify and mark each crack precisely. Length, extent, width, and location of each crack are reported and sorted. This whole process is called vectorization. Once the vectorization is completed, the algorithm then produces a crack map on the pavement surface, and data for each crack is reported in a table as a single entry. Classification of different cracks in

WiseCrax method is very flexible. As different agencies have different definitions and classifications protocols, the WiseCrax system was developed in a way that can meet the requirements of any classification protocol.

INO Laser Crack Measurement System (LCMS): INO LCMS system was developed by the National Optics Institute of Canada [36]. LCMS system can be deployed in a pavement management system to identify cracks and prioritize rehabilitation and preventative measures according to the need, cost allocation, and time constraints. This system has high-resolution cameras attached at the back of the vehicle which use specially built cameras and laser tools to acquire 2D and 3D images. LCMS system can automatically identify and analyze cracks according to the specified classification protocols. Cracks can be classified as transverse, alligator or longitudinal and can be evaluated according to their severity level. It can operate both in the day and nighttime and LCMS system can operate at a speed up to 100 km/h. The cameras can cover a 4-m wide road.

Figure 10. INO laser crack measurement system (INO)

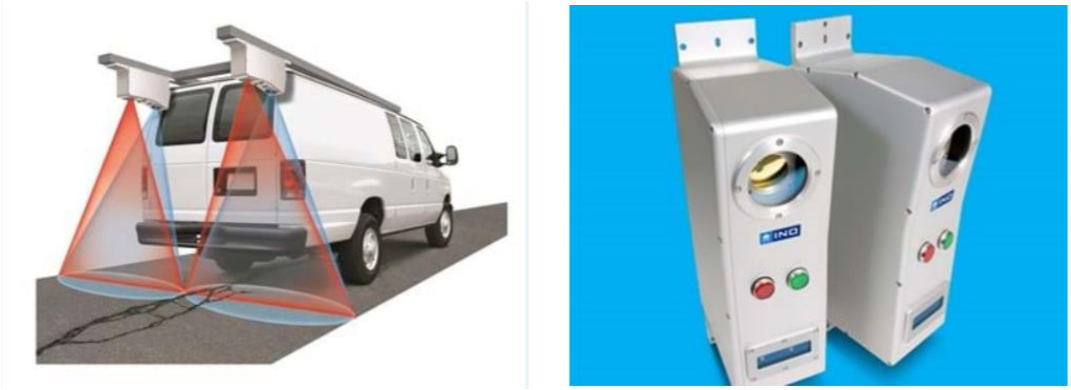

(a) INO LCMS vehicle (b) INO LCMS cameras (sensors)

Automated Distress Analyzer (ADA): An automated distress analyzer (ADA) was developed to detect and classify the cracks from real-time pavement images collected by the Digital Highway Data Vehicle (DHDV). Though DHDV has three subsystems: laser road profiling, pavement surface imaging, and right of way imaging, ADA mainly works with the pavement surface imaging to analyze the cracks [32].

For image acquisition purposes, tow line-scan cameras and two downward facing laser device pointers are attached with the DHDV vehicle. The system named Laser Road Imaging System (LRIS) allows the attached cameras to capture a limited amount of

information from the surface of the pavement within a narrow spectrum which in turn produce shadow-free pavement images. Two cameras can capture 4-m wide pavement surface when running at a speed of 100 km/h or more.

Figure 11. DHDV system and dataflow of DHDV [32]

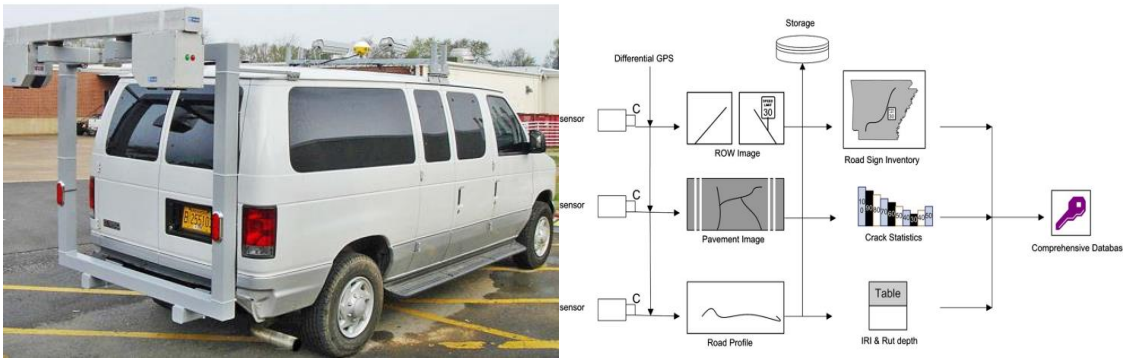

(a) DHDV and LRIS (b) Working algorithm of DHDV system

The Automated Distress Analyzer (ADA) uses pavement surface images collected and processed by the DHDV system to first detect and then classify the cracks according to different protocols. Linear cracks that are parallel to the pavement surface are classified as longitudinal cracks and perpendicular cracks are classified as transverse cracks respectively. Block cracks and alligator cracks are classified as Patterned Cracks. Lastly, a crack map is generated to highlight the detected cracks.

Pave 3D and Vision: Vision is a software developed by Fugro to automatically detect pavement cracks and classify them according to their severity level. This proprietary software of Fugro uses the pavement images collected by the vehicle ARAN developed by Roadware Inc.

Among other subsystems installed in the ARAN vehicle, Pave 3D subsystem collects the pavement images at a highway speed which can be used for pavement crack detection and classification by the Vision software. The hardware used in the modern day ARAN vehicle consists of a dual scanning camera Laser Crack Measurement Sensors (LCMS) developed by INO and Pavemetrics [37]. Pave 3D system can develop detail 3D models of the pavement and crack data can be extracted from the 3D model. ARAN can collect 5600 profiles while running at 62 mph with a profile spacing of 5 mm. It has a transverse field of view of 4 m or 13 ft. Z-axis (depth) resolution of 0.5 mm and x-axis (transverse) resolution of 1 mm [37]. Cracking data are collected from a 3D profiler. The system

utilizes the 3D imaging technology for each crack to ensure that the crack has propagated through the pavement. The 3D imaging system can substantially lessen the false positive error and improve the reliability of the cracking data.

Fugro uses its Vision software and the supporting pattern identification algorithm to ascertain the types of cracking. Cracking data are then measured and rated according to the distress identification document provided by the clientele.

Figure 12. ARAN vehicle and subsystem [37]

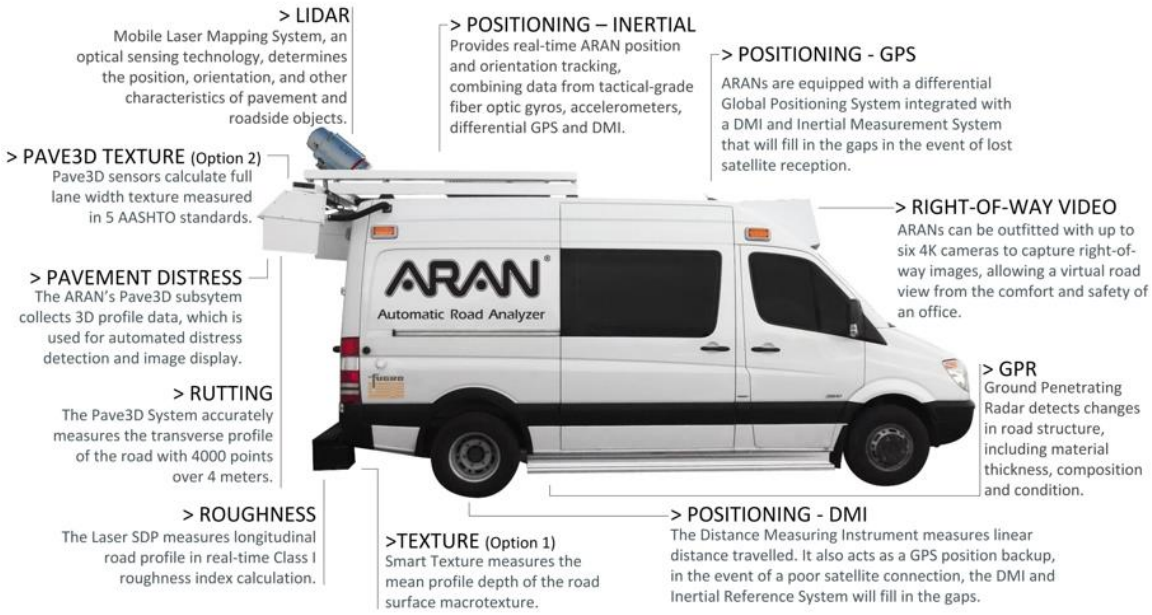

Evaluation of Automated Cracking Measurements

The quality of the manual distress survey heavily relies on the rater due to its subjective nature. A study by Rada et al. [22] found that the variability of an individual rater, even an accredited one, was large for any distress type. To provide a reliable and standardized specification for gathering pavement distress data for the LTPP program, AASHTO developed the *Distress Identification Manual*, which was first issued in 1987 and then updated in 1993, 2003, and 2014[32].

NCHRP sponsored a synthesis study on the automated pavement distress collection in 2004 [2]. Regarding the cracking distress, the study reported that, among a total of 56 responses, pavement images were collected through means by 30 agencies, but only 14 agencies implemented the automatic processing of the distress data. The others applied

the semi-manual data processing techniques using the pavement images. The major issue regarding the manual process was the inability to identify the distresses in a fast and reliable manner.

In terms of the accuracy of the automated distress survey, McQueen and Timm conducted the statistical analysis of the automated survey versus the manual survey for Alabama DOT [38]. It was found that the automated survey under-reported the alligator cracking with the severity of Level 1 and over-reported the alligator cracking with the severity of Level 3. For the purpose of pavement management, the study concluded that all types of cracking measurements need more accuracy.

McNeil and Humplick evaluated the data-acquisition component of two automated optical technologies and identified the main sources of error [39]. Different from other studies in which evaluation was made based on pavement images, this study simulated the longitudinal and transverse cracks. In this study, the parameters for the crack length, width, orientation, and spatial distribution were identified based on the visual inspection of a parking lot by a nine-person team. Researchers found that both technologies showed poor accuracy in the detailed report. However, when the number of observations were limited, and big sections were selected for comparison the results were comparatively good. In addition, the analysis demonstrated that the low-resolution quality of the images was responsible for measuring the wrong crack width, while the accuracy of the crack detection technology was affected by the crack length measurements. Since technologies have advanced greatly in the past two decades, the problems identified in this study might have been solved. Nevertheless, the methodology used in this study (i.e. simulation) is still appropriate to evaluate the latest automated distress acquisition systems.

Offrell et al. investigated the repeatability in the collection of the cracking distress of flexible pavements by video cameras, laser cameras, and a simplified manual survey [40]. 10 repetitive measurements were taken on a 10-km pavement section. Cracking was measured by two camera systems installed on the same vehicle—four analog video cameras mounted at the rear of the vehicle and six laser distance measuring cameras installed at the front of the vehicle. Subsequently, a typical windshield survey was performed by three different raters. Results showed that the two automated methods showed high repetition while the measurements from manual survey were comparatively low. Hence, the manual survey at the network level was not recommended. The authors also discussed other reliable measurements that automatic methods provided, such as the crack length, position, direction, shape, and percentage of the cracked area.

New Jersey DOT (NJDOT) conducted a study to compare the data collected by human raters with those by the automated distress survey equipment [7]. Two vendors collected the data of the pavement condition on fourteen selected test sites. Then the NJDOT staff investigated the pavement condition through a windshield survey. The starting point of the test sites was marked with a white paint stripe that could be identified in the images and assist the vendors as a reference point for the repeated runs. Through graphical comparisons and statistical analyses, it was concluded that the automated distress survey equipment was applicable to collect the cracking distress data with the quality control checks.

Another study conducted in Australia [41], evaluated both 2D and 3D automated crack detection and measurement systems and found a strong correlation between two automated measurements when the pavement surface was dense graded. For the rough textured surface, the false positive error and measurement error increased significantly. Qiu et al. compared the 3D crack measurement system with manual measurements in terms of inherent errors and found those crack measurements varied significantly for two systems [4].

Wang et al. conducted a precision test of the cracking package in the Automated Distress Analyzer [32]. The study analyzed 20 road sections consisting of four severity levels. In the precision test, four out of the twenty road sections were manually surveyed repeatedly by nine raters four times. The rest of the 16 roadway sections were manually rated by three raters who demonstrated the ability to be statistically consistent. The UK SCANNER protocol was used to calculate the index for each section as an indicator of the cracking condition. The nine raters were considered as “laboratories” and, similarly, four pavement sections as “material”. The importance of the precision test was that it obtained the precision statistics of the raters’ data before using them to establish the reference and the acceptable range for the data from the automated survey. Unlike accepting a simple average of all raters, the precision test identified outliers and only retained those statistically reasonable data for further analysis. Overall, the study found that 90% of the automated results were statistically acceptable. As expected, the semi-automated results for all sections were within the acceptable range. Furthermore, the study tracked the time consumed in each process (manual, semi-auto, and auto). Results showed that manual processing took 45 minutes to 2 hours to evaluate one 0.1-mi section, depending on the distress quantity of the section. Semi-automated processing took less than half of the time required for manual processing. Automated processing only took 16 seconds per section in a moderately equipped computer. Hence, the study concluded that

the time and cost savings from a fully automated survey can be substantial when it is used for a large network.

A recent study [8] evaluated three different automated crack detection systems with manual cracking measurements on twenty 550-ft. pavement sections in Texas. The results showed that a large number of false positives and missed cracks were observed between the manual measurements and those from the three automated systems considered. The false positive indicates that the automatic detection system reports a crack, however, no crack can be detected from manual measurements. Meanwhile, the missed crack refers to an error when the automatic detection system does not report a crack but the crack is detected from manual measurements. This study generally confirms that there still existed a certain degree of inconsistency between the manual and automated cracking measurements under the current state of the practice in high-speed data collection technologies. On the other hand, this study also reported that the number of false positives may be significantly reduced if applying manual post-processing on the automated cracking measurements. This implies that both the accuracy and quality of the automated cracking measurements may be improved through a manual post-processing procedure, if available.

Kargah-Ostadi et al. developed a framework to evaluate the accuracy, precision, repeatability, reproducibility, and efficiency of manual, semi-automated, and automated survey systems for rigid pavement. The results demonstrated that automated system provided somewhat accurate results (83%) in transverse cracking measurements when compared to the manual surveys (75%) but the accuracy was far less when compared to the semi-automated method (93%). For longitudinal cracking, the accuracy of the automated system was lower than transverse cracking (71%). Precision analysis showed that automated system had lower precision compared to the manual and semi-automated method. Researchers identified that automated system was unable to provide correct crack detection and measurements in the presence of joint strips, lane strips or pavement markings [20].

Tao et al. conducted a research to statistically evaluate the performance of Mississippi's state of the practice automated cracking distress survey system [42]. Manual/Semi-automated cracking survey results from 22.8 miles of asphalt pavement was used as the reference or ground truth value to evaluate the automated system. The results showed that automated system over detected longitudinal and transverse cracking as the false positives and precision error rates were higher than the missed crack and recall error. Statistical analysis on the crack measurement shows that the accuracy and precision of

the automated system were better for transverse cracking measurement than longitudinal cracking. Although, the automated system showed underestimation tendency in crack measurement. Overall, researchers concluded that the automated survey method is not reliable and still not ready to replace the traditional semi-automated method.

Artificial Neural Network (ANN) in Pavement Condition Survey

ANN Introduction

ANN is a globally accepted analogical tool that imitates the biological function of human brains. Fundamental elements in ANN are called nodes, which are similar to the neurons and weighted connections behave like synapses in the human biological system [43]. Like human brains, ANN can learn from experience as the nodes process the information locally and improve the performance of the model in the environment [44, 45]. Nowadays, ANN is a frequently utilized tool because of its ability to work with non-linear data, tolerance for outliers, the generalization of data, and flexibility with fitting complex datasets. Furthermore, there are various types of ANN that can be utilized in different scenarios based on the characteristics of problems [46].

The application of neural networks in the civil engineering sector has increased over the past few decades because of its adaptability to work with complex non-linear data. ANNs have been found to be very useful in dealing with pavement engineering problems due to the non-linear approximation of functions [47]. According to Plati et al. ANN can be a very essential tool to deal with large or small datasets. Although, modeling with large datasets provides more accurate approximation [48].

Feed-Forward ANN: Feed-forward ANN models are one of the most common types of ANN models and are generally used for function approximation and regression. A typical feed-forward neural network consists of input layers, hidden layers, and output layers. In the input layers, one or more independent variables can be defined. Output layers may consist of just one or multiple target variables and hidden layers deal with weight adjusting and updating. Single or multiple hidden layers can be used to process the data until the model produces the desired result. All of the layers may contain multiple neurons/nodes to process the data. These neurons are interlinked with each other and previous layers. Bias is distributed among each neuron and weight is assigned to the connection link among the neurons [49].

Figure 13. Typical feed-forward ANN architecture [50]

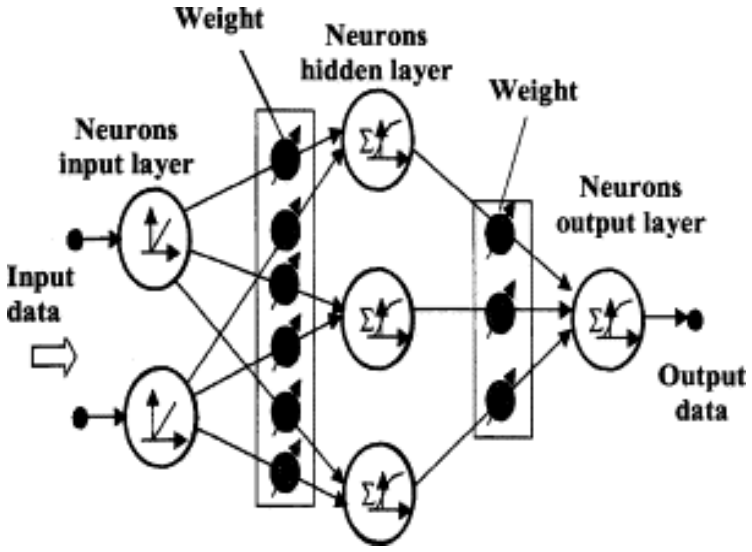

Back-Propagation ANN: Back-propagation ANN uses the training of the input data to produce the desired output to match with the target values. Back-propagation algorithm utilizes gradient descent and the mean square error to modify the weights in the neuron connections. In this algorithm, a little weight is assigned at the network connection at first, and then the learning sample is adjusted to achieve the minimum gradient of the error. The difference between the predicted output and target value is described as the error signal. The error signal is propagated from the predicted or output layer to the input layer. Weights in each connection are updated regularly to match the predicted output with original target values [51].

Figure 14. Typical back propagation ANN [43]

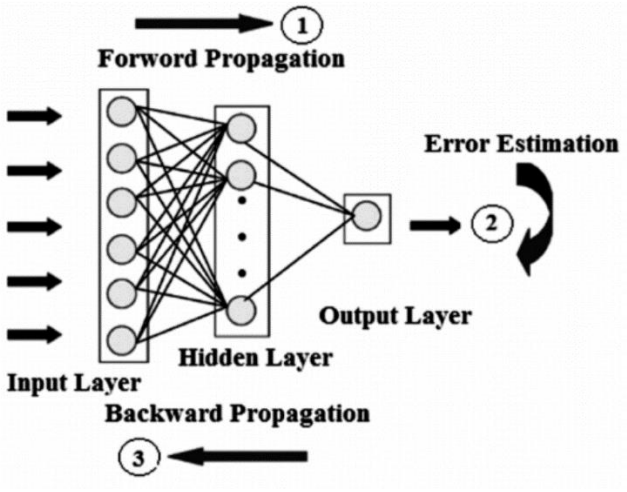

Torrecilla et al. provided a brief description about the different learning algorithms used in ANN back-propagation. Selection of a learning algorithm depends on the characteristics of the problem. Table 7 provides a brief overview of the generally used training algorithms used in back-propagation ANN.

Table 7. Brief description of commonly used training algorithms in back propagation neural networks [52]

Learning Algorithms	Descriptions
Variable Learning Rate- Gradient Descent	
TRAINGD	Learning rate is slow and can be used in incremental training.
TRAINGDM	Faster than TRAINGD and can be used in incremental training.
TRAINGDX	Faster than TRAINGD. Can only be used in batch mode training.
TRAINGDA	Faster than TRAINGD and TRAINGDM. Can only be used in batch mode training.
Resilient Back Propagation	
TRAINR	Random incremental training. Minimal storage with fast convergence.
TRAINRP	Minimal storage with fast convergence. Can only be used in batch processing.
Conjugated Gradient Descent	
TRAINCGF	Smallest storage requirements.
TRAINCGP	Faster than TRAINCGF and larger storage requirements.
TRAINCGB	Faster than TRAINCGP.

Learning Algorithms	Descriptions
TRAINSCG	Used for general purpose training.
Quasi-Newton Algorithm	
TRAINBFG	More iteration in each conjugate and Fast convergence. BFGS Quasi-Newton Method.
TRAINOSS	Adjust between Quasi-Newton method and Conjugate Gradient method.
Levenberg-Marquardt	
TRAINLM	Memory reduction features and fastest training algorithm for moderate sized network.
Automated Regularization	
TRAINBR	Bayesian regularization. Modification of Levenberg-Marquardt algorithm.

Aside from training algorithms, transfer functions are used in ANN to learn the temporal frequency or non-linear relationship among inputs and outputs variables. The most commonly used transfer functions are Log-sigmoid transfer function (LOGSIG), Hyperbolic tangent transfer function (TANSIG), and PURELIN transfer function. LOGSIG and TANSIG transfer functions generally have a sigmoidal shape. Although, they can take other forms based on the non-linearity of the data. Outputs from LOGSIG and TANSIG transfer functions range from 0 to +1 and -1 to +1 respectively [53]. LOGSIG, TANSIG, and PURELIN transfer functions can be estimated from Equations (4-6) [54].

$$LOGSIG:\ Y_{i=}\frac{1}{(1+exp(-X))} \tag{4}$$

$$TANSIG: Y_i = \tanh(\mathrm{X}) \tag{5}$$

$$PURELIN: Y_i = (\mathrm{X}) \tag{6}$$

ANN in Pavement Condition Prediction

Sollazzo et al. used the pavement roughness data from the LTPP database to develop an ANN model to predict the structural performance of the pavement. Researchers used a Multi-Layer Feed-Forward ANN as the prediction model where the inputs were: roughness index, structural parameters, traffic parameters, and climatic parameters collected from the LTPP database, and the target value was the structural numbers calculated from the FWD data. Results showed that ANN model produced high accuracy in predicting structural number with R^2 values 0.877, and 0.850 for validation and testing dataset respectively. The authors concluded that ANN model can successfully predict pavement structural performance from roughness index, and it would minimize the necessity for frequent deflection testing [55].

Vyas et al. conducted a similar study to predict the pavement performance from roughness data. Instead of collecting the input variables from any database, Vyas et al. conducted a thorough field testing program and collected 1452 observations. Vyas et al. used pavement roughness, structural parameters, and climatic parameters as the inputs and structural performance data derived from FWD testing as the target. The authors trained a total of 16 ANN models and the best model showed R^2 values 0.875, and 0.868 for testing and validation dataset respectively. Researchers also concluded that utilizing general pavement information and roughness data in ANN model can successfully reduce the frequency of FWD testing for structural performance determination [56].

Kargah-Ostadi et al. successfully implemented an ANN model to predict the pavement roughness index using pavement age, previous IRIs, HMA thickness, traffic data, and weather condition data. The developed ANN model produced an R^2 value of 0.9578 when compared with the measured IRI [57]. Lou et al. developed an ANN model to predict pavement cracking index in Florida and compared the model with the typical autoregressive model. Research found that ANN model predicted the cracking index more accurately than the typical regression models [58].

Objective

The objectives of this study are two-fold as follows:

For DOTD Pavement Management System (LA-PMS) Collected Cracking Data:

- Conduct a manual cracking distress survey using semi-automated image analysis approach;
- Evaluate the accuracy and precision of automated cracking detection and measurement results for both 3-D and 2-D automated measurement systems considered in LA-PMS;
- Perform a project level (a 50-ft. interval based) comparison analysis using the 3-D automated and manual cracking measurement results;
- Conduct a network level (a 0.1-mile interval based) comparison analysis using the 3-D automated and manual cracking measurement results;
- Develop an ANN application that correlates between the 3-D automated and manual cracking measurement results.

For LTRC Digital Highway Data Vehicle ($DHDV_{LTRC}$):

- Develop a software application to generate an automated cracking survey report from the high-resolution 2-D images collected.

Scope

To achieve these objectives, a comprehensive manual cracking survey was conducted on 23 selected pavement sections in Louisiana. The 23 selected sections contained 28.6 miles of flexible pavement. Manual measurements were reported for every 50-ft. subsections and 0.1-mile subsections for project and network-level assessment respectively. Automated cracking data for every 0.1 mile was collected from LA-PMS and 50-ft. cracking data were collected from the DOTD contracted vendor's proprietary software. Statistical analyses were conducted to find out the difference between the manual measurements and automated measurements. Statistical Analyses includes: Comparative analysis, accuracy and precision results, t-test, Monte-Carlo analysis and Simple Linear Regression. An ANN model was developed for the verification of PMS data for network-level evaluation. To utilize the LTRC vehicle's high-resolution pavement images, an already established 'Crack Detection' application was modified to add a crack classification and measurement algorithm to provide an automated package for crack quantification.

Methodology

The methodology of this research was divided into two parts. Firstly, as described in the literature, the LA-PMS data are based on pavement condition measurements that are collected biennially using an Automatic Road Analyzer (ARAN) system that provides a continuous assessment of the Louisiana pavement network. Historically the pavement crack measurement in LA-PMS were obtained from a 2D image collection system in ARAN. Starting from 2017, DOTD began to use a new 3D image collection system of ARAN in collecting its pavement condition data. The ARAN collected pavement images are further analyzed by an automated image analysis software called Vision for classification and quantity measurement of pavement cracking. In LA-PMS, the automated cracking reports for asphalt pavement include the alligator, longitudinal, transverse, and random cracking measurements on a 0.1-mile subsection base. Due to the cracking survey report generated by the automated system has not been fully validated, the first part of the study aims to provide a comprehensive quality assessment of the automated cracking data and provide recommendations for future applications. In this regard, the following tasks were performed:

- Imaging Data Project Selection.
- Manual and automated crack detection and classification.
- Evaluation of 3D automated crack detection accuracy.
- Statistical analyses between manual and automated cracking measurement at both the project and network levels.
- Development and application of an ANN-based computer model for adjusting the automated cracking measurements in LA-PMS.

Secondly, for the $DHDV_{LTRC}$ collected high-resolution 2D pavement images, this study developed a MATLAB-based computer program using an open source cracking identification algorithm in generating an automated cracking report for research purpose.

Project Section

LA-PMS Calibration Control Sites

DOTD selects nine 0.5-mile long control pavement sites for calibration of the current vendor's highway data collection system, or ARAN9000. Cracking distress data from

nine calibration control sites in Louisiana were used for the preliminary comparison among manual, 2D, and 3D automated data. Even though only flexible pavements were used for the quality assessment of 3D automated data, all three types of pavements in Louisiana (flexible, composite, and rigid) were used for this section. Table 8 represents the general description of the calibration sites used for the comparison in this section. Table 8 shows that total of 4.5 miles of pavement sections were rated from 9 control sites and each site was 0.5 miles long. The automated pavement condition data were collected by the vendor in 2016 on nine pavement sites with two image collection systems (2D and 3D) for a comparison purpose. The calibration sites include three pavement types (asphalt, composite, and jointed concrete) and each are 0.5 mile long (Table 8).

Table 8. General description of the calibration control sites

Control Site No.	District	Route	Begin mile post	End mile poste	Pavement Type
CTLSITE-02	61	US190	3.2	3.7	JCP
CTLSITE-03	61	LA019	6.8	7.3	COM
CTLSITE-04	61	LA042	5	4.5	JCP
CTLSITE-05	61	LA067	9.9	10.4	COM
CTLSITE-06	61	LA067	6.4	6.9	ASP
CTLSITE-07	61	LA010	1.2	1.7	ASP
CTLSITE-09	61	LA019	11.4	11.9	COM
CTLSITE-10	61	LA408	5.2	5.7	ASP
CTLSITE-13	61	LA964	0.2	0.7	ASP

Flexible Pavement Cracking Test Sections

To evaluate the automated 3D crack measurement accuracy, test sections were selected in a way to represent the typical pavement conditions and characteristics of the Louisiana highway network. A total of 23 flexible pavement sections were selected based on

different variables associated with Louisiana pavements. The severity (e.g., good, fair, and poor) of the cracking was taken into consideration during the selection of the sections. In addition, the selected sections are intended to represent most of the variables (e.g., geographic location, traffic level and year since last treatment) in the data collection process that DOTD encounters during the routine data collection. Figure 15 shows the geographical location of these projects. The selected test sections include 4 interstate asphalt pavements, 7 US highways, and 12 Louisiana roadways.

Figure 15. Geographical location of the selected projects

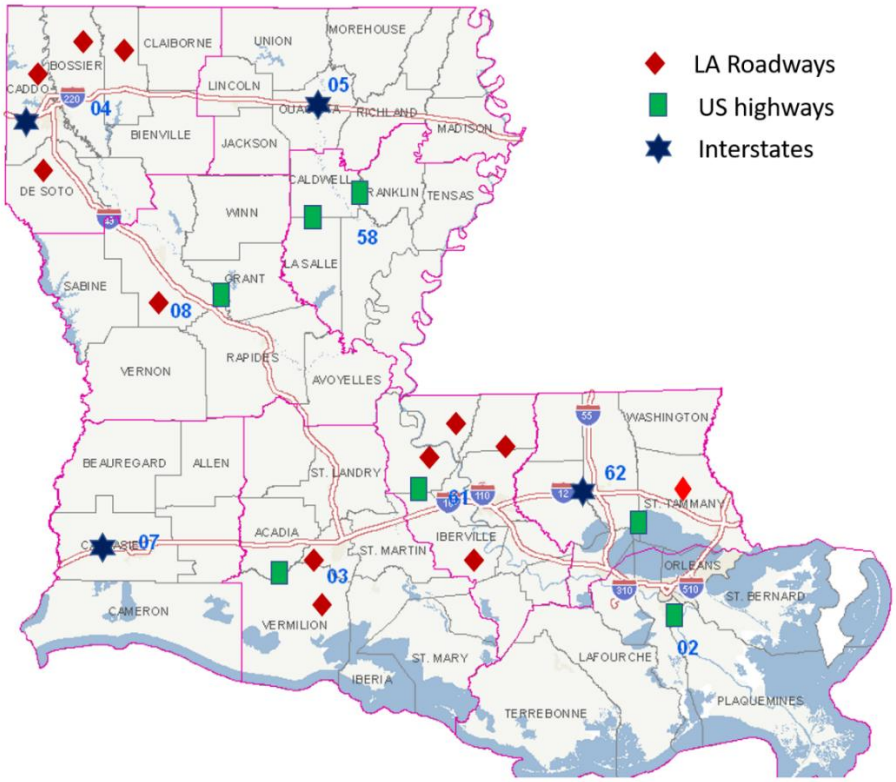

Table 9 shows the general description of the selected projects. In terms of initial traffic, ADT ranges from 640 to 37,510 vehicles per day which covers the low, medium, and high-volume roads. ALCR and RNDM column represents the alligator cracking index, and random cracking index respectively. ALCR range from 68.2 to 100. Subsequently, RNDM ranges from 70.8 to 100. Regarding the last treatment performed on these pavement sections, the year since the last treatment ranges from 1 to 36 years.

Table 9. General description of the selected projects

Control Section	Route	District	Parish	Length	ADT	ALCR	RNDM	Year since Last Treatment
034-05-1-010	LA 0006	08	35	0.1-1.1	7000	77.9	86.6	17
055-06-1-010	LA 0014	03	57	0.0-0.7	5872	84.0	81.3	36
057-06-1-010	LA 0013	03	20	0.0-1.0	4400	77.6	94.3	11
058-02-1-010	LA 0041	62	52	0.0-1.0	4200	87.9	98.0	9
060-04-1-010	LA 0067	61	19	6.3-6.8	2700	73.7	81.4	30
097-01-1-010	LA 0169	04	09	2.7-5.0	2500	80.1	90.8	22
100-01-1-010	LA 0514	04	41	0.5-6.7	1320	75.7	83.7	11
219-30-1-010	LA 0010	61	39	1.7-2.7	990	88.2	83.5	21
230-03-1-010	LA 0075	61	24	0.0-1.0	1930	98.5	95.6	21
300-04-1-010	LA 0513	04	16	0.0-1.0	710	98.3	98.9	8
839-02-1-010	LA 0419	61	39	0.0-1.0	640	78.2	80.6	21
841-02-1-010	LA 0788	04	41	1.0-2.0	970	68.2	78.1	24
008-30-1-010	US 0071	08	40	0.0-1.0	19300	87.8	77.6	22
008-01-2-010	US 0190	61	61	13.1-12.1	20100	82.3	90.7	13
013-08-1-010	US 0051-X	62	53	0.0-1.0	23100	94.3	90.6	6
015-05-1-010	US 0165	58	30	1.0-2.0	4900	98.1	95.6	1
026-05-2-010	US 0425	58	13	7.0-6.0	4000	99.4	100	5
080-01-1-010	US 0167	03	57	1.0-2.0	19300	99.9	95.9	7
424-07-1-010	US 0090	02	55	17.8-18.7	22800	84.7	90.9	11
450-03-1-010	I -0010	07	27	6.4-7.4	37,510	100	98.3	5
451-01-1-010	I -0020	04	09	1.8-2.8	36,600	77.8	79.8	10
451-06-1-010	I -0020	05	37	6.2-7.2	33,040	100	86.0	1
454-03-1-010	I -0012	62	53	0.2-1.2	24,070	99.7	70.8	1

Manual Cracking Survey and Measurements

In this study, the manual cracking survey was performed using a high resolution pavement image collected on selected pavement sites by ARAN. In a manual crack survey, a trained rater first manually marks all individual pavement cracks on a pavement image using the vendor provided image processing software on a workstation. Based on the DOTD's cracking protocol the rater then identify manually each cracking type with severity levels and input the identified cracking information into the processing software. Finally, the process software produces a detail manual cracking report for a selected pavement section based on the marked pavement cracks and a chosen subsection length. Figure 16 presents an example of the manual crack survey.

Figure 16. Manual data collection in a semi-automated way (a) crack detection and classification (b) generating manual cracking distress report

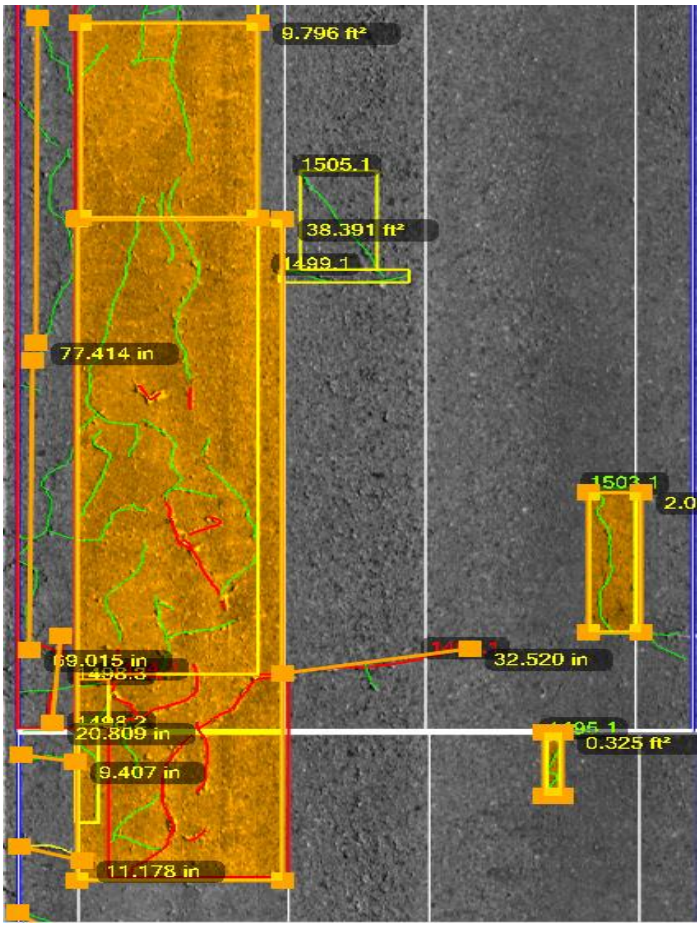

(a)

BeginChain	EndChainage	ALGCRK_H	ALGCRK_L	ALGCRK_M	LNGCRK_L	LNGCRK_M	TRNCRK_H	TRNCRK_L	TRNCRK_M
12405.7	12396.2	0.0	0.0	81.3	0.0	0.0	0.0	0.0	2.8
12396.2	12386.8	0.0	0.0	3.5	0.0	5.2	0.0	17.0	0.0
12386.8	12377.3	0.0	45.7	65.6	0.0	0.0	0.0	14.0	0.0
12377.3	12367.8	0.0	48.7	1.4	0.0	3.7	0.0	22.3	18.6
12367.8	12358.4	0.0	4.7	0.0	0.0	13.3	0.0	0.0	11.5
12358.4	12348.9	38.9	34.9	13.8	0.0	9.5	0.0	9.0	19.1
12348.9	12339.4	2.8	68.6	23.8	0.0	22.7	3.5	6.9	6.6
12339.4	12329.9	0.0	74.9	8.1	0.0	8.2	0.0	0.0	0.0
12329.9	12320.5	0.0	38.0	0.0	0.0	0.0	0.0	0.0	0.0
12320.5	12311.0	0.0	56.8	0.0	0.0	0.0	0.0	2.9	0.0
12311.0	12301.5	0.0	31.1	24.2	0.0	0.0	0.0	2.8	0.0
12301.5	12292.1	0.0	82.0	0.0	0.0	0.0	0.0	0.0	0.0
12292.1	12282.6	0.0	65.4	0.0	0.0	0.0	0.0	0.0	22.8
12282.6	12273.1	0.0	0.0	0.0	0.0	0.0	0.0	0.0	10.9
12273.1	12263.7	0.0	22.7	18.8	0.0	3.4	10.6	4.7	10.0
12263.7	12254.2	0.0	0.0	0.0	0.0	0.0	0.0	10.7	16.2
12254.2	12244.7	0.0	0.0	0.7	0.0	25.9	0.0	15.2	4.9

(b)

More specifically, in this study the manual cracking distress measurements were reported in each 50-ft. and 0.1-mile subsections for a project- and network-level analysis, respectively. Firstly, the wheel path was identified for every subsection. The next step was to mark the cracking distress and determine the type and severity levels according to LA-PMS. Detected cracks were classified as alligator, longitudinal, and transverse cracking. Alligator cracking was reported in three severity levels. If there was only longitudinal cracking with very few intersecting transverse ones in the wheel path, then it was rated and reported as low severity alligator cracking. If there were intersected longitudinal, short transverse, and diagonal cracks, that occur solely in the wheel paths, with crack widths that range from hairline to 0.25 in., then it was rated and reported as moderate severity alligator cracking. If there were intersecting longitudinal, transverse, and diagonal cracks that occur solely in the wheel paths, with the crack widths generally greater than 0.25 in. then it was rated and reported as high severity alligator cracking. The cracks may form a network of polygons or blocks, and spalling may be evident. Total alligator cracking measured for each section were reported in ft^2.

Cracks presented in the non-wheel path and predominately parallel to the traffic flow were classified as longitudinal cracking. Longitudinal cracking was reported in three severity levels. If the average crack width was less than 0.25 in., it was rated and reported as low severity cracks. If the average crack width was in between 0.25 in. to 0.50 in., it was rated and reported as moderate severity cracks. If the average crack width exceeds 0.50 in., it was rated as high severity cracks. Total longitudinal cracking measured for each section were reported in ft.

Cracks that are predominately perpendicular to the traffic flow were classified as transverse cracking. Transverse cracking was reported in three severity levels. If the average crack width was less than 0.25 in., it was rated and reported as low severity cracks. If the average crack width was in between 0.25 in. to 0.50 in., it was rated and reported was moderate severity cracks. If the average crack width exceeds 0.50 in., it was rated as high severity cracks. Total transverse cracking measured for each section were reported in ft.

Random cracking measurements were calculated by adding the total longitudinal cracks and transverse cracks reported in each section. LA-PMS use alligator and random cracking indices to estimate the composite pavement condition index. In this study, one rater with a good knowledge of the current DOTD cracking measurement protocol manually rated on the collected LCMS3D images. The manual cracking measurements were then used as the 'ground truth' values for comparison with the automated computer-algorithm identified cracking reports for Louisiana flexible pavements in LA-PMS.

Automated Crack Detection and Classification. DOTD currently uses a vendors' ARAN 9000 system in collecting the pavement condition data for LA-PMS (after 2017). ARAN 9000 is equipped with the automatic pavement crack detection sensor – Pave3D. The supporting software in the system was designed to automatically conduct crack classification and generate surface distress report for LA-PMS. Figure 17 shows the Pave3D sensors' working principle and a schematic of ARAN 9000 data collection vehicle. This system uses two 3D cameras and a laser to measure the surface coordinates.

Figure 17. Pave3D sensor working principal and ARAN 9000 specification

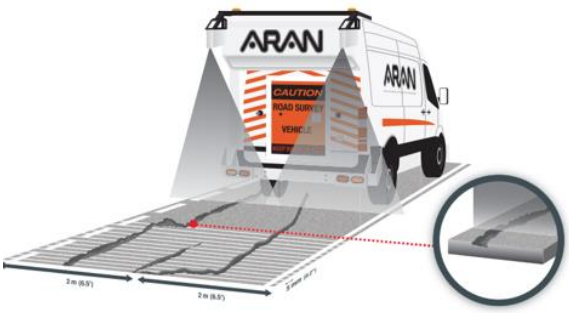

Vehicle Speed (Max):	62 mph (100 km/h)	50 mph (80 km/h)
• Sampling rate	5,600 profile/s	11,200 profile/s
• Profile spacing	5mm (0.2")	2.5mm (0.1")
• 3D points per profile	4,096 points	4,096 points
• Transverse field-of-view	4m (13 feet)	4m (13 feet)
• Depth range of operation	250mm (9.8")	250mm (9.8")
• Z-axis (depth) resolution	0.5mm (0.02")	0.5mm (0.02")
• X-axis (transverse) resolution	1mm (0.04")	1mm (0.04")

Upon completion of collecting 3D images at highway speed, the vendor uses its proprietary software to detect and quantify surface cracks of each type and severity. The

image processed cracking data are then transferred and stored in LA-PMS for each 0.1-mile pavement subsection surveyed. The vendor's image processing software uses a pattern recognition algorithm to classify the pavement cracks as alligator, longitudinal, or transverse cracking. Detailed reports and summary reports are produced after automated crack detection and classification. The detailed report contains the type, length, width, angle, extent, and severity level of each crack. On the other hand, the summary report includes the total length of different types of cracks and severity for a specific section. Usually for PMS, the vendor reports and summarizes the cracking data in a tenth of a mile subsection.

For this research, automated data for 50-ft. subsections were summarized and reported by utilizing the supporting software. The 0.1-mile data were collected directly from LA-PMS. There was a total of 323 data points for the 0.1-mile subsection and 2844 data points for the 50-ft. subsection. Each data point consists of the total number of cracks of different types, severity, and extent present in 0.1-mile or 50-ft. subsections. All the measurements were stored in the US system. Alligator cracking measurements were stored in ft^2. Both longitudinal and transverse cracking measurements were stored in feet.

Statistical Assessment of the Automated Cracking Measurements in LA-PMS

Accuracy of Automated Crack Detection

In general, two types of error may be produced by the automated system: a missing crack error and a false positive crack error [37]. Both the false positive and missing crack errors were used in the comparative analysis between automated and manual cracking measurements in this study. The false positive error is a ratio (in percentage) between the total number of sections of falsely-report-A-crack by the automated system to the total number of sections detecting no cracks by the manual operator [i.e., equation (7)]. The missed crack error is a ratio (in percentage) between the total number of sections of miss-detected-A-crack by the automated system to the total number of sections detected at least one crack by the manual operator [i.e., equation (8)].

$$False\ Positive = \frac{\sum_{i=1}^{n}(Manual=0, Auto>0)}{Total\ Sections} \times 100\% \quad (7)$$

$$Missed\ Crack = \frac{\sum_{i=1}^{n}(Manual>0, Auto=0)}{Total\ Sections} \times 100\% \quad (8)$$

Statistical parameters of error precision and error recall were also calculated using equation (9) and (10), respectively to evaluate the precision and accuracy of the automated system in a crack detection.

$$Error\ Precision = \frac{\sum_{i=1}^{n}(Manual=0, Auto>0)}{\sum_{i=1}^{n} Manual=0} \times 100\% \quad (9)$$

$$\text{Error Recall} = \frac{\sum_{i=1}^{n}(\text{Manual}>0, \text{Auto}=0)}{\sum_{i=1}^{n} \text{Manual}>0} \times 100\% \quad (10)$$

Ground-Truth Comparison for the 3D Cracking Measurements

At both a project level (a 50-ft. section based) and a network level (0.1 mile section based), statistical analyses were conducted between the 3D automated and the manual (ground-truth) cracking measurements for the selected pavement sections in this study.

Specially, two statistical parameters—the mean measurement error (STE) and the standard deviation of the measurement error (STD)—were computed based on equation (11) and (12), respectively. The mean measurement error refers to the average standard error produced by the automated system for each distress type as against the manual readings. A negative measurement error suggested the automated system under-estimated the measurements and vice-versa. The mean measurement error also represents the general estimation of the accuracy for the automated system.

$$STE = Y_i^{pred} - y_i^{meas} \quad (11)$$

$$STD = \sqrt{\frac{\sum_{i=1}^{n}(y_i^{pred} - y_i^{meas})^2}{n}} \quad (12)$$

Where,

STE = Standard Error of estimation

Y_i^{pred} = Automated Cracking Measurements.

Y_i^{meas} = Manual Cracking Measurements

n = Total number of data points.

In addition, two statistical tests below were conducted to verify the accuracy and precision of the automated system currently used by LA-PMS. In general, the lower the absolute value of the average standard error indicates that the automated system can be

better representative the results from manual measurements. The two hypothesis-based tests were described below:

- The t-test: A t-test with non-normally distribution was performed in this study on the mean measurement errors to verify the accuracy of the automated system. As shown in Figure 18, both manual and automated measurements were not normally distributed. The null hypothesis for the t-test is presented in equation (13):

$$H_0 : (Automated_{mean} - Manual_{mean}) = 0 \quad (13)$$

Figure 18. Distribution of the cracking measurements from automated and manual measurements at project level

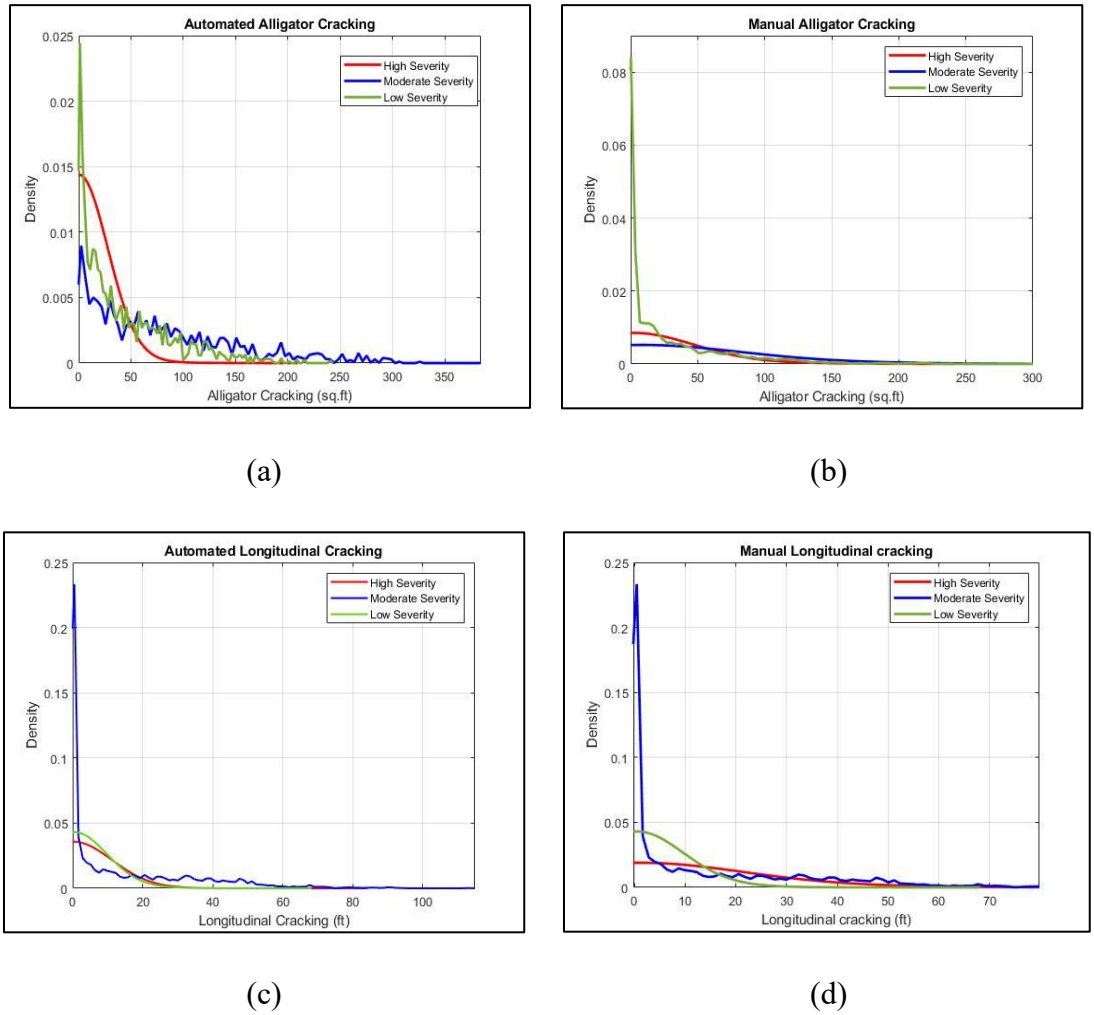

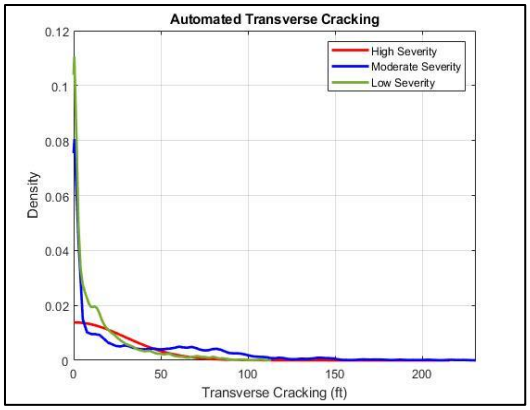

(e)

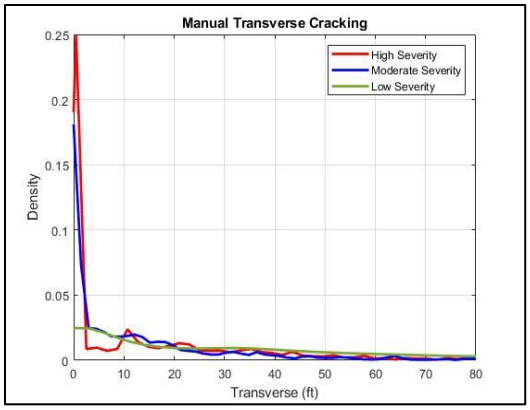

(f)

- Fligner-Kileen (FK) Test: FK statistical variance analysis was conducted to evaluate the precision of the automated system [59]. The FK is a nonparametric statistical test that evaluates the equality of variances of two datasets. The null hypothesis considered in this study is given below:

$$H_0 : (automated\ measurement\ variance) = (manual\ measurement\ variance)$$

This test is more useful when the variables are not normally distributed and contains high number of data outliers. In the analysis, the median of a dataset is first determined to find out the residuals of each measurement from the median. Then those residual values are ranked and normalized. A Fligner-Kileen statistic can be determined from the following formula:

$$FK = \frac{\sum_{i=1}^{j} n_i (x_i - x)^2}{Var^2} \quad (14)$$

Where, j = number of methods,

n_i = Size of the ith group.

x_i = mean of the normalized values for ith group.

x = mean of total normalized values.

Var = variance of the all normalized values.

FK statistics is used to determine the *p*-value. If p-value is less than the required significant level then the null hypothesis is rejected indicating the variances of the two dataset are statistically different from each other.

Development of ANN Cracking Prediction Model

The main goal of developing an ANN-based cracking prediction application in this study was to create a set of direct correlation links between the 3-D automated and the manual cracking measurements in order to adjust the less accurate automated cracking datasets in LA-PMS towards the manual measured cracking results. Selection of a proper architecture for an ANN model is the most important and complex task. In this study, a trial-version machine learning software application was used in the ANN's architecture design and a multilayered backpropagated feed-forward ANN model using three hidden layers was developed. The architecture of the developed ANN model is presented in Figure 19. As shown in Figure 19, the input layer considers fifteen input parameters including nine automated cracking measurements at each three severity levels, other surface conditions of rutting, IRI and mean profile depths (MPD), and the surface treatment type and service years as well the average temperature during the data collection. The output layer contains nine predicted measurements for the alligator, longitudinal, and transverse cracking of three severity levels.

Figure 19. Architecture of ANN model

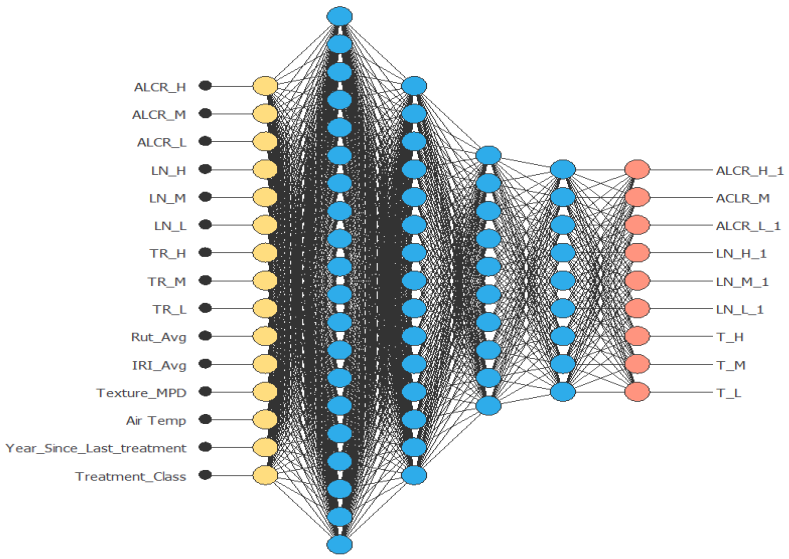

The ANN model was developed using the cracking measurements from 323 subsections (0.1 miles based) considered in this study. The measurement data of both the 3D automated and the manual were divided into three subsets: 55% for training, 30% for validation, and the remaining 15% data were used for testing. Such percentages of dataset breakdown were adopted after using a trial-and-error process in the model development

to reach an overall best performance of the ANN prediction model developed. Training of the ANN model can be described as the process through which the network deploys preliminary values and subsequently optimize the connection weights to achieve a global minimum instead of a local minimum [60]. As a longer training cycle can cause the model to over-fit, a maximum of 1000 iterations were allowed in this study. Furthermore, the training of the model was discontinued when the validation error was leveled. Validation of the ANN model is necessary to evaluate the robustness of the model. Upon completion of the training and validate phases, independent 15% of data was used to test the proposed ANN model with respect to the accuracy in predicting the alligator, longitudinal, transverse cracking at each severity level. With that in mind, the correlation coefficient *R,* Coefficient of determination R^2, Root Mean Square Error (RMSE) and Mean Absolute Error (MAE) of the ANN-predicted cracking measurements were used to evaluate the predicted cracking measurements. The RMSE and MAE were calculated using the following equations.

$$RMSE = \sqrt{\frac{1}{n}\sum_i^n \left(Y_i^{pred} - Y_i^{meas}\right)^2} \tag{15}$$

$$MAE = \frac{1}{n}\sum_i^n \left|Y_i^{pred} - Y_i^{meas}\right| \tag{16}$$

Where,
Y_i^{pred} = Predicted Cracking Measurements.
Y_i^{meas} = Manual Cracking Measurements
n = Total number of data points.

Indices Analysis of Cracking Measurements in LA-PMS

The ALCR (alligator cracking) and RNDM (random cracking) indices were calculated using equations (1) and (2). Pairwise T-statistical test was performed to check if there is any significant difference between automated indices and manual or ground truth indices. Similarly, a pairwise t-test was also conducted between the indices from ANN-predicted measurements and manual measurements. T-test was performed as it uses sample standard deviation instead of population standard deviation which will allow to qualitatively evaluate the precision of ANN-predicted and automated indices. Moreover, t-tests results for ANN-predicted and automated indices were compared against each other.

Monte Carlo simulation was used to evaluate the changes in the overall pavement condition index (PCI) due to errors from automated and ANN-predicted indices. Equation (3) was modified to find out the changes in PCI. This analysis uses a sequence of random numbers and uses the error result from each system to create a probability density function (PDF). Cumulative Density Function (CDF) is then estimated from the PDF. Monte Carlo simulation uses a random sampling technique from the CDF to produce the change in PCI due to error in each system.

In PCI calculation, only ALCR and RNDM parameters were used. So, for this analysis, errors from ALCR and RNDM produced by automated and ANN-predicted measurements were utilized. The following describes the procedure of using Monte Carlo simulation in the PCI calculation:

- Error from each parameter can be computed from equation (16):

$$Error = y_i^{pred} - y_i^{meas} \tag{16}$$

Where, y_i^{meas} denotes the ALCR or RNDM from manual measurements and y_i^{pred} denotes the ALCR and RNDM from automated or ANN-predicted measurements.

$$PCI_M = \mathrm{MAX}(\mathrm{MIN}(\mathrm{RNDM}, \mathrm{ALCR}, \mathrm{PTCH}, \mathrm{RUFF}, \mathrm{RUT})_M, [\mathrm{AVG}(\mathrm{RNDM}, \mathrm{ALCR}, \mathrm{PTCH}, \mathrm{RUFF}, \mathrm{RUT})_M - 0.85\ \mathrm{STD}(\mathrm{RNDM}, \mathrm{ALCR}, \mathrm{PTCH}, \mathrm{RUFF}, \mathrm{RUT})]_M) \tag{17}$$

$$PCI_A = \mathrm{MAX}(\mathrm{MIN}(\mathrm{RNDM}, \mathrm{ALCR}, \mathrm{PTCH}, \mathrm{RUFF}, \mathrm{RUT})_A, [\mathrm{AVG}(\mathrm{RNDM}, \mathrm{ALCR}, \mathrm{PTCH}, \mathrm{RUFF}, \mathrm{RUT})_A - 0.85\ \mathrm{STD}(\mathrm{RNDM}, \mathrm{ALCR}, \mathrm{PTCH}, \mathrm{RUFF}, \mathrm{RUT})]_A) \tag{18}$$

Where, subscripts M and A denote manual results and automated or ANN-predicted results, respectively.

To evaluate the effect of each parameter on PCI change, all the other parameters except for the one under review were set to 0. Equations (19) and (20) describe the change in PCI due to ALCR and RNDM error, respectively:

$$\Delta PCI_{ALCR} = MAX(MIN(0, ALCR_{Error}, 0, 0, 0), [AVG(0, ALCR_{Error}, 0, 0, 0) - 0.85\ STD(0, ALCR_{Error}, 0, 0, 0)]) \tag{19}$$

$$\Delta PCI_{RNDM} = MAX(MIN(RNDM_{Error}, 0, 0, 0, 0), [AVG(RNDM_{Error}, 0, 0, 0, 0) - 0.85\, STD(RNDM_{Error}, 0, 0, 0, 0)]) \quad (20)$$

Errors from automated and ANN-predicted ALCR and RNDM indices were calculated using equation (16) for each data point. Equations (19) and (20) were then used for constructing a CDF for Monte Carlo analysis. Random numbers between 0 to 100 were generated, which allowed ΔPCI_{ALCR} and ΔPCI_{RNDM} to be determined from CDF. Monte Carlo simulation provides a mean and standard deviation of the change in PCI due to error from ALCR and RNDM indices. Mean and standard deviation of ΔPCI_{ALCR} and ΔPCI_{RNDM} from automated and ANN-predicted measurements have been evaluated against each other.

Development of Automated Crack Survey Application for DHDV$_{LTRC}$

As described in the Introduction, LTRC owns a DHDV$_{LTRC}$ system for collecting research based pavement condition data including high resolution 2D pavement surface images at highway speeds. This portion of the research describes the development of a prototype imaging processing software for DHDV$_{LTRC}$ using an open source algorithm called Random Structured Forests in MATLAB to detect, classify, and measure the cracking distresses automatically based on high resolution 2D images. MATLAB is a proprietary multi-paradigm programming language and numeric computing environment developed by MathWorks [61].

Shi et al. [62] developed the 'CrackForest' framework based on the Random Structured Forests algorithm. Developers of the CrackForest application divided the framework into three major parts: (1) Feature extraction by integrating channel features—feature extraction allowed the developers to represent cracks with a higher level of structural information, (2) Introduction of Random Structured Forest [63] to obtain preliminary information on crack detection, and (3) Using of Crack Descriptor which can characterize the cracks. They applied a classification algorithm to separate cracks from noise.

Figure 20. Manually drawn contour lines in the image patches to identify crack regions [61]

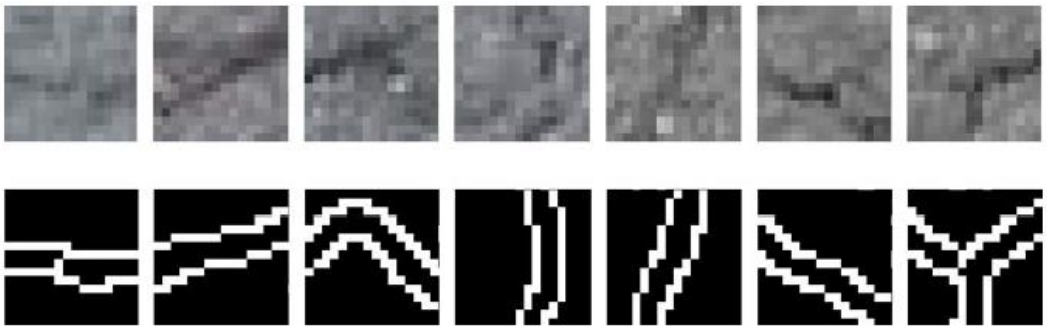

Figure 20 shows the mechanism of selecting the training dataset for the ‘CrackForest’ application. Researchers divided the images with pavement cracks to create small image patches and manually draw contour lines along the crack edge. These small image patches were then used as the training dataset to extract crack features and crack edge detection process.

Upon completion of the crack detection, images were stored in a separate folder, and a crack classification algorithm was applied to classify cracks. The classification criteria were kept simple for these research purposes. Matlab's’ image processing toolbox was used to develop the crack classification and measurement algorithm. Interconnected cracks were classified as alligator cracking and reported in ft^2. Cracks that were predominately parallel to the traffic direction and/or pavement centerline were reported as longitudinal cracking and reported in linear ft. Cracks that were predominately perpendicular to the pavement centerline were reported as transverse cracking and reported in linear ft.

Discussion of Results

For the nine calibration control sites, both the 2D and 3D automated cracking data on 0.1-mile subsections as well as the vendor 3D-camera collected pavement images were obtained from DOTD's pavement management system engineers. In collecting various pavement cracking distress data for selected flexible pavement test sections, the 3D automated cracking measurements of every 0.1-mile were retrieved from the 2017 LA-PMS pavement condition database. Furthermore, datasets of 50-ft. based subsections for the 3D automated cracking measurements were generated by the research team using the vendor provided imaging software. In addition, manual pavement cracking measurements were obtained using the aforementioned semi-auto method on all calibration sites and flexible pavement test sections considered. In total, there were 2,844 cracking measurement subsections of 50 ft. each for the flexible pavement test sections and 45 subsections of 0.1 mile each for the calibration sites used in this study. The following presents the details of the 2D/3D automated and the manual cracking measurement data analysis and software applications developed.

Comparison of 2D and 3D Automated Cracking Measurements

The following presents a direct comparison of the vendor's two automated imaging systems (2D and 3D) collected cracking on the DOTD's nine calibration pavement sites using the manual measurements as the ground truth.

Comparison on Total Measured Crack Quantities

Table 10 presents the total quantity results for the alligator, longitudinal, and transverse cracks measured on the nine pavement sites using the three cracking survey methods (2D, 3D, and the manual). As can be seen in Table 10, by comparing to the manual survey results, the 2D system generally slightly over-reported the alligator cracks, under-reported the transverse cracks, but largely under-reported the longitudinal cracking by approximately 30 percent on the total measurements of nine testing sites surveyed. On the other hand, the 3D measurements were found to provide a similar total alligator cracking measurement as that from the manual survey, but slightly under-reported the longitudinal cracking and over-predicted the transverse cracking. Overall, the 2D system seems to under-estimate the total longitudinal and transverse crack lengths as compared to those obtained by the 3D system.

Table 10. Total results of cracking measurements on nine calibration sites

Cracking Type	Manual	2D-Automated	3D-Automated	% Difference between 2D and Manual	% Difference between 3D and Manual	% Difference between 2D and 3D
Alligator (ft^2)	26,596	27,202	26,221	**2.3%**	**-1.4%**	**3.7%**
Longitudinal (ft.)	21,431	14,968	19,837	**-30.2%**	**-7.4%**	**-24.5%**
Transverse (ft.)	20,279	18,696	22,562	**-7.8%**	**11.3%**	**-17.1%**

Comparison on Individual Measured Crack Quantities

Figure 21 presents the individual cracking measurements on each pavement site surveyed. Figure 21(a) shows that the alligator cracking were measurable only on sites 6, 7, 10, and 13. In general, the alligator cracking measurements from manual rating and 3D system visually matched with each other. On the other hand, the 2D system tended to either over- or under-predicted the alligator cracking significantly. Figure 21(b) shows the individual longitudinal cracking measurement results of test sections. As can be viewed in Figure 21(b), both the 2D and 3D automated measurements tended to under-predict the longitudinal cracking with the 2D results showing a significant under prediction on both site 3 and site 5. In term of the overall transverse cracking quantity measured on each test section, Figure 21(c) indicates that the automated 3D measurement appeared to over-report the overall transverse cracking quantity; whereas, the 2D data showed a mixed-bag results as comparing with the manual transverse cracking measurements.

Figure 21. Comparison of cracking measurements at each control site (a) alligator (b) longitudinal and (c) transverse cracking measurements

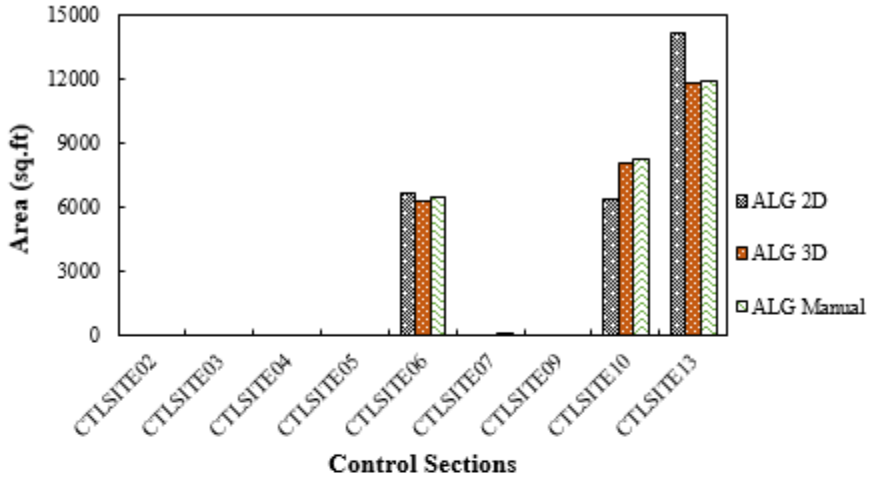

(a)

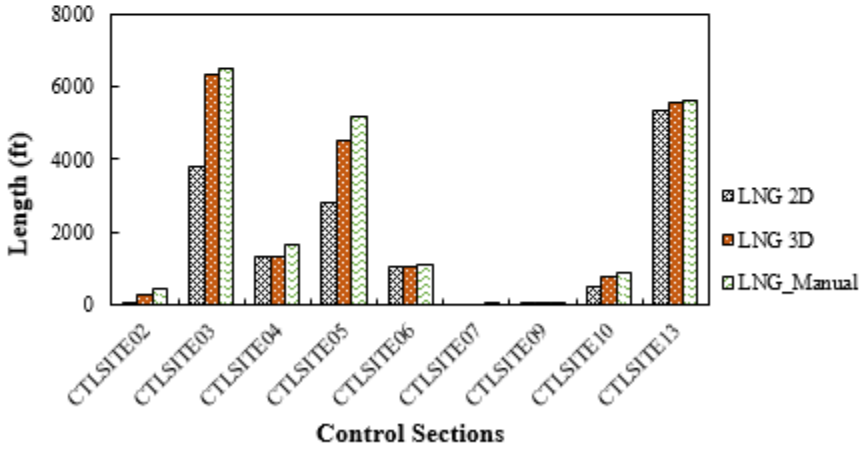

(b)

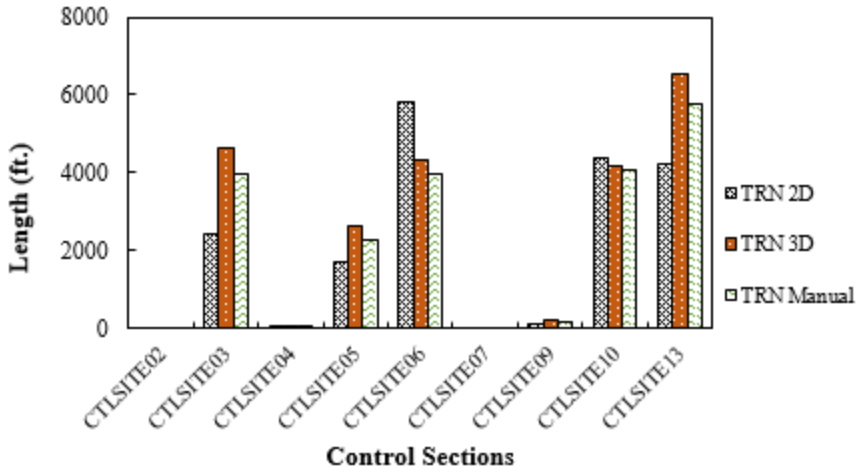

(c)

Comparison on Crack Severity

A further breakdown comparison in various cracking severity levels (i.e., high, moderate, and low) was performed based on the imaging and manual collected cracking measurements on the calibration pavement sites. Figure 22 shows the measurement comparison for the three cracking types (i.e., alligator, longitudinal and transverse) illustrated by a pie-chart. In general, in terms of the absolute measured crack quantities at different severity levels, the 3D measurements showed slightly more matching (or closer) values to the manual survey values than the 2D measurements (Figure 22). With an exception in 3D high transverse cracking measurement, both 2D and 3D underestimated all other high-level cracking measurement quantities, as shown in Figure 22. On the other hand, the 3D measurements appeared to over report the crack quantities at a moderate level but under-predict at a low severity level (except for the 3D low transverse cracking measurements). In addition, all 2D collected cracking quantities were found to under estimate moderate level cracks but tend to over report the amounts of low alligator and transverse cracking.

In terms of the measured alligator cracking breakdown percentages, the considered 3D system detected, respectively, 2%, 73% and 25% of the high, moderate and low severity alligator cracks, which were comparable to those values (3%, 69%, and 28%, respectively) obtained from the manual alligator cracking survey. However, the 2D system was found to have over-predicted the percentage of low alligator cracks (i.e., 40%) and under reported the percentage of moderate alligator cracks (i.e., 59%) for the calibration pavement sites surveyed (Figure 22).

For the breakdown percentages in transverse cracking measurements, the 2D system followed a similar trend as the comparison showed in alligator cracking measurements. The 2D results were found to overestimate low severity transverse cracks (i.e., 45% vs. 34% of the manual survey) and under report moderate severity of 48% transverse cracking as compared to manual measurements of 57%. On the other hand, 3D system detected respectively, 9%, 56% and 35% of the high, moderate and low severity transverse cracks, which were similar to those values obtained from the manual transverse cracking survey results (Figure 22).

In terms of those the breakdown percentages for longitudinal cracking measurements, however, similar percentages at three severity levels were obtained for all three cracking survey systems or methods considered in this study. As shown in Figure 22, both 2D and 3D systems detected 7% high severity longitudinal cracking compared to the 10% of manual measurements. There were 23%, 29%, and 28% moderate severity cracking detected by manual, 2D system and 3D system respectively. And 67% low severity cracking was detected by the manual rating compared to the 64% and 65% detected by 2D and 3D system, respectively.

Overall, the 3D system showed an improved cracking identification and measurement results over the 2D system studied. This is promising since the LA-PMS cracking data has been collected by the 3D system since 2017. However, an accuracy analysis for the 3D system is still needed in order to improve the LA-PMS collected cracking data to be potentially used in a project level pavement performance analysis. The following section describes the results of the accuracy analysis for the 3D automated system considered.

Figure 22. Crack measurements results at different severity level for calibration control sites

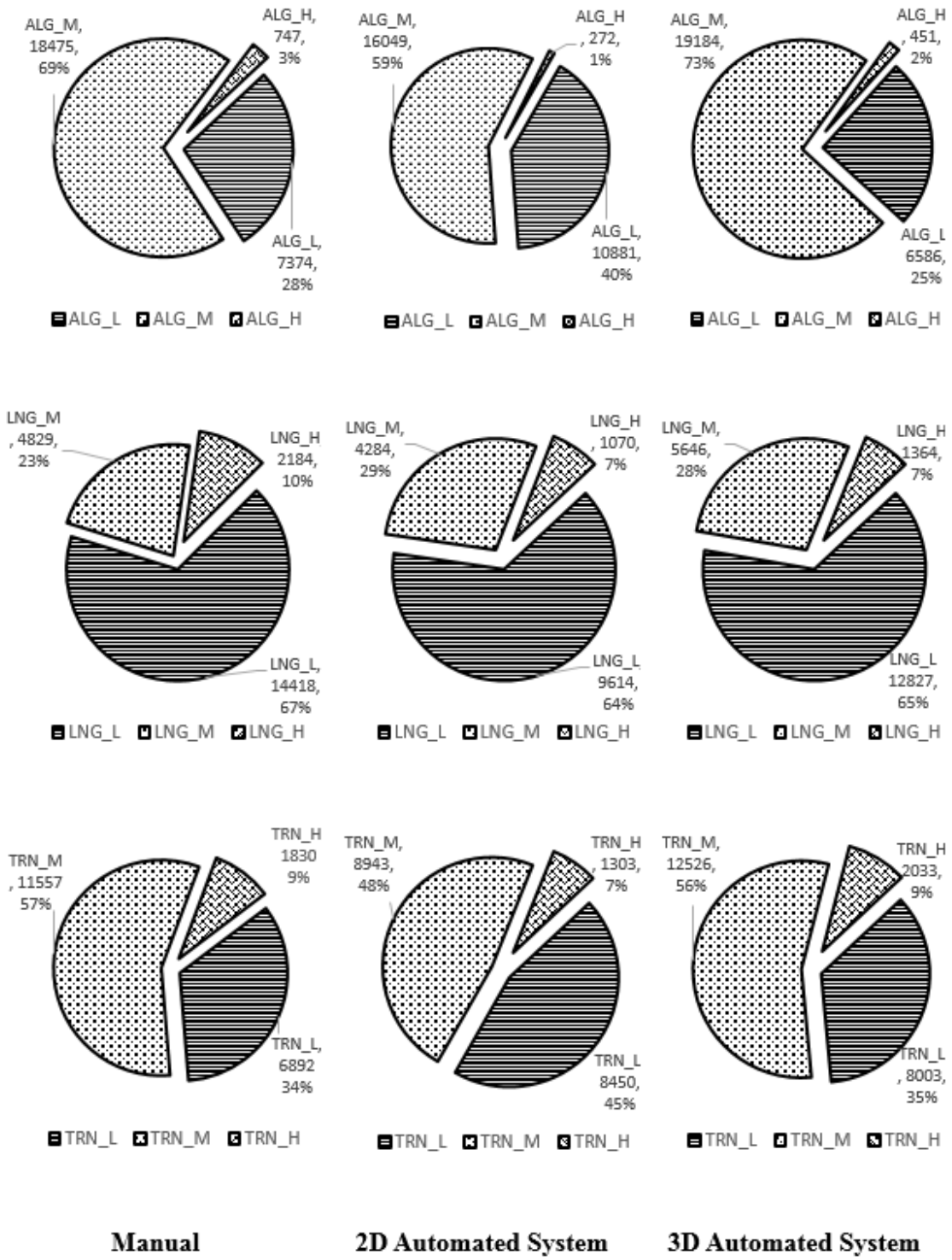

Performance of the 3D Automatic Crack Detection

To evaluate the crack detection performance for the current vendor's 3D imaging software used by the LA-PMS for collecting the automated cracking measurements, four statistical measures (false positives, missed cracks, precision, and recall) were computed using the 3D automated and manual cracking measurements collected on all 23 flexible pavement test sections considered in this study. This analysis was based on the measurements of 50-ft. subsections and a total of 2844 subsections were evaluated. Cracking measurements at high, moderate, and low severity for each crack type (alligator, longitudinal, and transverse) were combined in this analysis. Again, the manual survey measurements were considered as the ground truth reference values.

Table 11 represents a summary report of various number of sections of the values that are used in the crack detection accuracy evaluation of the automated system. Manual = 0, Auto > 0 column represents the number of sections where the manual system did not detect a crack, but the automated system detected at least one crack. Manual > 0, Auto = 0 column represents the number of sections where the manual system detected at least one crack, but the automated system did not detect any crack. Manual = 0 and Manual > 0 columns represent the number of sections; the manual system did not detect a crack and manual system detected at least.

Table 11. Automated system crack detection accuracy calculation

Cracking Type	Total Test Sections	False Positive Sections (Manual=0 Auto>0)	Missed Cracks Sections (Manual>0 Auto=0)	No Detectable Crack Sections (Manual = 0)	Detected Minimum One Crack Sections (Manual > 0)
Alligator	2844	241	141	1042	1802
Longitudinal	2844	280	225	1086	1758
Transverse	2844	249	41	862	1982

Figure 23 represents the percentages of false positive, missed cracks, precision, and distress sensitivity (recall) errors produced by the automated system. False positive error is the ratio (in percentage) between the number of sections of falsely-report-A-crack by the automated system and the total number of sections. Missed crack error is the ratio (in

percentage) between the number of sections of missed-detected-A-crack by the automated system and the total number of sections. Precision error is the percentage of non-cracked sections where the automated system at least detected one crack, and the distress sensitivity error (Recall) is the percentage of cracked sections where the automated system did not detect any crack. Equations (7-10) were used to calculate %False Positives, %Missed Cracks, %Precision, and %Recall of the automated system.

For example, among 2,844 subsections of flexible pavements, the automated system measured alligator cracking in 241 subsections, but the manual system did not detect any alligator cracks in those subsections. So, the total percentage of false positives error produced by the automated system using equation (7) is 8.5%. Subsequently, among 2,844 subsections, the manual system measured alligator cracking in 141 subsections, but the automated system did not detect any. Thus, the total percentage of missed crack error produced by the automated system is 5.0%. On the other hand, the manual system did not detect any alligator cracks in 1042 subsections, but the automated system detected alligator cracks in 241 of them. So, the total %Error Precision produced by the automated system is 23.1%. Subsequently, the manual system detected alligator cracking in 1802 subsections, but the automated system did not detect any in 141 of them. So, the %Error Recall produced by the automated system is 7.8%.

Figure 23. False positives, missed cracks, precision, and distress sensitivity (recall) in comparison with manual measurements

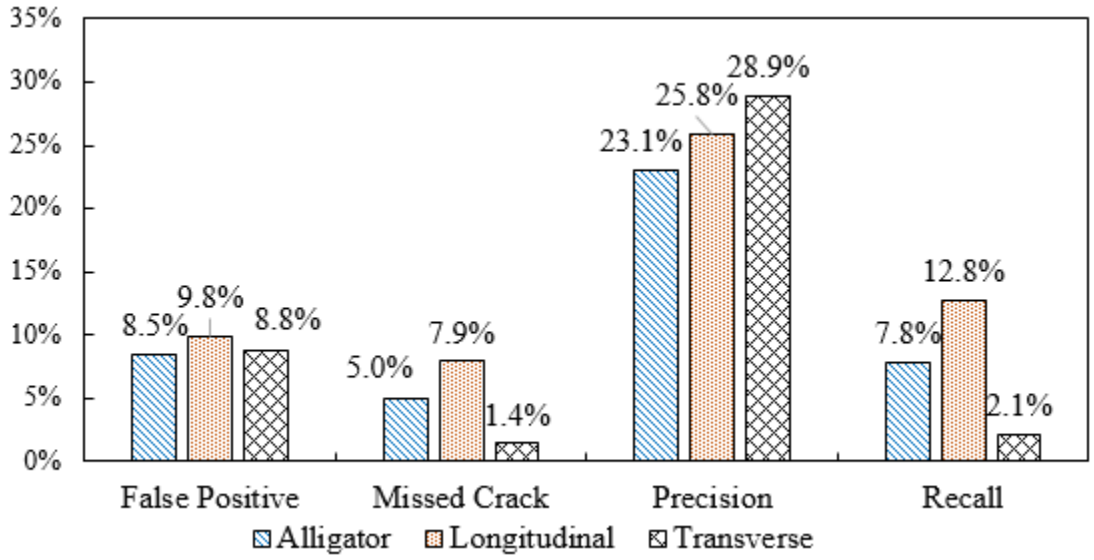

Figure 24(a) shows that, due to the oil stains presented in the considered section, the automated system falsely identified three cracks. On the other hand, Figure 24(b) shows that even though a longitudinal crack is clearly visible at the right wheel path, the automated system did not detect the crack. One reason for these errors produced by the automated system may lie in the fact that the illumination, pavement marks, shadows, and humidity are continuously changing during pavement condition surveys.

Figure 24. (a) False positive and (b) missed crack error produced by automated system

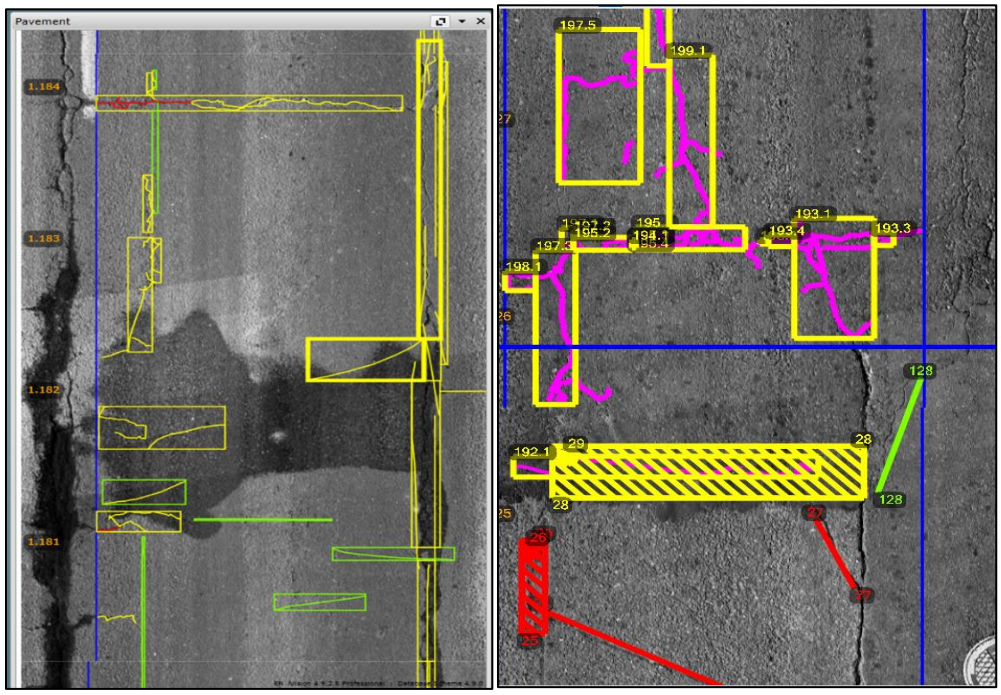

(a) (b)

In general, it can be observed in Figure 23 that highest percentages of false positives and missed cracks are the longitudinal cracking. Moreover, %Error Precision was greater than 20% for all crack types suggests that, automated system tend to report cracking distress in the non-cracked sections. This is as expected, since computer software may miss-identify a fallen object or sealed crack as longitudinal cracking, or longitudinal cracking may be miss-counted due to the strict algorithm followed by the software. It should be noted that the vendor and DOTD's pavement engineers performed additional manual post-checking of the cracking measurements during the DOTD's 2019 data collection cycle. Therefore, those percentages of false positive and missed cracks may have been significantly reduced in DOTD's 2019 LA-PMS database.

Accuracy and Precision Analysis of the 3D Automated Crack Measurements

The crack measurement accuracy and precision for the vendor's 3D automated system are evaluated in this section using the measurement cracking data collected in the selected 23 flexible pavement sections. Both a project level analysis (based on 50-ft. subsection measurements) and a network-level analysis (based on 0.1-mile subsection measurements) were performed. Three types of automated cracking measurements (i.e., alligator, longitudinal, and transverse) at each severity level were compared against the reference manual measurements. Note that only the subsections for which both the automated system and the manual detected cracking were considered in the analyses.

Cracking Measurements on 50-ft. Subsections

Table 12 presents a summary of the accuracy and precision analysis for the 3D automated cracking measurements based on the selected 50-ft. subsections. The "Mean" and "Median" columns in Table 12 are the means and medians of the measurement values obtained from both the 3D automated and manual methods. In general, all mean values differ from the corresponding medium values. This is expected as the cracking distresses of the selected pavement projects are not necessary to follow the uniform or a normal distribution. The means of the 3D automated cracking measurements are also found different from the means of the manual measurement results for all cracking types.

For each subsection, a measurement error was first calculated as the difference between the 3D automated and the manual measurements. The "Mean Measurement Error" column in Table 12 lists an overall average of all subsection measurement errors for each type of cracking measurement produced by the 3D automated system; whereas, the "Standard Deviation of the Error" column gives the standard deviation of all subsection measurement errors of each type. While the mean measurement error is the estimate of accuracy for the 3D automated measurement system (a positive signed error suggests an overestimation and vice versa), a standard deviation of the error is indicative of the 3D measurement precision. Generally, the smaller a mean measurement error, the more accurate of the 3D automated system. One the other hand, the greater a standard deviation of the error, the more variation of the 3D measurements, indicating the imprecision of the measurement system and vice versa. For example, as can be seen in Table 12, the 3D automated system tended to underestimate the high severity alligator cracking with an accuracy of 24.57 ft^2 and a precision of 35.80 ft^2 on a 50-ft. long pavement section.

Overall, the results shown in Table 12 indicate that, in term of accuracy, the 3D automated system can significantly over-estimate the amounts of cracks at a moderate severity level with positive errors of 49.09 ft^2, 9.04 ft., and 24.86 ft. for the alligator, longitudinal, and transverse measurements, respectively. The 3D system was also found slightly over-estimated in the low and high severity transverse cracking. On the other hand, the 3D measurements generally under-reported other crack amounts at high or low severity levels for both alligator and longitudinal cracks with negative errors ranged from (-3.59) ~ (-11.01) in feet and (-2.8) to (-24.57) in square feet, respectively, over a 50-ft. long pavement section. The precision errors of the 3D measurements generally showed a similar level of magnitude as the accuracy errors.

Table 12. Summary results of the quantification error produced by the automated based on 50-ft. subsections

Crack Type	Severity Level	Mean		Median		Mean Measurement Error (Accuracy estimate)	Standard Deviation of the Error (Precision estimate)
		Automated	Manual	Automated	Manual		
Alligator (ft^2)	High	30.74	55.30	25.47	35.93	-24.57	35.80
	Moderate	108.26	59.16	92.38	41.00	49.09	58.71
	Low	48.72	51.52	34.87	37.99	-2.80	45.71
Longitudinal (ft.)	High	8.63	19.65	4.85	17.24	-11.01	14.32
	Moderate	25.13	16.09	21.26	11.79	9.04	14.47
	Low	6.22	9.81	4.33	7.68	-3.59	7.51
Transverse (ft.)	High	28.60	26.04	27.43	22.67	2.65	18.72
	Moderate	57.46	32.60	53.49	25.40	24.86	31.99
	Low	18.74	17.21	12.36	12.01	1.53	17.41

Figure 25 presents the scatter plots for automated and manual alligator cracking measurements at each severity level. From Figure 25, it can be observed that at all

severity levels, when the crack amounts are low, data points are close to the identity line. However, with the increase in crack measurements, points are dispersed up and below the identity line. At each severity level for all crack types, with the increase of pavement cracking, the accuracy of the automated system tends to reduce. Figure 25 also shows that the correlations between automated and manual measurements are generally poor with R^2 values approximately ranging from 0.15 to 0.47 for all cracking measurements considered.

Figure 25. Scatter plot of automated vs manual cracking measurements on 50-ft. (a) alligator cracking (b) longitudinal cracking and (c) transverse cracking

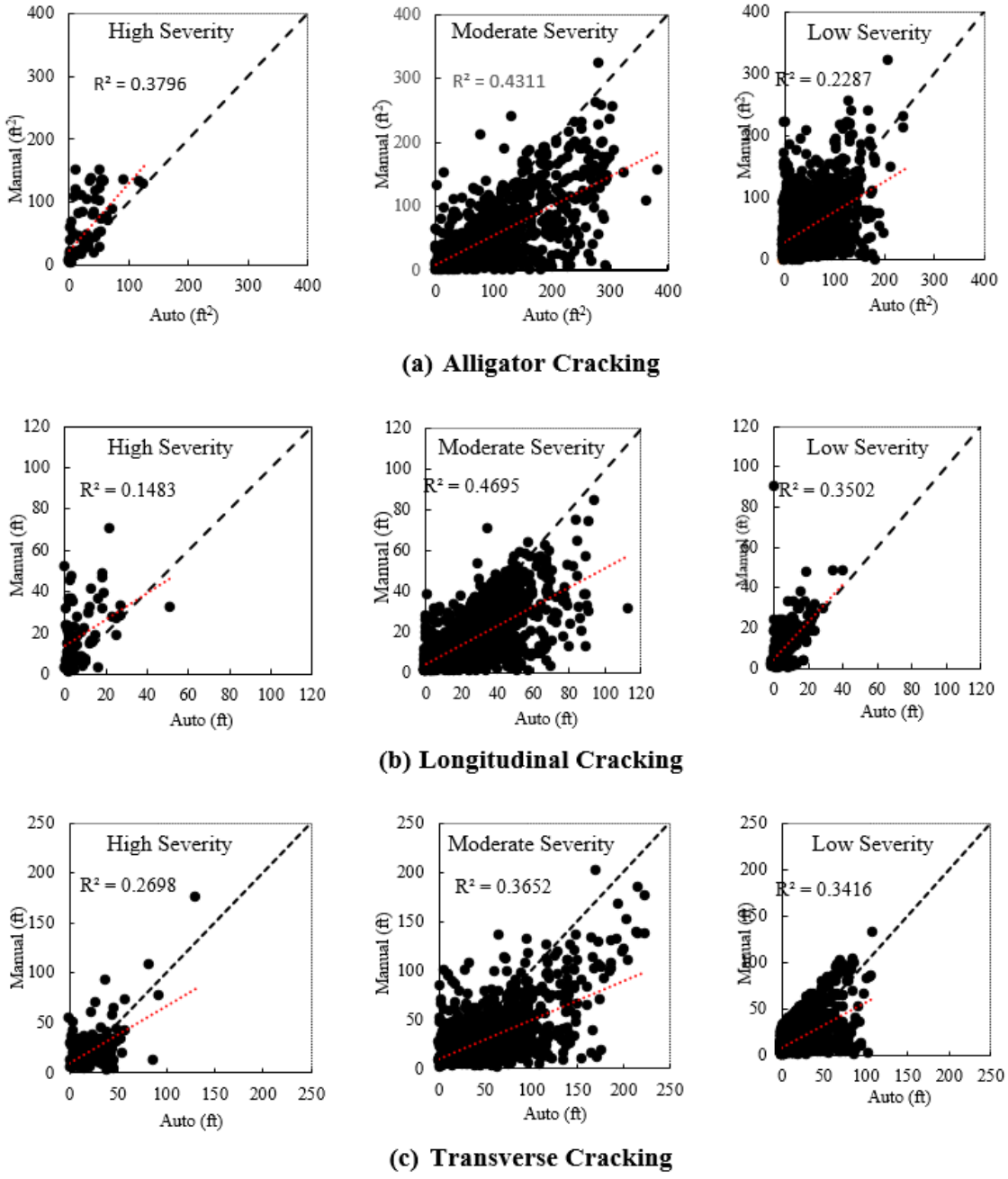

As it was previously established, none of the cracking measurements from automated and manual measurements were normally distributed and most of the data reside in the first quartile range. T-test statistical analysis at a significant level of 95% was conducted to evaluate the accuracy of the automated system. Measurement error occurred from the automated system was used for this analysis, which evaluated two hypotheses of H_0 *(Null*

Hypothesis): Mean Measurement Error = 0, and H_1 (Alternative Hypothesis): Mean Measurement Error ≠ 0. When the resulted *p*-value < 0.05, reject the null hypothesis of no measurement error.

A t-test with non-normally distribution at a significant level of 95% was performed in this study on the mean measurement errors to verify the accuracy of the 3D automated cracking measurements. Table 13 presents the t-test results. It can be observed that, except for high severity transverse cracking, there is a significant difference between the automated and manual cracking measurements for all crack types at all severity levels. Although the t-test indicates there is no statistically significant difference between the 3D automated and the manual results on the high severity transverse cracking measurements, however, it was found by viewing Figure 25(c) that the two datasets of high severe transverse cracking were not correlated each other with a R^2-value of only 0.27, indicating they are differed practically in most of the test sections considered. The t-test results generally confirmed the accuracy estimates in terms of the 3D mean measurement errors shown in Table 12.

Table 13. T-test on measurement errors results for 50-ft. subsections

Crack Type	Severity Level	Actual Mean	Number of Subsections	Degree of Freedom	t-Statistic	*p*-Value	Significance
Alligator (ft^2)	High	-24.57	73	72	5.86	<0.0001	Yes
	Moderate	49.09	802	801	23.68	<0.0001	Yes
	Low	-2.80	1259	1258	2.18	0.0298	Yes
Longitudinal (ft.)	High	-11.01	69	68	6.38	<0.0001	Yes
	Moderate	9.04	1344	1343	22.90	<0.0001	Yes
	Low	-3.59	375	374	9.27	<0.0001	Yes
Transverse (ft.)	High	2.65	154	153	1.68	0.92	**No**
	Moderate	24.86	1248	1247	27.45	<0.0001	Yes
	Low	1.53	1519	1518	3.43	0.0006	Yes

Fligner-Kileen statistical analysis was conducted to qualitatively evaluate the variation (or precision) of the 3D automated cracking measurements at each severity level. Fligner-Kileen analysis is a hypothesis test that estimates the homogeneity of variances for two or more groups. It is more useful than other equality of variance tests as it takes non-normality and the presence of outliers into account. The Fligner-Kileen analysis evaluated two hypotheses of H0 (Null Hypothesis): Automated cracking Variance = Manual cracking Variance, and H1 (Alternative Hypothesis): Automated cracking Variance ≠ Manual cracking Variance. When the resulted in p-value < 0.05, reject the null hypothesis, indicating the variances of the 3D automated and manual measurements are statistically different. Figure 14 illustrates the results from Fligner-Kileen analysis. It can be observed in Table 14, except for low severity alligator cracking, the 3D automated cracking measurements generally showed higher variation (or less precision) as compared to those manual measurements. This also agreed by large with the standard deviation of the errors (or the estimate for precision) shown in Table 12.

Table 14. Summary of Fligner-Kileen analysis for 50-ft. subsections

Crack Type	Severity Level	Number Methods, (n)	Degree of Freedom, (n-1)	FK-Statistic	P-value	Significance
Alligator (ft^2)	High	2	1	25.8	3.83E-07	Yes
	Moderate	2	1	96.4	9.24E-23	Yes
	Low	**2**	**1**	**0.1**	**0.72**	**No**
Longitudinal (ft.)	High	2	1	16.5	4.83E-05	Yes
	Moderate	2	1	77.6	1.24E-18	Yes
	Low	2	1	39.3	3.62E-10	Yes
	High	2	1	860.13	4.6E-19	Yes
	Moderate	2	1	270.79	7.6E-61	Yes

Crack Type	Severity Level	Number Methods, (n)	Degree of Freedom, (n-1)	FK-Statistic	P-value	Significance
Transverse (ft.)	Low	2	1	67.62	1.9E-16	Yes

Cracking Measurements on 0.1-mile

Table 15 represents an overall cracking measurement comparison (without considering the cracking severity) between the 3D and the manual methods for a total of 28.6-mile long of the 23 flexible pavement test sections rated in this study. Note that the total cracking quantities in Table 15 were based on 0.1-mile subsections. As shown in Table 15, the 3D automated cracking generally overestimated the total alligator, longitudinal, and transverse cracking by 32.8%, 8.5%, and 27.7%, respectively, over the surveyed pavement length of 28.6 miles in this study.

Table 15. Summary results of automated vs. manual system at network-level

Total Miles Covered	Crack Type	Automated System	Manual System	% Difference between Automated and Manual
28.6	Alligator (ft^2)	216,073	162,657	**32.8%**
	Longitudinal (ft.)	44,990	41,455	**8.5%**
	Transverse (ft.)	127,936	100,214	**27.7%**

In terms of the accuracy and precision for the 3D automated cracking measurements in a network-level data analysis, a summary of quantification error results based on 286 subsections of 0.1-mile each are presented in Table 16. Similar to Table 12, the “Mean” columns represent the means of the measurement values obtained from both the 3D automated and manual methods. In general, Table 16 shows that large discrepancies were observed for all mean values between the 3D and the manual measurements based on the 0.1-mile measurement subsections. This implies that the accuracy of the 3D cracking measurements may still need to be improved for using the PMS data in a decision making of treatment selection or the calibration of pavement design models. The mean

measurement errors echoed the inaccuracies of the means, which are similar to those in Table 12. In general, the variations (less precision) of 3D measurements are also increased at all severity level cracking measurements compared to those in Table 12. This may be due to the length of measurement subsection changed from 50 ft. to 0.1 mile.

Table 16. Summary results of the quantification errors produced by the automated system based on 0.1-mile subsection

Crack Types	Severity Level	Mean		Mean Measurement Error (Accuracy estimate)	Standard Deviation of the Error (Precision estimate)
		Automated	Manual		
Alligator (ft^2)	High	1846.1	18067.2	-50.1	114.2
	Moderate	133335.6	52219.6	250.4	348.0
	Low	81560.4	92873.7	-34.9	203.4
Longitudinal (ft.)	High	877.4	9266.1	-26.0	60.3
	Moderate	38143.7	25172.3	40.2	89.4
	Low	5969.1	7016.9	-3.2	18.9
Transverse (ft.)	High	5267.1	13619.6	-25.9	79.9
	Moderate	89420.0	48445.5	126.9	204.3
	Low	33249.2	38149.6	-15.2	90.5

To further investigate the comparisons between the 3D automated and the manual cracking measurements on 0.1-mile subsections, Figure 26 shows a breakdown of the cracking measurements at each severity level and Figure 27 presents the scatter plots of those measurements.

Figure 26. Crack measurements by severity level for automated and manual system (a) alligator cracking (b) longitudinal cracking and (c) transverse cracking

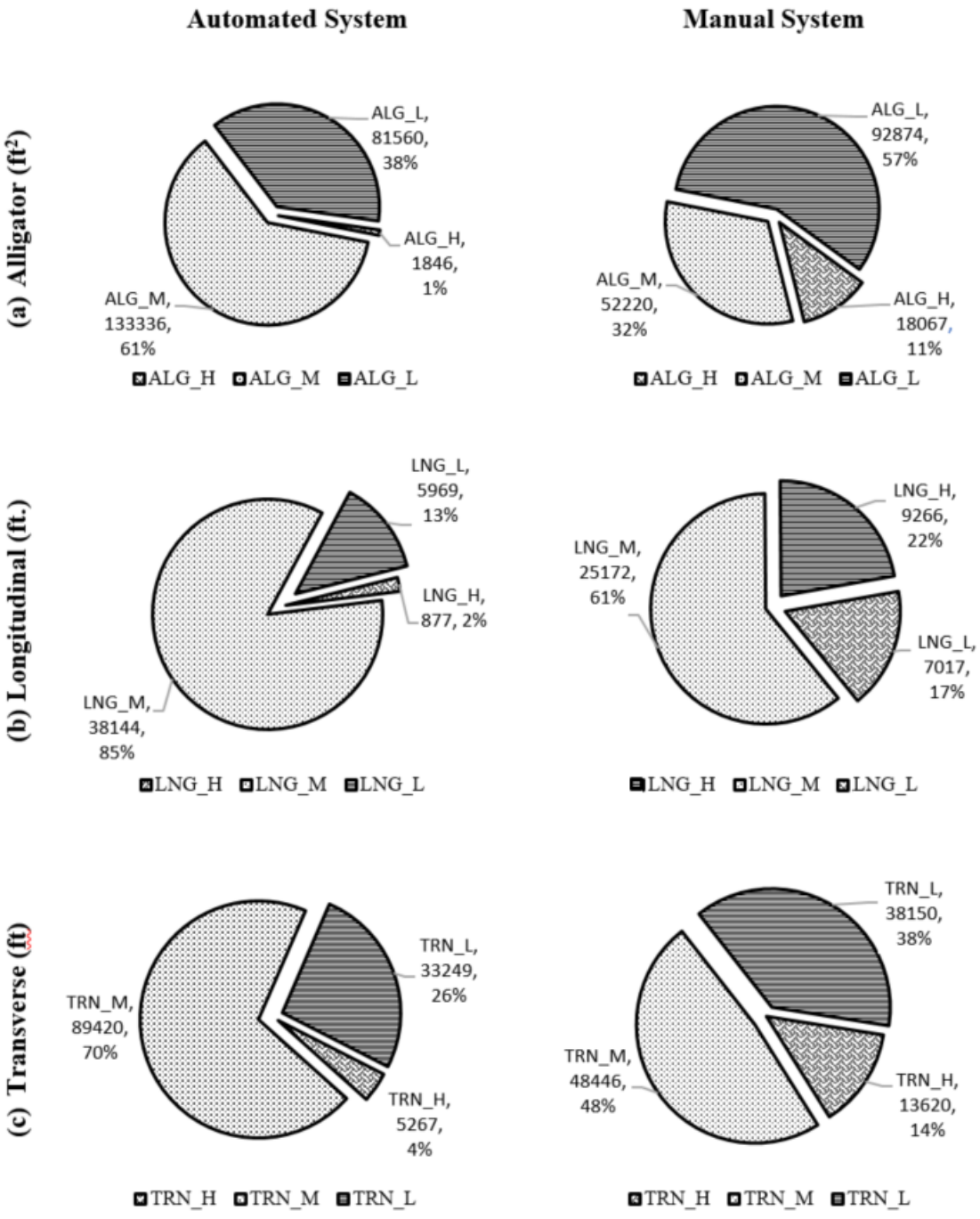

Figure 27. Scatter plot of automated vs manual transverse cracking measurements (a) alligator cracking (b) longitudinal cracking and (c) transverse cracking

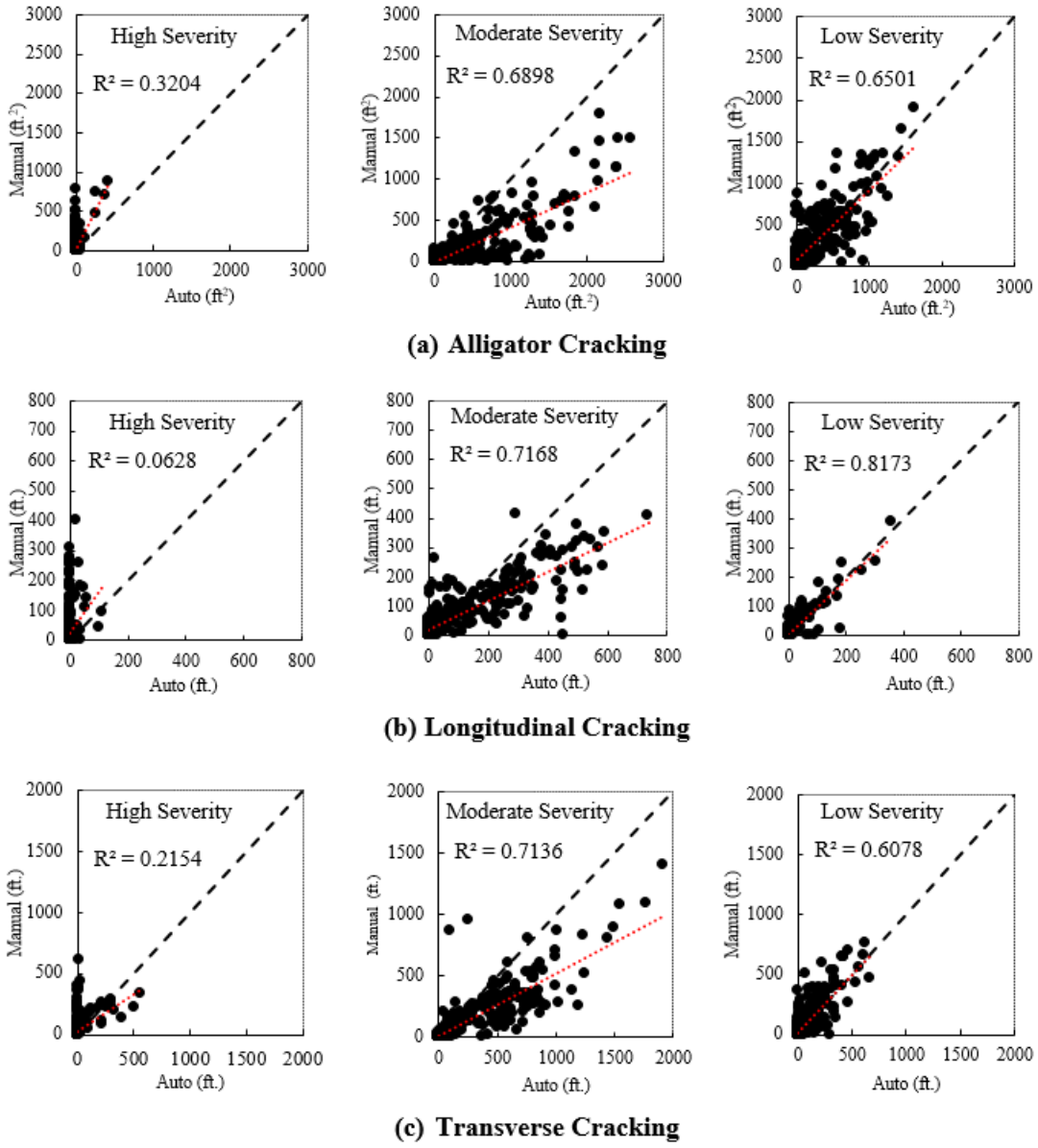

Figure 26 indicates the 3D automated system tends to over-estimate the moderate severity cracking for each crack type, but under-reports the high and low severity cracks for a 0.1 mile subsection. The results in Figure 27 are observed similar to those plots shown in Figure 25. It can be seen in Figure 27, when the cracking measurements of both 3D automated and the manual are relatively low, data points are close to the identity line. However, at each severity level for all crack types, with the increase of deterioration, the accuracy of the automated system reduces. On the other hand, the correlations between the 3D automated and manual measurements are found somewhat improved with the

higher R^2-values as compared to Figure 25. One reason may be partially because using less data points in Figure 27 could result in less scatter of the measurements. Another reason may be due to some accuracy and precision improvement when the 3D measurements are summarized in a longer subsection (e.g., the 0.1-mile subsection) as compared to those in the 50-ft. subsections.

Similarly, t-tests with non-normally distribution at a significant level of 95% and the Fligner-Kileen variance tests were performed on the 0.1-mile subsection to further verify the accuracy and precision of the 3D automated cracking measurements. The statistical results are presented in Table 17 and Table 18.

It can be observed in Table 17 that the mean errors between the automated and manual cracking measurements at all crack types at all severity levels are statistically different from zero based on 0.1-mile subsections. The t-test results generally confirmed the accuracy estimates in terms of the 3D mean measurement errors shown in Table 16. On the other hand, the p-values shown in Table 18 are slightly different from Table 13 at the project level analysis. The 3D automated measurements showed less varied (more precise) for low severity level of all crack types and high severity transverse cracking measurements. This finding agrees with the correlation analysis in Figure 27, indicating when reporting the cracking on a 0.1-mile subsection the 3D automated measurements tend to report slightly more precise cracking measurements as less data points are involved than using a 50-ft. subsection reporting.

Table 17. T-tests on measurement mean error results for 0.1-mile subsection

Crack Types	Severity Level	Actual Mean Error	Number of Subsections	Degree of Freedom	t-Statistic	*p*-Value	Significance
Alligator (ft^2)	High	-158.1	21	20	5.08	<0.0001	Yes
	Moderate	373.9	207	206	14.47	<0.0001	Yes
	Low	-41.15	252	251	2.58	0.0046	yes
	High	-77.78	37	36	4.99	<0.0001	Yes

Crack Types	Severity Level	Actual Mean Error	Number of Subsections	Degree of Freedom	t-Statistic	*p*-Value	Significance
Longitudinal (ft.)	Moderate	49.89	265	264	8.472	<0.0001	Yes
	Low	-6.66	164	163	3.55	0.0005	Yes
Transverse (ft.)	High	-43.33	52	51	2.04	0.046	yes
	Moderate	177.4	226	225	11.87	<0.0001	Yes
	Low	-18.68	264	263	3.12	0.002	Yes

Table 18. Results from Fligner-Kileen statistical analysis for 0.1-mile measurements

Crack Types	Severity Level	Number of Methods	Degree of Freedom	FK-Statistic	*p*-value	Significance
Alligator (ft^2)	High	2	1	6.5	0.01	Yes
	Moderate	2	1	52.6	4E-13	Yes
	Low	**2**	**1**	**0.6**	**0.44**	**No**
Longitudinal (ft.)	High	2	1	26.5	2.57E-07	Yes
	Moderate	2	1	40.9	1.60E-10	Yes
	Low	**2**	**1**	**3.5**	**0.06**	**No**
Transverse (ft.)	**High**	**2**	**1**	**1.55**	**0.26**	**No**
	Moderate	2	1	48.72	2.94E-12	Yes
	Low	**2**	**1**	**1.12**	**0.29**	**No**

Discussion

It should be noted that the repeatability and variation of the manual cracking rating due to multiple raters was not directly considered in this research due to time and budget constraints. However, it is believed that, due to the variation in pavement image quality and computer algorithm used in the 2017 LA-PMS database, the amounts of false positive and missed cracks identified by the manual rating in this study should be similar or close to each other even when a different experienced rater was involved. In addition, Figure 28 presents an example comparison between the manual and 3D measured medium alligator cracking amounts on one selected pavement project (841-02-1-010) of this study. As seen in Figure 28, when comparing the automated cracking measurements to +/- 50% of the manual results, the automated system was found to over-estimate the medium-severity cracks on 8 out 11 0.1-mile testing points. Similar observations were found on other cracking types considered, which indicates that the automated system used in 2017 LA-PMS database generally tends to over-estimate the medium-severity cracks of flexible pavements.

Figure 28. Comparison between automated cracking measurements to manual measurement results

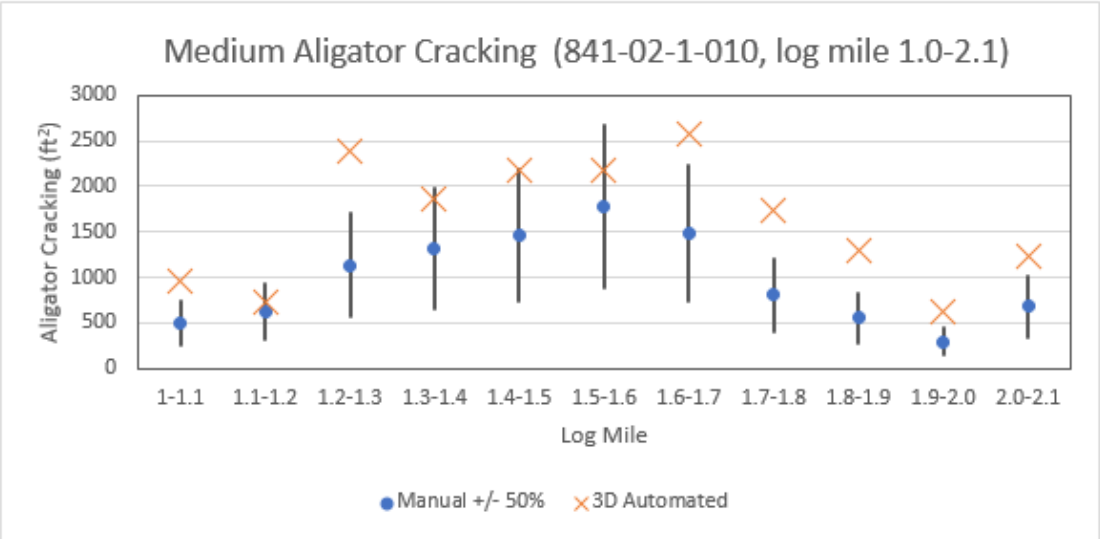

Furthermore, the pavement images used for the manual rating of this study are those of the Laser Crack Measurement System (LCMS) 3D collected pavement images as shown in the following Figure 29 (a), which are different from those used in the automatic software rating called the LCMSRange, figure (b). As can be seen in the figure, the

LCMSRange image tends to display significantly more cracks on a pavement surface than the LCMS3D image.

Figure 29. Comparison between LCMS3D and LCMSRange images

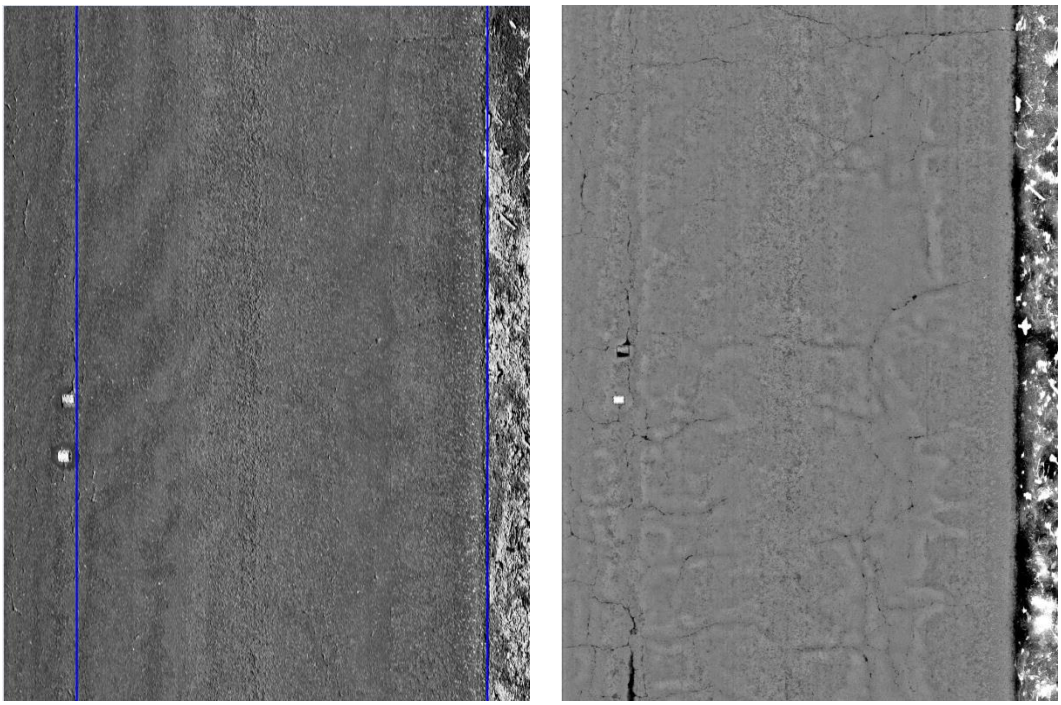

(a) LCMS3D (b) LCMSRange

A close look between the LCMS3D and LCMSRange images (Figure 30) indicates that some of the cracks in the LCMSRange image are not visible in the LCMS3D image. Since the comparison in this study was based on the manual LCMS3D image rating vs. the automated LCMSRange image rating, further research is still needed to clarify: (1) whether or not some of those unseen cracks in LCMS3D images are real pavement cracks through the field investigations; and (2) if LCMSRange images were found to over-predict pavement cracks, then determine how to improve the accuracy in the future DOTD's cracking data collection through adjusting the algorithm considered in the imaging software.

Figure 30. False crack in LCMSRange image

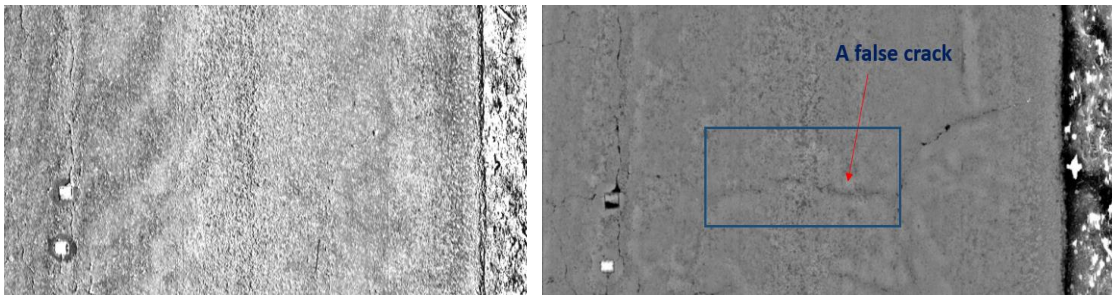

Comparison of Cracking Indices from the 3D and Manual Measurements

Previous analyses were based on the comparison of the accuracy and precision of the 3D automated cracking measurements as against the manual measurements. The results generally indicated that the automated cracking measurements were not statistically equal to the manual cracking data in various cracking types and severity levels. In this section, the cracking indices currently used in the treatment selection process by DOTD were determined using both the 3D automated and the manual cracking measurements collected on the selected 23 flexible pavements. Note that only an ALCR (the alligator cracking index) and an RNDM (the random cracking index determined by combining the longitudinal and transverse cracking measurements) are currently used by DOTD in a treatment selection.

The average calculated cracking index results are presented in Table 19. A pairwise t-test at a significant level of 95% was used in the comparison. Overall, the *p*-values indicate both cracking indices (ALCR and RNDM) determined from the automated cracking measurements are significantly different from those of manual cracking measurements. As shown in Table 19, the automated cracking measurements tend to under-predict the alligator cracking index but over-predict the random cracking index as compared to the manual cracking measurements.

Table 19. Comparison of automated cracking indices and p-values

Index Type	**Automated Mean**	**Manual Mean**	t-Statistics	t-Critical	*p*-Value	Significance
ALCR	84.82	88.00	-6.81	1.65	2.37E-11	**Significant**
RNDM	88.53	85.63	4.07	1.65	2.86E-05	**Significant**

Difference in indices from the 3D automated and manual cracking measurements may lead to a different pavement treatment selection. The calculated cracking indices for each selected 0.1-mile survey section of flexible pavement in this study were further used in a trial treatment selection exercise to determine if the automated and the manual cracking indices would provide the same or different treatment selections based on the current DOTD's treatment trigger values. The detailed results of the treatment selection exercise may be referred to as Appendix A. Note that only ALCR and RNDM indices were considered in the treatment selection exercise based on roadway function classes and control sections. Overall, nine out of twenty-three control sections (roughly 39 percent of control sections) yielded different treatment plans between the automated and manual cracking indices. Similar percentages of different treatment selections between the manual and the automated indices were found when the comparison were based on roadway function classes.

In summary, the aforementioned results generally indicate the automated cracking data collected using the vendor's 3D high-speed data collection system proved to be more accurate and less variated than the 2D automated system measurements for all flexible pavement crack types considered by DOTD's LA-PMS. On the other hand, the 3D automated cracking measurements were found statistically different from the manual measurements, as evidenced by the percentages of false positives and missed cracks as well as the overall low precisions. The different automated cracking measurements, specifically in terms of severity levels, would potentially yield a wrong treatment selection according to the DOTD's current treatment trigger values. In order to improve the accuracy of the 3D automated cracking data reported in 2017 LA-PMS database in the use of the DOTD's treatment selection and potentially implement for a project level pavement modeling and analysis, the following section will discuss an ANN-based cracking prediction model developed in this study.

Evaluation of Developed ANN Model

In this study, a 15-20-15-10-9 multilayered backpropagated feed-forward ANN model was developed based on the 0.1-mile subsections' cracking measurements collected by 3D automated and the manual survey methods (Figure 19). The developed ANN model aimed at adjusting the less accurate automated cracking measurements towards more accurate manual measurement results. In other words, the predicted cracking measurements from the ANN model should be closely matched with their corresponding manual results. In this study, there were 323 datapoints used to formulate the ANN model from 23 pavement sections in Louisiana. The data were divided into three subsets: 55% data for training, 30% data for validation, and the remaining 15% data were used for testing. Testing dataset were not used in model developing to avoid over prediction of the output. It should be noted that, input values for training and validation were chosen randomly.

As described in Methodology, a 15-20-15-10-9 multilayered backpropagated feed-forward ANN model was developed based on the 0.1-mile subsections' cracking measurements collected by 3D automated and the manual survey methods (Figure 19). The goal is to predict a set of manual cracking measurements from the 3D automated cracking measurements by considering the influences of the existing pavement surface treatment type, years of service, and other distress and environment conditions of each 0.1-mile subsection considered. With that in mind, the 15 input parameters used in the ANN model include the nine 3D automated cracking measurements and other automated system collected pavement surface distresses and conditions (e.g., Rutting, IRI, MPD), the pavement surface treatment type and years of service as well as the average temperature during data collection.

Figure 31 presents the ANN predicted cracking measurements as compared to the manual measurements using different datasets (i.e., 55% of training, 30% of verification, and 15% of testing). Table 20 presents a summary of the predicted R^2 values for the testing dataset, which was not used in the ANN model training development. In general, all the comparison plots showed in Figure 31 and high R^2 values in Table 20 seem to indicate that the predicted cracking measurements from the ANN model correlated well with the manual cracking measurements. On the other hand, a relatively low correlation was observed for the predicted longitudinal-high (R^2 of 0.67) and longitudinal-low cracking (R^2 0f 0.76), Table 20. This could be attributed partially to a high percentage of test sections in the training dataset having zero longitudinal low or high cracking.

Figure 31. Predicted vs. manual cracking measurements from ANN modeling; (a) training dataset (b) validation dataset (c) testing dataset and (d) all data

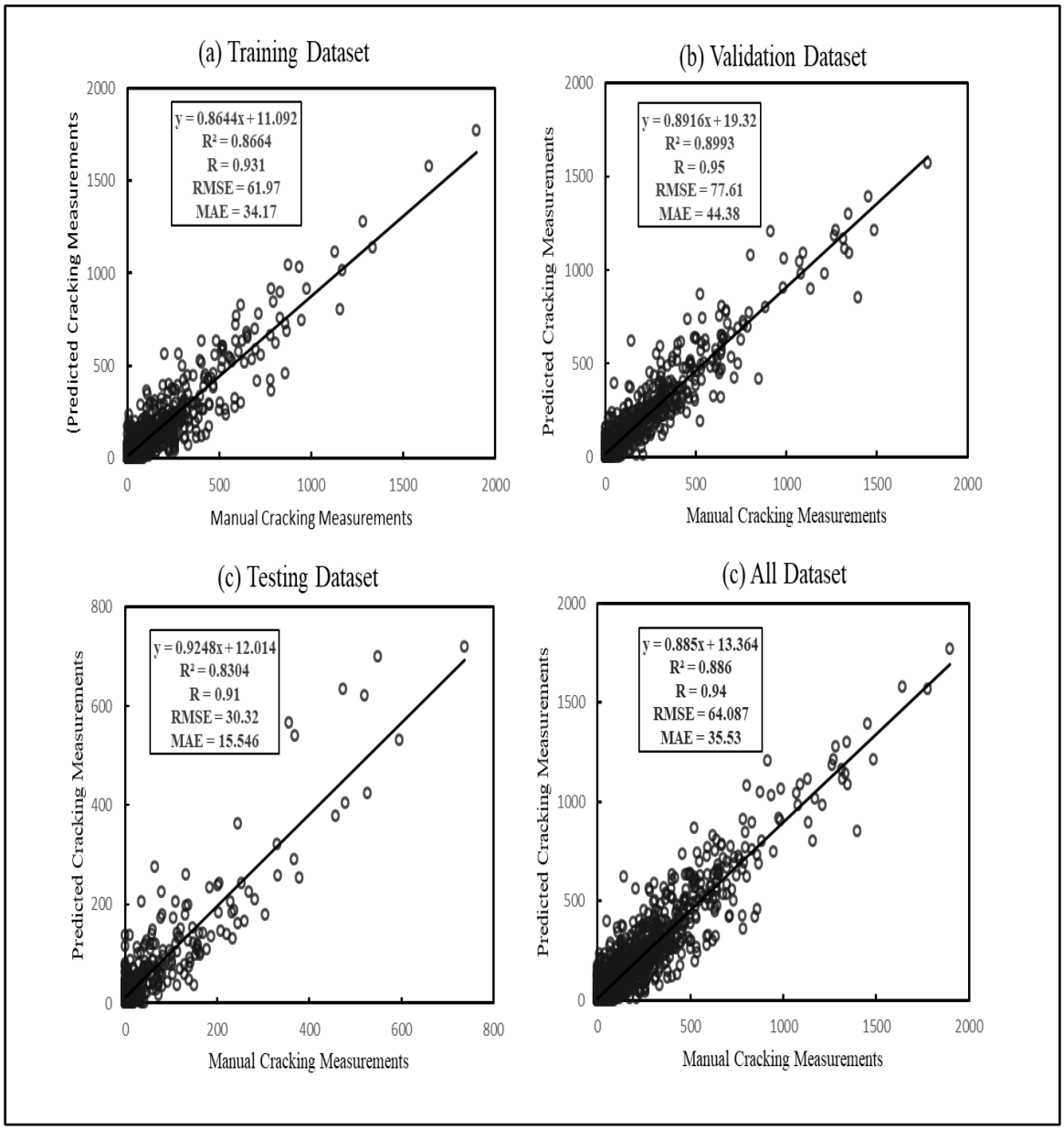

Table 20. Calculated validation parameters for each output from testing dataset

Crack Type	R - Value	R^2- Value	RMSE	MAE
Alligator-High (ft^2)	0.98	0.96	30.33	15.46

Crack Type	R - Value	R^2- Value	RMSE	MAE
Alligator-Moderate(ft^2)	0.93	0.86	51.31	46.78
Alligator Low(ft^2)	0.91	0.82	73.7	53.22
Longitudinal-High (ft.)	0.82	0.67	16.4	9.65
Longitudinal–Moderate (ft.)	0.92	0.84	23.04	14.06
Longitudinal-Low (ft.)	0.87	0.76	21.93	9.71
Transverse-High (ft.)	0.92	0.85	4.18	17.67
Transverse-Moderate (ft.)	0.91	0.84	46.53	34.93
Transverse-Low (ft.)	0.94	0.88	4.65	4.17

Figure 32 represents the Root Mean Square Error (RMSE) values from the 3D automated measurements and ANN-predicted measurements when compared with the manual measurements. RMSE from automated measurements were significantly greater than the ANN-predicted measurements for all crack types at each severity level.

Figure 32. RMSE from automated and ANN predicted measurements compared to the manual measurements

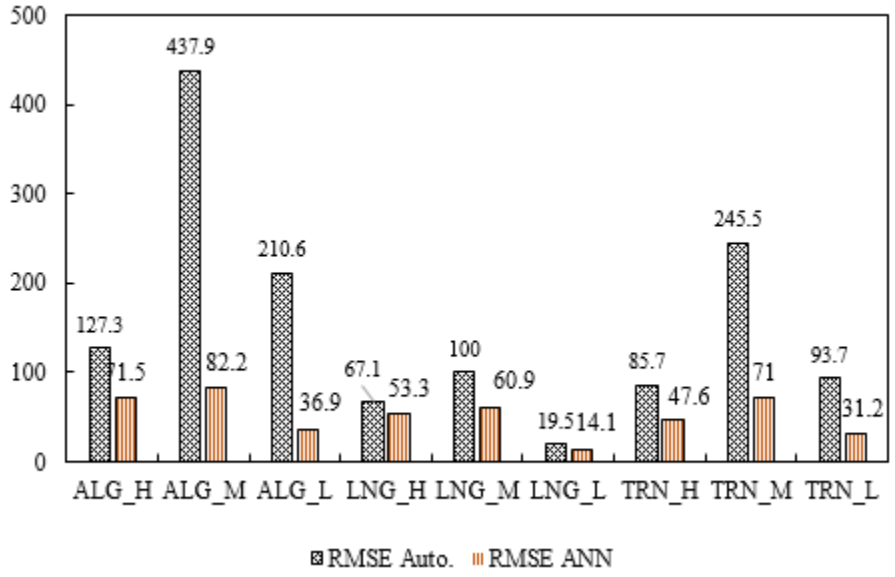

Figure 33 represents the Mean Absolute Error (MAE) values from the 3D automated measurements and ANN-predicted measurements when compared with the manual measurements. Except for high severity longitudinal cracking, MAE from automated measurements were significantly greater than the ANN-predicted measurements.

Figure 33. MAE from automated and ANN-predicted measurements compared to the manual measurements

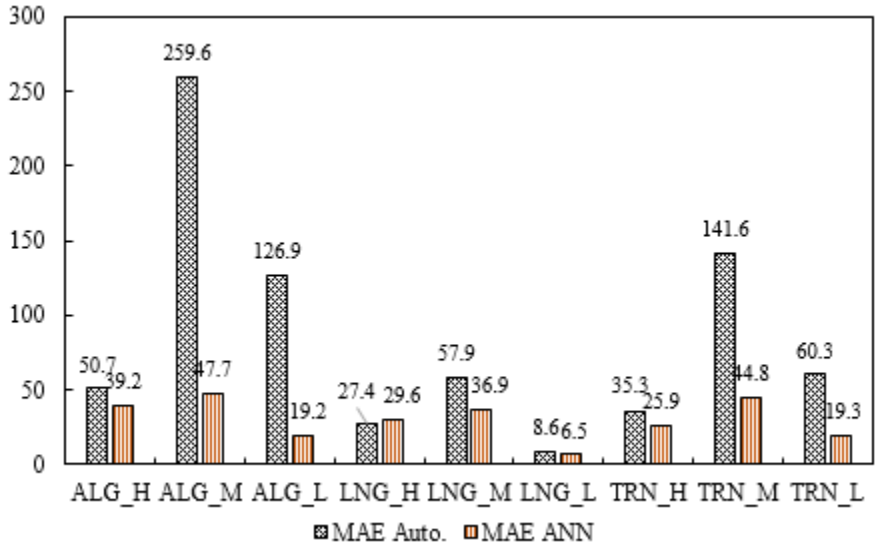

Table 21 generally showed that, the predicted cracking measurements from the ANN model are matched much closer to the manual measurement results than the automated measurements as indicated by the negative percent changes of both RMSE and MAE. This observation implies that, when using the developed ANN model, the accuracy of the automated cracking measurements in PMS may be significantly improved.

Table 21. Evaluation of ANN Model

Crack Type	Mean Measurement Errors		R		R^2		RMSE Change %	MAE Change %
	Auto	ANN	Auto	ANN	Auto	ANN		
ALG_H	-50.1	-2.9	0.56	0.91	0.31	0.83	-44	-23
ALG_M	250.4	-2.59	0.83	0.95	0.69	0.91	-81	-82
ALG_L	-34.9	-3.56	0.80	0.84	0.65	0.71	-82	-85
LNG_H	-26.0	3.92	0.25	0.93	0.06	0.87	-21	8
LNG_M	40.2	3.69	0.85	0.85	0.72	0.72	-39	-36
LNG_L	-3.2	-1.27	0.90	0.96	0.82	0.92	-28	-24
TRN_H	25.9	3.34	0.47	0.92	0.22	0.84	-44	-27
TRN_M	126.9	8.24	0.85	0.94	0.72	0.89	-71	-68
TRN_L	15.2	6.29	0.78	0.84	0.61	0.71	-67	-68

Verification of the ANN Prediction Model

To further validate the developed ANN cracking prediction model, the pavement cracking indices [i.e., ALCR and RNDM listed in equation (1) and (2)] were computed using both the ANN predicted and the manual cracking measurements. The average results are presented in Table 22. A pairwise t-test was performed to determine if the average ANN-predicted cracking indices are equal to those from the manual measurements. As showed in Table 22, all *p*-values are greater than 0.05 indicating the average ANN-predicted cracking indices are statistically equal to those from the manual measurements.

Table 22. Cracking indices from ANN-predicted vs. manual measurements and *p*-values

Index Type	ANN predicted Mean	Manual Mean	t-Statistics	t-Critical	*p*-Value	Significance
ALCR	**87.16**	88.00	-1.43	1.65	0.08	**Not Significant**
RNDM	**84.87**	85.63	-0.74	1.65	0.23	**Not Significant**

Monte Carlo analysis was conducted to find out the change in Pavement Condition Index (PCI) due to error from ALCR and RNDM indices calculation. Equations (18-22) were utilized to conduct the Monte Carlo simulation. Figure 34 represents the running average plots for Monte Carlo simulation.

Figure 34. Running average plot from Monte Carlo analysis

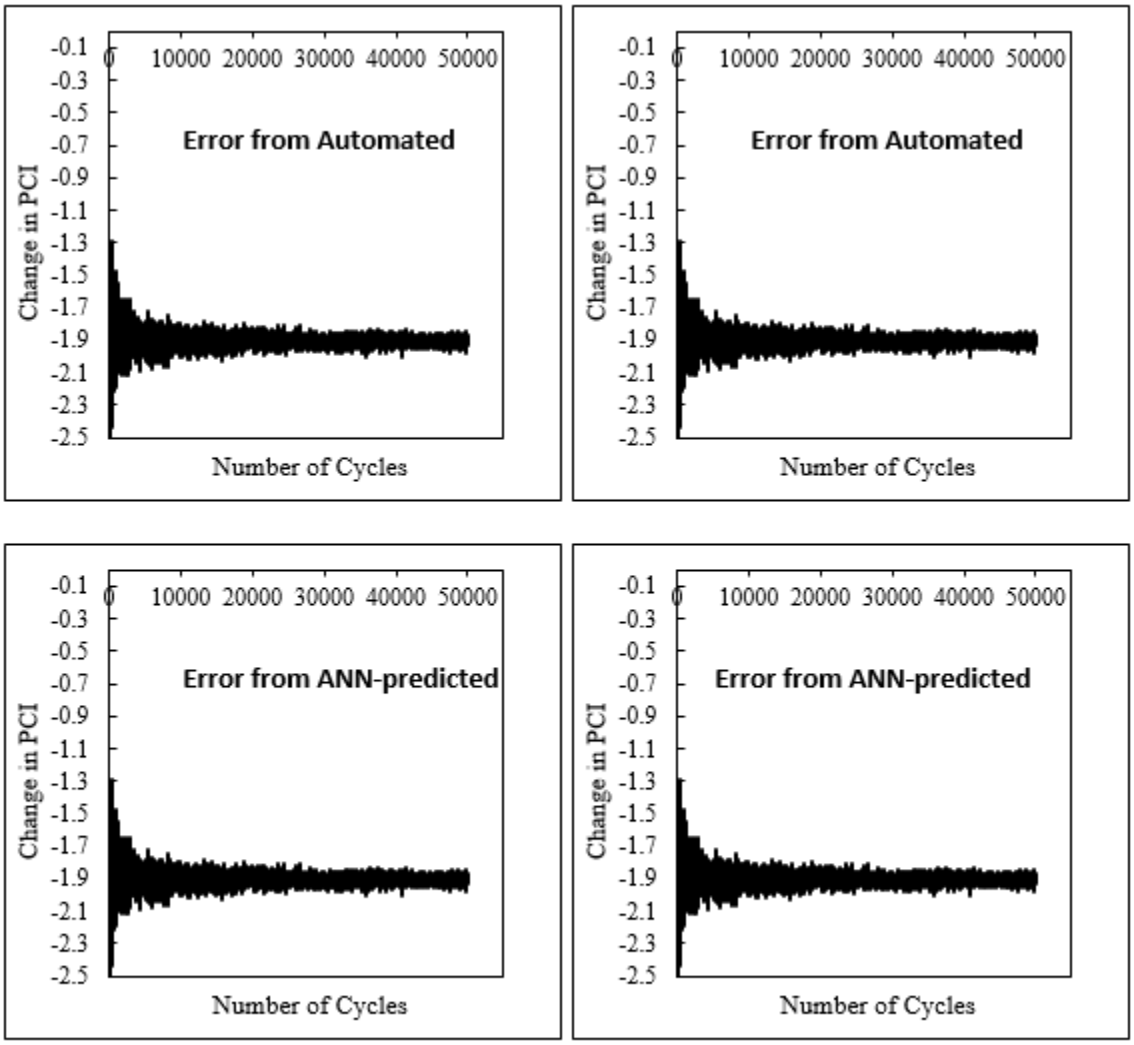

Table 23 evaluates the results from the Monte Carlo analysis. The mean column represents the average change in PCI due to ALCR and RNDM indices error. Table 23 indicates that the average change in PCI (or ΔPCI) was higher from the 3D automated measurements than the ANN-predicted measurements. It was assumed that 95% of the error values will fall within a two standard deviation. The "Max ΔPCI" column represents the maximum possible value of ΔPCI due to error in each index parameter and, thus, describes the sensitivity of PCI value due to the cracking measurements error from automated and ANN-predicted system. It can be observed that, for both the automated system and ANN-predicted measurements, the error in the RNDM index was more

sensitive to PCI than the error in the ALCR index. However, ANN-predicted ALCR and RNDM indices yield a lower maximum change in PCI, thus causing lower sensitivity to the final PCI values than automated ALCR and RNDM indices. Table 23 suggests that ANN-predicted cracking measurements were 41.67% and 26.5% less sensitive than automated cracking measurements for ALCR and RNDM respectively.

Table 23. Results from Monte Carlo simulation

Index	Automated			ANN-Predicted			% change in Max PCI
	Mean ΔPCI	Standard Deviation of ΔPCI	Max ΔPCI	Mean ΔPCI	Standard Deviation of ΔPCI	Max ΔPCI	
ALCR	-1.9	4.8	9.6	-0.38	2.8	5.6	41.67%
RNDM	1.1	4.9	9.8	-0.37	3.6	7.2	26.5%

Summary of the Developed MATLAB Application for $DHDV_{LTRC}$

A MATLAB computer application was developed in this research for identifying and measuring various asphalt pavement cracking distresses from 2-D pavement images collected using the $DHDV_{LTRC}$. Note that the current version of the computer software application is considered as a prototype and its accuracy in the crack type identification and detail cracking measurements still warrant further verification and improvement. Figure 35 represents the framework used in the development using the MATLAB.

Figure 35. Framework for developing automated crack survey application

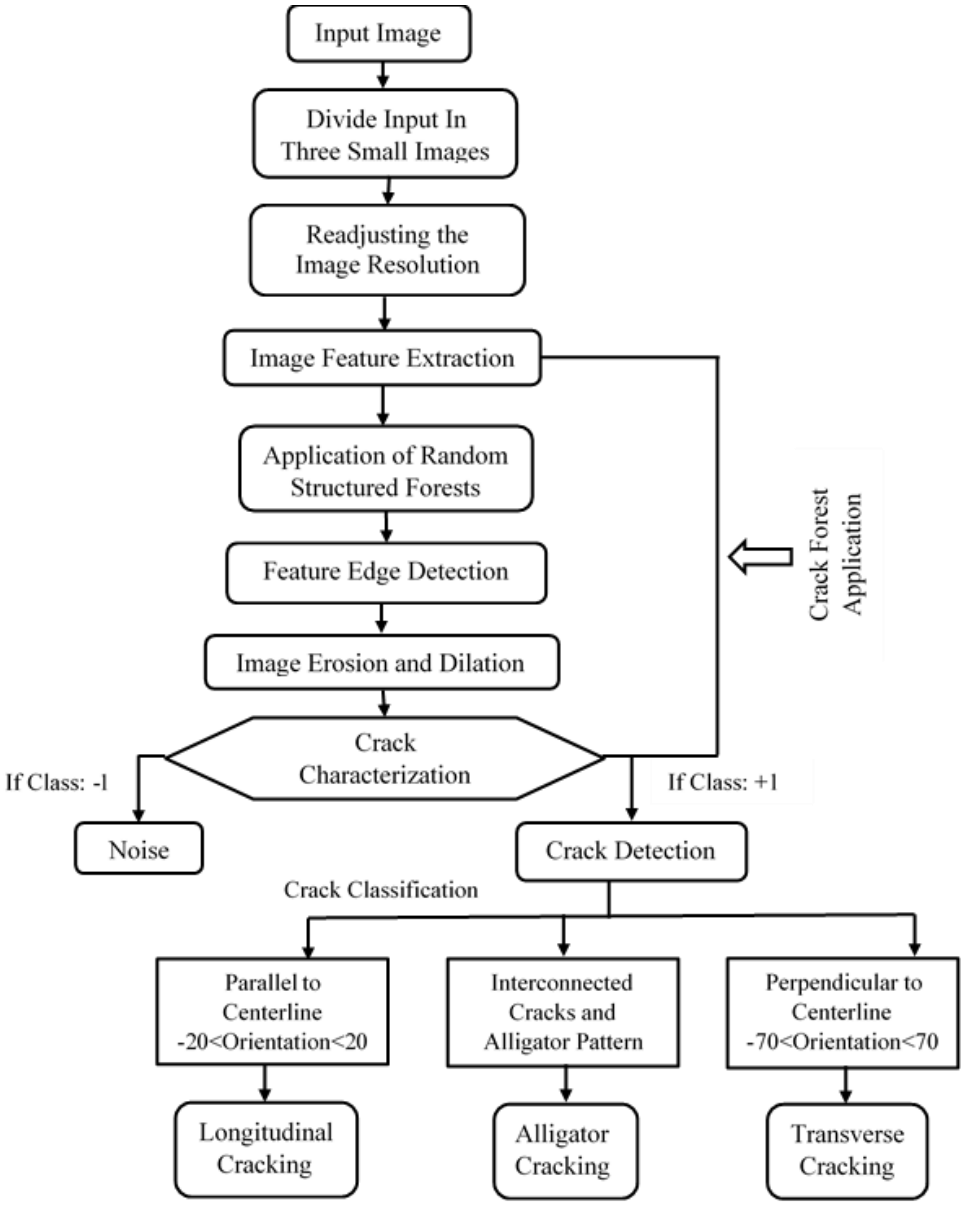

Readjusting Input Image

Input images were collected from LTRCs' Digital Highway Data Collection Vehicle. As two images from the LTRC vehicle merge together to form a complete pavement section, it was necessary to readjust the image size according to the 'CrackForest' algorithm. According to Shi et al., each image was divided into three 480 × 320 pixel-sized images. Each pixel was 0.0155 ft. in width and 0.0155 ft. in length. Thus, two original 7.44 ft. × 14.88 ft. images were divided and readjusted into six 7.44 ft. × 4.96 ft. images to form a

complete pavement section for evaluation. Readjusted images were saved in ‘Output 1’ folder and kept in the same location as the ‘CrackForest’ framework.

Applying ‘CrackForest’ Algorithm

Crack detection framework was applied to the readjusted images in ‘Output 1.’ Crack detection algorithm first applied the feature extractor to identify the crack regions. Crack regions generally have darker pixels than the non-cracked regions. Then previously developed ‘structured forests algorithm’ was implemented to detect the crack features (edges, shape, etc.). Binarization (image erosion and image dilation) technique was applied to ensure the continuity of the cracked regions. Manually drawn crack patterns on binary images were used to train the ‘structured forests algorithm.’ ‘CrackForest’ application tackled the crack detection problem as a classification one where cracked regions are classified as +1 and non-cracked regions are classified as -1 in the training dataset. Upon completion of the model training, noise from the binary image were deleted and final crack detected images were saved in ‘Output 2’ folder for crack classification and quantification and stored in the same location as the ‘CrackForest’ application. Figure 36 illustrates the procedures that were followed for crack detection from each image.

Figure 36. (a) Original image (b) feature extraction (c) edge detection (d) image erosion (e) image dilation and (f) crack detection

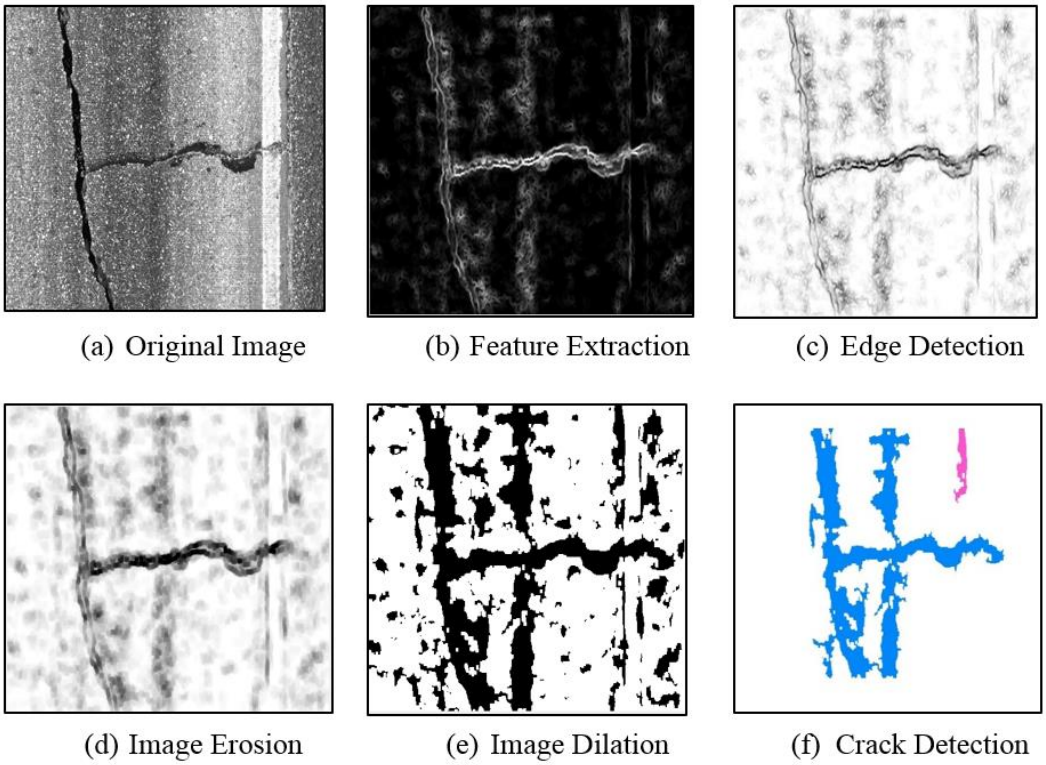

Crack Classification and Quantification Algorithm

'Crack Detected' images from 'Output 2' folder were used for crack classification and quantification. An ellipse was formed surrounding each detected cracks which covers the least area for each crack, Figure 37. Each ellipse has a horizontal (semi-major axis: b) and vertical (semi-minor axis: a) axis.

Figure 37. Ellipse surrounding each crack

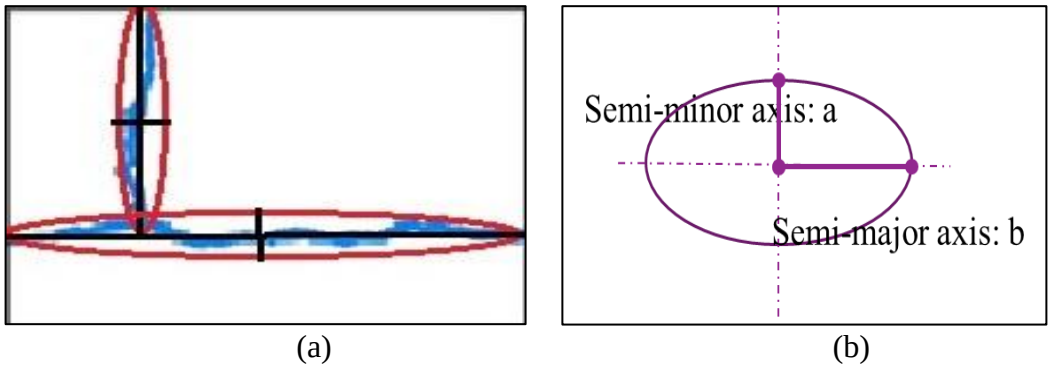

‘REGIONPROPS’ function in ‘MATLAB’ was utilized to estimate the convex area and parameter (length) for each axis. As image dimensions are defined by pixel; convex pixel area and pixel parameter was converted into ft^2 and ft. respectively using previously estimated pixel dimension (0.0155 ft. in width and 0.0155 ft. in length). Moreover, axis percentage was determined by dividing semi-minor axis: a from Semi-major axis: b.

Threshold Value: Threshold value is applied to differentiate alligator cracking from longitudinal or transverse cracking. $If\ Axispercentage = \frac{a}{b} \geq 0.3$, the crack was classified as alligator cracking. Otherwise, it was classified as longitudinal or transverse cracking.

Horizontal and vertical axis for longitudinal or transverse classified cracks were checked for the orientation. Vertical axis was defined as the centerline as it is parallel to the traffic direction and the orientation for each crack was determined from the centerline. If $-70 < \text{crack orientation from centerline} < 70$, it was classified as transverse cracks. Otherwise, it was classified as Longitudinal Crack.

Alligator cracking was reported in area (ft^2) and both longitudinal and transverse cracking were reported in ft. Crack classification and quantification algorithm was performed on each readjusted image. However, summary reports were produced for each readjusted image and also by adding cracking measurements for six images. Crack classification images and summary reports were saved in ‘Output 3’ folder and kept in the same location as the ‘CrackForest’ framework.

Figure 38 illustrates the final results from crack classification algorithm. Crack detection algorithm used a classifier to remove noise from the original image. However, crack detection application was unable to remove the shadows from the tire mark and shoulder mark. Figure 38 (a) shows the presence of longitudinal and transverse cracking. From Figure 38(b), it can be seen that, crack detection application identified the tire mark as a crack and connected it with the transverse crack to form a pattern, which prompted the classification algorithm to classify the pattern as an alligator crack and neglect both longitudinal and transverse cracks in Figure 38 (c). On the other hand, detection algorithm was unable to remove the whole shoulder mark as noise thus prompting the classification algorithm to classify it as a longitudinal crack.

Figure 38. (a) Original image (b) crack detected image and (c) crack classification

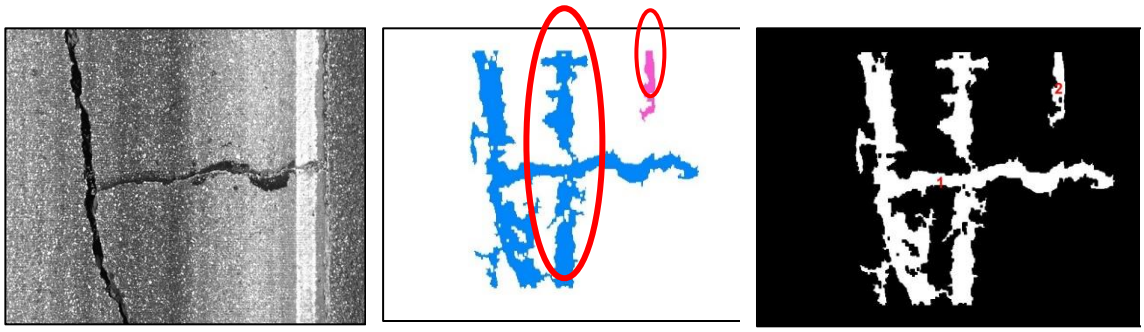

(a) (b) (c)

Table 24 represents the summary result from the automated crack survey application for one readjusted image. Alligator cracking is measured in ft^2 and both longitudinal and transverse cracking are measured in ft.

Table 24. Summary results from the LTRCs' automated cracking survey application

Section ID	Length	Alligator (ft^2)	Longitudinal (ft.)	Transverse (ft.)
LA 005_1	14.88	33.68	27.81	0
LA 005_2	14.88	15.98	29.87	6.87
LA 005_3	14.88	57.97	55.14	0
LA 005_4	14.88	47.87	37.82	0
LA 005_5	14.88	19.87	24.65	0

The built-in crack detection algorithm was verified to exclude all the pavement marks (oil stains, shadows, tire marks, etc.) other than pavement cracking. However, images which were used for the validation of the crack detection algorithm were collected using iPhone 5 camera with very low resolution. In this automated application, pavement images were collected using high resolution cameras from a vertical angle which capture dark tire marks and other stain patterns. Thus, crack detection algorithm was unable to differentiate dark tire marks and/or shadows from darker crack region pixels. More research is needed to improve the accuracy of the cracking identification algorithm used.

Conclusions

This research study was conducted to evaluate and assess the quality of the automated cracking measurements for flexible pavements in Louisiana. From previous studies, it was evident that the automated distress survey showed a good degree of reliability for the rut depth and IRI measurements. However, the automated cracking data are still prone to errors and irregularity. DOTD started in 2017 by collecting the LA-PMS pavement distress data using a vendor's 3D automated data collection system for LA-PMS. In this study, a comprehensive manual cracking survey was conducted on twenty-three flexible pavement sections (totally 28.6 miles long) and nine 0.5-mile calibration sites, using Vendor's high-resolution pavement images collected during DOTD's 2017 pavement condition data collection cycle. In addition, a MATLAB-based imaging analysis computer program was developed to generate an automated cracking report from high-resolution 2D pavement images collected by LTRC's DHDV automatic system.

For the evaluation of flexible pavement automated cracking measurements reported in LA-PMS's 2017 pavement condition database, the following observations and conclusions may be drawn from this study:

- From 2D, 3D, and manual crack measurements comparison for calibration sites: 2D system over-predicted total alligator cracking by 2.3% and under-predicted total longitudinal and transverse cracking by 30.2% and 7.8% respectively. On the other hand, the 3D system under-predicted total alligator cracking and longitudinal cracking by 1.4% and 7.4%, respectively, and over-predicted transverse cracking by 11.3% when compared with the manual measurements. Comparison at each severity level indicated that the 2D system significantly over-estimated low severity cracks (12% and 11% for alligator and transverse cracking respectively) and under-estimated moderate severity cracks (10% and 9% for alligator and transverse cracking respectively) compared to the manual measurements. Comparison between the 3D system and the manual system showed that 3D system measurement at each severity level for all crack types was close to the manual measurements with 5% being the highest difference where 3D system overestimated moderate severity longitudinal cracking. It can be concluded that 3D system's performance was better and closer to the reference values than 2D system's measurements.
- Crack detection efficiency of the automated method was determined based on the manual and automated cracking measurements from 2,844 50-ft. subsections

considered in this study. In general, false positive errors produced by the automated system (8.5%, 9.8%, and 8.8% respectively for alligator, longitudinal, and transverse cracking) were greater than the missed crack errors (5.0%, 7.9%, and 1.4% respectively). It can be observed that the highest percentages of false positives and missed cracks are the longitudinal cracking. This is as expected, since computer software may miss-identify a fallen object or sealed crack as longitudinal cracking or longitudinal cracking may be miss-counted due to the strict algorithm followed by the software. Moreover, the precision errors produced by the automated system on 0.1-mile subsections for all crack types were all greater than 18.5% (Table 16), which indicates that automated system could falsely detect and report cracking distresses on some non-cracked sections.

- In general, the automated cracking measurements for 50-ft. subsections and 0.1-mile subsections followed a similar estimation trend. The automated measurements over-estimated the amounts of cracks at moderate severity level and under-reported the amounts of cracks at high and low severity levels. Scatter plots for manual and automated cracking measurements at 50-ft. subsection suggested that the automated results poorly correlated with manual measurements with R^2 values less than 0.5 for all crack types and severity levels. On the other hand, the automated measurements on 0.1-mile subsections correlated well with the manual measurements at moderate and low severity levels for all crack types with R^2 values greater than 0.6. However, high average measurement errors and standard deviations indicated that both systematic and random errors could be produced by the automated system. To qualitatively estimate the accuracy and precision of the automated system, a t-test on measurement error and Fligner-Kileen statistical tests were performed at a significance level of 0.05. Results showed that, at the project-level (on 50-ft. subsections), the automated system could produce significantly accurate results for high severity transverse cracking and significantly precise results for low severity alligator cracking. At the network level (on 0.1-mile subsections), the automated system produced significantly accurate estimation at low severity alligator cracking and high severity transverse cracking. The automated system also produced significantly precise cracking measurements at low severity level for all crack types.
- The *p*-values from a pairwise t-test suggested that both ALCR and RNDM mean cracking indices determined from the automated cracking measurements were significantly different from those of manual cracking measurements, indicating that the automated cracking measurements under-predicted the alligator cracking index, but over-predicted random cracking index. It was observed that automated

measurements could potentially lead to different treatment selections according to the current DOTD cracking indices trigger values.

- A feed-forward ANN prediction model was developed to shift the 0.1-mile automated cracking measurements of flexible pavements in 2017 LA-PMS database towards the ground-truth manual measurements. Several pavement and environmental factors potentially or possibly associated with the automated cracking image processing and identification were considered in the ANN model, which include other existing pavement distresses (rutting, IRI, and MPD), pavement age, treatment type, and air temperature. Results indicate that the ANN-predicted cracking indices (ALCR and RNDM) were found statistically similar to the corresponding manual cracking measurements on the flexible pavement sections considered in this study.

In addition, for LTRC's DHDV automatic system, a MATLAB-based imaging analysis computer program was developed to generate an automated cracking report from high-resolution 2D pavement images collected by LTRC's DHDV automatic system. The development of the imaging analysis computer application are summarized below:

- For crack detection, an algorithm called "Structured Random Forests" was implemented in MATLAB. Pavement images collected from the DHDV were re-adjusted according to the training images from the Structured Random Forests algorithm. MATLABs' image processing toolbox was utilized to transform the colored images in binary images. Crack Detection framework was then applied on the binary images to filter the noises and detect pavement cracks.
- To develop the crack classification algorithm, the methodology was kept simple. Interconnected cracks were classified as alligator cracking, cracks which were predominately parallel to the traffic direction were classified as longitudinal cracking and cracks which were predominately perpendicular to the pavement centerline were classified as transverse cracking. Alligator cracking measurements were reported in ft^2 and both longitudinal and transverse cracking were reported in ft.
- It was observed that, the developed cracking survey application can produce summary results for a continuous 0.1-mile pavement section in seven minutes. However, the developed application sometimes failed to remove deep tire marks and shoulder markings. Observations showed that, detected tire markings connect with possible transverse cracks and form a pattern, which prompted the classification algorithm to over-estimate alligator cracking and under-estimate transverse cracking. Therefore, further algorithm improvements are still warranted in the crack detection and image noise removal subroutines of the developed imaging program in order to predict more accurate cracking measurements from the LTRC's DHDV automated system.

Recommendations

Based on the findings of this project, the following recommendations were made:

It is recommended the PMS office utilize the newly developed ANN cracking prediction application for its 2017 LA-PMS's flexible pavement cracking database in the project treatment selection process, especially when the cracking indices become the control parameters in a treatment selection.

Due to the difference between the LCMS3D and LCMSRange images, the vendor shall check the cracking accuracy when using LCMSRange images in the future pavement condition data collection for DOTD.

Pavement researchers can use the developed ANN cracking model to adjust the 3D automated asphalt pavement cracking data retrieved from the 2017 LA-PMS database and the adjusted crack values may be treated as pseudo project-level measurements used in the pavement performance evaluation and/or performance model calibration.

The developed MATLAB application for DHDV can be used to generate an automated cracking report for the 2D camera collected pavement images from the LTRC digital data collection vehicle. However, the accuracy of the automated cracking report still have room for an improvement.

Acronyms, Abbreviations, and Symbols

Term	Description
2D	Two Dimension
3D	Three Dimension
AASHTO	American Association of State Highway and Transportation Officials
ADA	Automated Distress Analyzer
ALCR	Alligator Cracking Index
ANN	Artificial Neural Network
ARAN	Automatic Road Analyzer
ASTM	American Society of Testing Materials
CDF	Cumulative Density Function
DHDV	Digital Highway Data Vehicle
DN	Do Nothing Treatment
DOT	Department of Transportation
DOTD	Louisiana Department of Transportation and Development
FHWA	Federal Highway Administration
FK	Fligner-Kileen Variance Test
FWD	Falling Weight Deflectometer
IRI	International Roughness Index
LA-PMS	Louisiana Pavement Management System
LCMS	Laser Crack Measurement System
LTRC	Louisiana Transportation Research Center
LTPP	Long-Term Pavement Performance
LCMS	Laser Crack Measurement Sensors
LRIS	Laser Road Imaging System
MAE	Mean Absolute Error

Term	Description
MEPDG	Mechanic-Empirical Pavement Design Guide
MO	Medium Overlay
MPD	Mean Profile Depth
MS	Micro-Surfacing Treatment
NCHRP	National Cooperative Highway Research Program
NPS	National Park Service
PCI	Pavement Condition Index
PDF	Probability Density Function
PMS	Pavement Management System
PTCH	Patching Index
R2	Coefficient of Determination
RMSE	Root Mean Square Error
RNDM	Random Cracking Index
RUFF	Roughness Index
RUT	Rutting Index
SO	Structural Overlay
TO	Thin Overlay
UTO	Ultra-Thin Overlay

References

[1] Khattak, M. J., Baladi, G. Y., & Sun, X. (2009). Development of index-based pavement performance models for pavement management system (PMS) of DOTD: tech summary (No. FHWA/LA. 08/460). Louisiana Transportation Research Center.

[2] McGhee, K. H. (2004). Automated pavement distress collection techniques (Vol. 334). Transportation Research Board.

[3] Attoh-Okine, N., & Adarkwa, O. (2013). Pavement condition surveys–overview of current practices. Delaware Center for Transportation, University of Delaware: Newark, DE, USA.

[4] Qiu, X., & Wang, F. (2014). Use of automated survey for surface cracking distress condition in a pavement management system. In Pavement materials, structures, and performance (pp. 351-363).

[5] Wu, Z., & Yang, X. (2012). Evaluation of current Louisiana flexible pavement structures using PMS data and new mechanistic-empirical pavement design guide (No. FHWA/LA.11/482). Louisiana Transportation Research Center.

[6] Timm, D. H., & McQueen, J. M. (2004). A study of manual vs. automated pavement condition surveys. Alabama, EE. UU: Auburn University.

[7] Vitillo, N., Gucunski, N., Rascoe, C., & Zaghloul, S. (2009). Evaluation of the Automated Distress Survey Equipment (No. FHWA NJ-2009-007).

[8] Serigos, P. A., Prozzi, J. A., de Fortier Smit, A., & Murphy, M. R. (2016). Evaluation of 3D Automated Systems for the Measurement of Pavement Surface Cracking. Journal of Transportation Engineering, 142(6), 05016003.

[9] Wang, K. C., Li, J. Q., & Yang, G. (2020). Standard Definitions for Common Types of Pavement Cracking. NCHRP Web-Only Document, (NCHRP Project 01-57A).

[10] Federal Highway Administration (FHWA). 2014. Distress Identification Manual for the Long-Term Pavement Performance Program (Fifth Revised Edition). FHWA-HRT-13-092, Washington, D.C.

[11] AASHTO R 85-18 “Standard Practice for Quantifying Cracks in Asphalt Pavement Surfaces from Collected Pavement Images Utilizing Automated Methods”. AASHTO, 2018

[12] AASHTO R 55-10 “Standard Practice for Quantifying Cracks in Asphalt Pavement Surfaces”. AASHTO, 2013.

[13] Louisiana protocol (2014) "Louisiana DOTD Distress Identification Protocols For Asphalt & Composite Pavements"

[14] AASHTO, "Mechanistic-Empirical Pavement Design Guide, Interim Edition: A Manual of Practice," AASHTO, 2008.

[15] Kristiansen, J. (1998). Implementation of Pavement Management Systems in 8 Republics of the Former Soviet Union. In 4th International Conference on Managing Pavements. South Africa (pp. 1137-1153).

[16] Haas, R., Hudson, W. R., & Zaniewski, J. P. (1994). Modern pavement management.

[17] Morian, D., Stoffels, S., & Frith, D. J. (2002). Quality management of pavement performance data. In Pavement Evaluation Conference, 2002, Roanoke, Virginia, USA.

[18] Flintsch, G. W., & McGhee, K. K. (2009). Quality management of pavement condition data collection (Vol. 401). Transportation Research Board.

[19] Pierce, L. M., & Zimmerman, K. A. (2015, June). Quality Management for Pavement Condition Data Collection. In 9th International Conference on Managing Pavement Assets.

[20] Kargah-Ostadi, N., Nazef, A., Daleiden, J., & Zhou, Y. (2017). Evaluation Framework for Automated Pavement Distress Identification and Quantification Applications. Transportation Research Record, 2639(1), 46-54.

[21] Goodman, S. N. (2001). Assessing variability of surface distress surveys in canadian long-term pavement performance program. Transportation research record, 1764(1), 112-118.

[22] Rada, G. R., Bhandari, R. K., Elkins, G. E., & Bellinger, W. Y. (1997). Assessment of long-term pavement performance program manual distress data variability: bias and precision. Transportation research record, 1592(1), 151-168.

[23] Haas, C., & Hendrickson, C. (1991). Integration of diverse technologies for pavement sensing. Transportation Research Record: Journal of The Transportation Research Board, (1311), 92-102.

[24] Chua, K. M., & Xu, L. (1994). Simple procedure for identifying pavement distresses from video images. Journal of transportation engineering, 120(3), 412-431.

[25] Wang, K. C., & Elliott, R. P. (1999). Investigation of image archiving for pavement surface distress survey.

[26] Chambon, S., & Moliard, J. M. (2011). Automatic Road Pavement Assessment with Image Processing: Review and Comparison. International Journal of Geophysics.

[27] Zakeri, H., Nejad, F. M., & Fahimifar, A. (2017). Image based techniques for crack detection, classification and quantification in asphalt pavement: a review. Archives of Computational Methods in Engineering, 24(4), 935-977.

[28] Huang, Y., & Tsai, Y. (2011). Dynamic programming and connected component analysis for an enhanced pavement distress segmentation algorithm. Transportation research record, 2225(1), 89-98

[29] Zou, Q., Cao, Y., Li, Q., Mao, Q., & Wang, S. (2012). CrackTree: Automatic crack detection from pavement images. Pattern Recognition Letters, 33(3), 227-238.

[30] Oliverira, H., & Correia, P. L. (2012). CrackTree: Automatic crack detection and characterization. *IEEE* Transactions on Intelligent Transportation Systems, 14(1), 155-168.

[31] Hoang, N. D., & Nguyen, Q. L. (2018). Automatic recognition of asphalt pavement cracks based on image processing and machine learning approaches: a comparative study on classifier performance. Mathematical Problems in Engineering, 2018.

[32] Wang, K. C. (2011). Automated survey of pavement distress based on 2D and 3D laser images (No. MBTC DOT 3023). Mack-Blackwell National Rural Transportation Study Center (US).

[33] Jiang, J., Liu, H., Ye, H., & Feng, F. (2015). Crack enhancement algorithm based on improved EM. JOURNAL OF INFORMATION &COMPUTATIONAL SCIENCE, 12(3), 1037-1043.

[34] Zhang, A., Wang, K. C., & Ai, C. (2017). 3D shadow modeling for detection of descended patterns on 3D pavement surface. Journal of Computing in Civil Engineering, 31(4), 04017019.

[35] Li, B., Wang, K. C., Zhang, A., Fei, Y., & Sollazzo, G. (2019). Automatic segmentation and enhancement of pavement cracks based on 3D pavement images. Journal of Advanced Transportation, 2019.

[36] Laurent J., Hebert J., Lefebvre, D. & Savard Y. (2012) Using 3D Laser Profiling Sensors for the Automated Measurement of Road Surface Conditions. 7th RILEM International Conference on Cracking in Pavements.

[37] Fugro, 2017. https://www.fugro.com/our-services/asset-integrity/roadware

[38] McQueen, J. M., & Timm, D. H. (2005). Statistical analysis of automated versus manual pavement condition surveys. Transportation research record, 1940(1), 54-62.

[39] McNeil, S., & Humplick, F. (1991). Evaluation of errors in automated pavement-distress data acquisition. Journal of Transportation Engineering, 117(2), 224-241.

[40] Offrell, P., Sjögren, L., & Magnusson, R. (2005). Repeatability in crack data collection on flexible pavements: Comparison between surveys using video cameras, laser cameras, and a simplified manual survey. Journal of transportation engineering, 131(7), 552-562.

[41] Wix, R., & Leschinski, R. (2012, September). Cracking: A tale of four systems. In ARRB Conference, 25th, 2012, Perth, Western Australia, Australia

[42] Tao, J., Luo, X., Qiu, X., & Wang, F. (2020). Data quality assessment of automated pavement cracking measurements in Mississippi. International Journal of Pavement Research and Technology, 1-12.

[43] Abedini, R., Esfandyari, M., Nezhadmoghadam, A.and Rahmanian, B. (2012). The Prediction of Undersaturated Crude Oil Viscosity: An Artificial Neural Network and Fuzzy Model Approch. Petroleum Science and Technology, 30(19).

[44] Sinha, S. K., & Wang, M. C. (2008). Artificial neural network prediction models for soil compaction and permeability. Geotechnical and Geological Engineering, 26(1), 47-64.

[45] Khademi, F., Akbari, M., Jamal, S. M., & Nikoo, M. (2017). Multiple linear regression, artificial neural network, and fuzzy logic prediction of 28 days compressive strength of concrete. Frontiers of Structural and Civil Engineering, 11(1), 90-99.

[46] Yang, G., Wang. K.C., Li, J. Q., Fei, Y., Liu, Y., Mahboub, K.C., & Zhang, A.A. (2020). Automatic Pavement Type Recognition for image-based pavement condition survey using convolutional neural network. Journal of Computing in Civil Engineering, 35(1), 0402060.

[47] Ceylan, H., Bayrak, M. B., and Gopalakrishnan, P. Neural Networks Applications in Pavement Engineering: A Recent Survey, International Journal of Pavement Research and Technology, 7(6), p.434, 2014.

[48] Plati, C., Georgiou, P. and Papavasiliou, V. Simulating Pavement Structural Condition Using Artificial Neural Networks, Structure and Infrastructure Engineering, pp. 1–10, 2015.

[49] Kim, S., Ceylan, H., Ma, D., and Gopalakrishnan, K. "Local Calibration Studies on DARWin-ME / Mechanistic-Empirical Pavement Design Guide Jointed Plain Concrete Pavement Performance Prediction

[50] Hosseini, S. M. K., Zarei-Hanzaki, A., Panah, M. Y., & Yue, S. (2004). ANN model for prediction of the effects of composition and process parameters on tensile strength and percent elongation of Si–Mn TRIP steels. Materials Science and Engineering: A, 374(1-2), 122-128.

[51] Li, J., Cheng, J. H., Shi, J. Y., & Huang, F. (2012). Brief introduction of back propagation (BP) neural network algorithm and its improvement. In Advances in computer science and information engineering (pp. 553-558). Springer, Berlin, Heidelberg.

[52] Torrecilla, J. S., Aragon J. M., and Palancar, M. C. Optimization of an Artificial Neural Network by Selecting the Training Function. Application to Olive Oil Mills Waste. Industrial & Engineering Chemistry Research, 47, 7072-7080, 2008.

[53] Dorofki, M., Elshafie, A. H., Jaafar, O., Karim, O. A., & Mastura, S. (2012). Comparison of artificial neural network transfer functions abilities to simulate extreme runoff data. International Proceedings of Chemical, Biological and Environmental Engineering, 33, 39-44.

[54] Lahiri, S. K., & Ghanta, K. C. (2009). Artificial neural network model with the parameter tuning assisted by a differential evolution technique: The study of the holdup of the slurry flow in a pipeline. Chemical Industry and Chemical Engineering Quarterly/CICEQ, 15(2), 103-117.

[55] Sollazzo, G., Fwa, T. F., & Bosurgi, G. (2017). An ANN model to correlate roughness and structural performance in asphalt pavements. Construction and Building Materials, 134, 684-693.

[56] Vyas, V., Singh, A. P., & Srivastava, A. (2020). Prediction of asphalt pavement condition using FWD deflection basin parameters and artificial neural networks. Road Materials and Pavement Design, 1-19.

[57] Kargah-Ostadi, N., Stoffels, S. M., & Tabatabaee, N. (2010). Network-level pavement roughness prediction model for rehabilitation recommendations. Transportation Research Record, 2155(1), 124-133.

[58] Lou, Z., Gunaratne, M., Lu, J. J., & Dietrich, B. (2001). Application of neural network model to forecast short-term pavement crack condition: Florida case study. Journal of infrastructure systems, 7(4), 166-171.

[59] Fligner, M. A., & Killeen, T. J. (1976). Distribution-free two-sample tests for scale. Journal of the American Statistical Association, 71(353), 210-213.

[60] Abu-Farsakh, M. Y., & Mojumder, M. A. H. (2020). Exploring Artificial Neural Network to Evaluate the Undrained Shear Strength of Soil from Cone Penetration Test Data. Transportation Research Record, 0361198120912426.

[61] MATLAB and Statistics Toolbox Release 2019b, The MathWorks, Inc., Natick, Massachusetts, United States.

[62] Shi, Y., Cui, L., Qi, Z., Meng, F., & Chen, Z. (2016). Automatic road crack detection using random structured forests. IEEE Transactions on Intelligent Transportation Systems, 17(12), 3434-3445.

[63] Cui, L., Qi, Z., Chen, Z., Meng, F., & Shi, Y. (2015, August). Pavement distress detection using random decision forests. In International Conference on Data Science (pp. 95-102). Springer, Cham.

Appendix A

To quantify a difference level percentage between the selected treatment types by the two cracking measurement datasets, a treatment selection exercise was conducted using the computed ALCR and RNDM indices according to the DOTD's current trigger values for different treatment selections as shown in Figures A-1, A-2 and A-3 for the collector, arterial, and interstate roads, respectively.

Figure 39. DOTD treatment triggers for collector roads

Index	0-55	60	70	75	80	85	90	95	98	100
ALCR	In-Place Stabilization	Medium Overlay			Thin Overlay		Polymer Surface Treatment		Ultra-thin Overlay	Micro-surfacing
RNDM	Medium Overlay			Thin Overlay		Polymer Surface Treatment		Ultra-thin overlay	Micro-surfacing	

Figure 40. DOTD treatment triggers for arterial roads

Index	0-60	65	70	75	80	85	90	95	98	100
ALCR	Structural Overlay	Medium Overlay				Thin Overlay		Ultra-thin Overlay		Micro-surfacing
RNDM	Medium Overlay					Thin Overlay			Micro-surfacing	

Figure 41. DOTD treatment triggers for interstates and freeways

Index	0-65	70	75	80	85	90	95	98	100
ALCR	Structural Overlay	Medium Overlay					Thin Overlay	Ultra-thin Overlay	Micro-surfacing
RNDM	Medium Overlay					Thin Overlay	Ultra-thin Overlay	Micro-surfacing	

Tables A-1, A-2, and A-3 present the impacts of change in treatment plans from the automated measurements based on the cracking measurements of 0.1-mile subsections for the collector, arterial, and interstate roads, respectively. Note that, by excluding those subsections with no detectable cracks measured by both survey methods, there are in total 88, 68, and 41 subsections of 0.1 mile each for the collector, arterial, and interstate pavement subsections used in the treatment selection comparison. In addition, there are 23 control sections involved in the selected flexible pavement projects. Using the average cracking indices of a control section in the treatment selection, Table A-4 shows the changes in treatment plans between the 3D automated and manual cracking measurement methods.

Overall, Tables A-1 to A-3 indicate, on average, 39% of 0.1-mile sections yielded different treatment triggers than the manual measurements. A similar percentage of the plan change, 39%, was found in Table A-4 based on the control sections in which 9 out of 23 control sections (39%) yielded different treatment plans for automated measurements when compared to the reference values.

Table 25. Treatment selection matrix from manual and automated measurements for collector type roads

		Automated Treatment							
		DN	MS	PST	UTO	TO	MO	IPS	Change
Manual Treatment	DN	11	5	0	1	0	0	0	35.3%
	MS	2	8	3	0	0	0	0	38.5%
	PST	0	1	20	2	6	3	0	37.5%
	UTO	0	1	0	3	1	0	0	40%
	TO	0	0	7	0	24	18	0	51%
	MO	0	0	0	1	6	20	3	33.3%
	IPS	0	0	0	0	0	2	2	50%

DN = Do Nothing; MS = Micro-surfacing; PST = Polymer Surface Treatment; UTO = Ultra-thin Overlay; TO = Thin Overlay; MO = Medium Overlay and IPS = In-Place Stabilization.

Table 26. Treatment selection matrix from manual and automated measurements for arterial type roads

		Automated Treatment						
		DN	MS	UTO	TO	MO	SO	Change
Manual Treatment	DN	14	4	1	1	0	0	30.0%
	MS	2	19	2	3	1	0	29.6%
	UTO	0	1	9	4	2	0	43.8%
	TO	0	0	4	12	7	0	47.8%
	MO	0	0	0	3	8	2	38.5%
	SO	0	0	0	0	3	6	33.3%

DN = Do Nothing; MS = Micro-surfacing; UTO = Ultra-thin Overlay; TO = Thin Overlay; MO = Medium Overlay and SO = Structural Overlay.

Table 27. Treatment selection matrix from manual and automated measurements for interstates

		Automated Treatment						
		DN	MS	UTO	TO	MO	SO	Change
Manual Treatment	DN	5	3	0	0	0	0	37.5%
	MS	1	5	0	1	2	0	44.4%
	UTO	0	0	3	2	1	0	50%
	TO	0	0	0	3	3	0	50%
	MO	0	0	0	7	22	3	31.2%
	SO	0	0	0	0	0	3	0%

DN = Do Nothing; MS = Micro-surfacing; UTO = Ultra-thin Overlay; TO = Thin Overlay; MO = Medium Overlay and SO = Structural Overlay.

Table 28. Treatment selection matrix for every control sections used in this project

		Automated Treatment								
		DN	MS	PST	UTO	TO	MO	IPS	Change	Avg. Change
Manual Treatment	DN	0	0	0	0	0	0	0	0%	38.77%
	MS	0	5	0	1	1	0	0	28.6%	
	PST	0	0	0	0	1	0	0	100%	
	UTO	0	1	0	0	1	1	0	100%	
	TO	0	0	0	0	4	3	0	42.8%	
	MO	0	0	0	0	0	5	0	0%	
	IPS or SO	0	0	0	0	0	0	0	0%	

Appendix B

Mathematical Expression for Developed ANN Model

An ANN model usually takes the form of a function of outputs with respect to inputs. The ANN model in this study takes the inputs ALCR_H, ALCR_M, ALCR_L, LONG_H, LONG_M, LONG_L, TRAN_H, TRAN_M, TRAN_L, Rut_Avg, IRI_Avg, Texture_MPD, Air Temp, TreatmentAge, Treatment_Class, to produce the outputs ALCR_H1, ALCR_M1, ALCR_L1, LONG_H1, LONG_M1, LONG_L1, TRAN_H1, TRAN_M1, TRAN_L1, respectively. Since the developed model includes a series of input, hidden perceptron (hidden) and output layers and each has different numbers of neurons, its mathematical expression needs to be represented by the data flow in the prediction through a scaling input layer, the perceptron layers and an unscaling output layer. The mathematical expression for the developed ANN model can be expressed below, which includes a series of mathematical functions expressed for the information data flow in a feed-forward fashion.

scaled_ALCR_H = ALCR_H*(1+1)/(254.529007-(0))-0*(1+1)/(254.529007-0)-1;
scaled_ALCR_M = ALCR_M*(1+1)/(2582.48999-(0))-0*(1+1)/(2582.48999-0)-1;
scaled_ALCR_L = ALCR_L*(1+1)/(1618-(0))-0*(1+1)/(1618-0)-1;
scaled_LONG_H = LONG_H*(1+1)/(100.4820023-(0))-0*(1+1)/(100.4820023-0)-1;
scaled_LONG_M = LONG_M*(1+1)/(737.5980225-(0))-0*(1+1)/(737.5980225-0)-1;
scaled_LONG_L = LONG_L*(1+1)/(357-(0))-0*(1+1)/(357-0)-1;
scaled_TRAN_H = TRAN_H*(1+1)/(396.4580078-(0))-0*(1+1)/(396.4580078-0)-1;
scaled_TRAN_M = TRAN_M*(1+1)/(1914.540039-(0))-0*(1+1)/(1914.540039-0)-1;
scaled_TRAN_L = TRAN_L*(1+1)/(667.4769897-(0))-0*(1+1)/(667.4769897-0)-1;
scaled_Rut_Avg = Rut_Avg*(1+1)/(305-(0.0700000003))-0.0700000003*(1+1)/(305-0.0700000003)-1;
scaled_IRI_Avg = IRI_Avg*(1+1)/(518-(-1))+1*(1+1)/(518+1)-1;
scaled_Texture_MPD = Texture_MPD*(1+1)/(0.08519999683-(0.01099999994))-
0.01099999994*(1+1)/(0.08519999683-0.01099999994)-1;
scaled_Air Temp = Air Temp*(1+1)/(93.5-(56.5))-56.5*(1+1)/(93.5-56.5)-1;
scaled_TreatmentAge = TreatmentAge*(1+1)/(36-(0))-0*(1+1)/(36-0)-1;
scaled_Treatment_Class = Treatment_Class*(1+1)/(6-(1))-1*(1+1)/(6-1)-1;
perceptron_layer_0_output_0 = sigma[-0.125671 + (scaled_ALCR_H*0.167294)+
(scaled_ALCR_M*1.06395)+ (scaled_ALCR_L*-0.711778)+ (scaled_LONG_H*0.320123)+
(scaled_LONG_M*-0.364759)+ (scaled_LONG_L*0.118011)+ (scaled_TRAN_H*-0.0325401)+
(scaled_TRAN_M*0.849402)+ (scaled_TRAN_L*-0.449344)+ (scaled_Rut_Avg*-0.133349)+
(scaled_IRI_Avg*-0.57683)+ (scaled_Texture_MPD*-0.421644)+ (scaled_Air Temp*0.509927)+
(scaled_TreatmentAge*0.535243)+ (scaled_Treatment_Class*0.829728)];
perceptron_layer_0_output_1 = sigma[0.21364 + (scaled_ALCR_H*-0.0688495)+
(scaled_ALCR_M*0.0370861)+ (scaled_ALCR_L*0.507893)+ (scaled_LONG_H*-0.531505)+
(scaled_LONG_M*0.174808)+ (scaled_LONG_L*0.135333)+ (scaled_TRAN_H*-0.594031)+
(scaled_TRAN_M*-0.458052)+ (scaled_TRAN_L*-0.310612)+ (scaled_Rut_Avg*-0.96653)+
(scaled_IRI_Avg*0.542529)+ (scaled_Texture_MPD*0.921245)+ (scaled_Air Temp*-0.333395)+
(scaled_TreatmentAge*-0.950853)+ (scaled_Treatment_Class*-0.818309)];
perceptron_layer_0_output_2 = sigma[0.198477 + (scaled_ALCR_H*0.215623)+ (scaled_ALCR_M*-
0.329002)+ (scaled_ALCR_L*0.203283)+ (scaled_LONG_H*0.303117)+ (scaled_LONG_M*1.24122)+
(scaled_LONG_L*0.188608)+ (scaled_TRAN_H*-0.291638)+ (scaled_TRAN_M*0.511611)+
(scaled_TRAN_L*1.70097)+ (scaled_Rut_Avg*1.00721)+ (scaled_IRI_Avg*0.386698)+

(scaled_Texture_MPD*0.109986)+ (scaled_Air Temp*-0.350448)+ (scaled_TreatmentAge*0.450518)+ (scaled_Treatment_Class*0.675231)];
perceptron_layer_0_output_3 = sigma[0.00863233 + (scaled_ALCR_H*0.0586587)+ (scaled_ALCR_M*-0.210533)+ (scaled_ALCR_L*-0.0994667)+ (scaled_LONG_H*0.0397918)+ (scaled_LONG_M*0.129864)+ (scaled_LONG_L*1.30034)+ (scaled_TRAN_H*0.132794)+ (scaled_TRAN_M*-0.00617421)+ (scaled_TRAN_L*0.27278)+ (scaled_Rut_Avg*-0.10203)+ (scaled_IRI_Avg*-0.190013)+ (scaled_Texture_MPD*0.268355)+ (scaled_Air Temp*0.108965)+ (scaled_TreatmentAge*-0.682672)+ (scaled_Treatment_Class*0.351473)];
perceptron_layer_0_output_4 = sigma[-0.0417946 + (scaled_ALCR_H*0.0628377)+ (scaled_ALCR_M*0.913088)+ (scaled_ALCR_L*-0.014739)+ (scaled_LONG_H*0.215891)+ (scaled_LONG_M*0.690274)+ (scaled_LONG_L*0.312424)+ (scaled_TRAN_H*-0.470958)+ (scaled_TRAN_M*-0.629645)+ (scaled_TRAN_L*0.349286)+ (scaled_Rut_Avg*-0.119791)+ (scaled_IRI_Avg*-0.268982)+ (scaled_Texture_MPD*0.132698)+ (scaled_Air Temp*0.389531)+ (scaled_TreatmentAge*-0.377493)+ (scaled_Treatment_Class*-0.414914)];
perceptron_layer_0_output_5 = sigma[-0.308396 + (scaled_ALCR_H*-0.0731325)+ (scaled_ALCR_M*-0.00527642)+ (scaled_ALCR_L*0.542128)+ (scaled_LONG_H*0.204281)+ (scaled_LONG_M*0.937124)+ (scaled_LONG_L*0.209156)+ (scaled_TRAN_H*0.106183)+ (scaled_TRAN_M*-0.891726)+ (scaled_TRAN_L*-0.652341)+ (scaled_Rut_Avg*0.595185)+ (scaled_IRI_Avg*-0.449126)+ (scaled_Texture_MPD*-0.152145)+ (scaled_Air Temp*-0.0262722)+ (scaled_TreatmentAge*0.0952771)+ (scaled_Treatment_Class*-0.0631565)];
perceptron_layer_0_output_6 = sigma[0.237426 + (scaled_ALCR_H*-0.516168)+ (scaled_ALCR_M*1.53012)+ (scaled_ALCR_L*-0.2627)+ (scaled_LONG_H*-0.355355)+ (scaled_LONG_M*0.453832)+ (scaled_LONG_L*0.0268586)+ (scaled_TRAN_H*0.0307848)+ (scaled_TRAN_M*0.558933)+ (scaled_TRAN_L*0.679047)+ (scaled_Rut_Avg*0.36379)+ (scaled_IRI_Avg*0.123474)+ (scaled_Texture_MPD*0.37842)+ (scaled_Air Temp*-0.131581)+ (scaled_TreatmentAge*0.256468)+ (scaled_Treatment_Class*-0.38574)];
perceptron_layer_0_output_7 = sigma[-0.587799 + (scaled_ALCR_H*0.226224)+ (scaled_ALCR_M*-0.288476)+ (scaled_ALCR_L*-1.16245)+ (scaled_LONG_H*0.392331)+ (scaled_LONG_M*-0.482162)+ (scaled_LONG_L*-0.174288)+ (scaled_TRAN_H*0.0610641)+ (scaled_TRAN_M*0.343147)+ (scaled_TRAN_L*-0.125753)+ (scaled_Rut_Avg*0.105367)+ (scaled_IRI_Avg*0.538758)+ (scaled_Texture_MPD*-0.195669)+ (scaled_Air Temp*-1.04171)+ (scaled_TreatmentAge*-0.307383)+ (scaled_Treatment_Class*1.55273)];
perceptron_layer_0_output_8 = sigma[-0.69152 + (scaled_ALCR_H*-0.293692)+ (scaled_ALCR_M*-0.887119)+ (scaled_ALCR_L*0.0273406)+ (scaled_LONG_H*0.463292)+ (scaled_LONG_M*0.85432)+ (scaled_LONG_L*-0.290734)+ (scaled_TRAN_H*0.79692)+ (scaled_TRAN_M*1.23435)+ (scaled_TRAN_L*1.37542)+ (scaled_Rut_Avg*-0.362723)+ (scaled_IRI_Avg*-0.0813753)+ (scaled_Texture_MPD*0.613364)+ (scaled_Air Temp*0.749112)+ (scaled_TreatmentAge*-0.351639)+ (scaled_Treatment_Class*-0.293722)];
perceptron_layer_0_output_9 = sigma[0.228557 + (scaled_ALCR_H*-0.363664)+ (scaled_ALCR_M*-0.0937628)+ (scaled_ALCR_L*0.137772)+ (scaled_LONG_H*0.0571189)+ (scaled_LONG_M*1.85458)+ (scaled_LONG_L*-0.0966858)+ (scaled_TRAN_H*0.292924)+ (scaled_TRAN_M*0.58972)+ (scaled_TRAN_L*-0.226056)+ (scaled_Rut_Avg*-0.699528)+ (scaled_IRI_Avg*-0.533407)+ (scaled_Texture_MPD*0.238618)+ (scaled_Air Temp*-0.197319)+ (scaled_TreatmentAge*-0.31775)+ (scaled_Treatment_Class*-0.683279)];
perceptron_layer_0_output_10 = sigma[-0.157589 + (scaled_ALCR_H*0.447297)+ (scaled_ALCR_M*-1.03598)+ (scaled_ALCR_L*0.267672)+ (scaled_LONG_H*-0.528144)+ (scaled_LONG_M*-0.725698)+ (scaled_LONG_L*-0.702337)+ (scaled_TRAN_H*0.0514497)+ (scaled_TRAN_M*-0.236046)+ (scaled_TRAN_L*0.0915667)+ (scaled_Rut_Avg*-0.112654)+ (scaled_IRI_Avg*-0.0608853)+ (scaled_Texture_MPD*0.36471)+ (scaled_Air Temp*0.0440283)+ (scaled_TreatmentAge*0.0930323)+ (scaled_Treatment_Class*-0.840582)];
perceptron_layer_0_output_11 = sigma[-0.265473 + (scaled_ALCR_H*0.415655)+ (scaled_ALCR_M*-0.729189)+ (scaled_ALCR_L*-0.216293)+ (scaled_LONG_H*0.117049)+ (scaled_LONG_M*-0.321638)+ (scaled_LONG_L*0.504553)+ (scaled_TRAN_H*-0.136932)+ (scaled_TRAN_M*-0.454783)+ (scaled_TRAN_L*-0.463926)+ (scaled_Rut_Avg*0.537014)+ (scaled_IRI_Avg*-0.408213)+

(scaled_Texture_MPD*-0.426573)+ (scaled_Air Temp*-0.519522)+ (scaled_TreatmentAge*0.0384133)+ (scaled_Treatment_Class*-1.09008)];
perceptron_layer_0_output_12 = sigma[0.447267 + (scaled_ALCR_H*-0.122616)+ (scaled_ALCR_M*-0.0123976)+ (scaled_ALCR_L*0.251749)+ (scaled_LONG_H*-0.0222749)+ (scaled_LONG_M*0.132437)+ (scaled_LONG_L*-0.177064)+ (scaled_TRAN_H*-0.283903)+ (scaled_TRAN_M*-0.953804)+ (scaled_TRAN_L*0.436791)+ (scaled_Rut_Avg*0.314132)+ (scaled_IRI_Avg*0.91511)+ (scaled_Texture_MPD*-0.042266)+ (scaled_Air Temp*-1.37107)+ (scaled_TreatmentAge*-0.823338)+ (scaled_Treatment_Class*1.23292)];
perceptron_layer_0_output_13 = sigma[-0.0289586 + (scaled_ALCR_H*-0.162177)+ (scaled_ALCR_M*0.527159)+ (scaled_ALCR_L*0.458899)+ (scaled_LONG_H*-0.066651)+ (scaled_LONG_M*-0.647503)+ (scaled_LONG_L*0.472325)+ (scaled_TRAN_H*0.280233)+ (scaled_TRAN_M*0.498707)+ (scaled_TRAN_L*-0.534394)+ (scaled_Rut_Avg*0.233431)+ (scaled_IRI_Avg*-0.156681)+ (scaled_Texture_MPD*0.316506)+ (scaled_Air Temp*-0.370631)+ (scaled_TreatmentAge*-0.706031)+ (scaled_Treatment_Class*-0.88583)];
perceptron_layer_0_output_14 = sigma[-0.112313 + (scaled_ALCR_H*0.363274)+ (scaled_ALCR_M*-0.564889)+ (scaled_ALCR_L*-0.402709)+ (scaled_LONG_H*-0.074953)+ (scaled_LONG_M*0.96401)+ (scaled_LONG_L*1.18934)+ (scaled_TRAN_H*-0.323646)+ (scaled_TRAN_M*-0.832774)+ (scaled_TRAN_L*0.945726)+ (scaled_Rut_Avg*-0.307141)+ (scaled_IRI_Avg*0.560482)+ (scaled_Texture_MPD*-0.33986)+ (scaled_Air Temp*-0.0700147)+ (scaled_TreatmentAge*0.724687)+ (scaled_Treatment_Class*-0.0362189)];
perceptron_layer_0_output_15 = sigma[0.20157 + (scaled_ALCR_H*-0.139847)+ (scaled_ALCR_M*0.485766)+ (scaled_ALCR_L*0.511045)+ (scaled_LONG_H*0.0308218)+ (scaled_LONG_M*0.52251)+ (scaled_LONG_L*0.721622)+ (scaled_TRAN_H*-0.165469)+ (scaled_TRAN_M*-0.623958)+ (scaled_TRAN_L*-0.346875)+ (scaled_Rut_Avg*0.0841056)+ (scaled_IRI_Avg*-0.281963)+ (scaled_Texture_MPD*-0.0463051)+ (scaled_Air Temp*0.451902)+ (scaled_TreatmentAge*0.515228)+ (scaled_Treatment_Class*0.287376)];
perceptron_layer_0_output_16 = sigma[-0.111451 + (scaled_ALCR_H*-0.0924763)+ (scaled_ALCR_M*-0.411665)+ (scaled_ALCR_L*-1.13599)+ (scaled_LONG_H*-0.438027)+ (scaled_LONG_M*0.711242)+ (scaled_LONG_L*0.0460177)+ (scaled_TRAN_H*0.287867)+ (scaled_TRAN_M*0.35688)+ (scaled_TRAN_L*-0.924045)+ (scaled_Rut_Avg*-0.151013)+ (scaled_IRI_Avg*0.391926)+ (scaled_Texture_MPD*-0.429823)+ (scaled_Air Temp*-1.01103)+ (scaled_TreatmentAge*-0.735971)+ (scaled_Treatment_Class*0.560051)];
perceptron_layer_0_output_17 = sigma[0.690179 + (scaled_ALCR_H*0.0462878)+ (scaled_ALCR_M*-1.97815)+ (scaled_ALCR_L*1.33229)+ (scaled_LONG_H*-0.20291)+ (scaled_LONG_M*-0.835808)+ (scaled_LONG_L*-0.422673)+ (scaled_TRAN_H*-0.438866)+ (scaled_TRAN_M*0.13635)+ (scaled_TRAN_L*0.104529)+ (scaled_Rut_Avg*0.234601)+ (scaled_IRI_Avg*-0.570884)+ (scaled_Texture_MPD*0.262312)+ (scaled_Air Temp*1.05084)+ (scaled_TreatmentAge*-0.338812)+ (scaled_Treatment_Class*0.443641)];
perceptron_layer_0_output_18 = sigma[-0.182216 + (scaled_ALCR_H*-0.453629)+ (scaled_ALCR_M*-0.235336)+ (scaled_ALCR_L*-0.183886)+ (scaled_LONG_H*-0.0958681)+ (scaled_LONG_M*0.148302)+ (scaled_LONG_L*-0.923234)+ (scaled_TRAN_H*0.111034)+ (scaled_TRAN_M*-0.1272)+ (scaled_TRAN_L*0.137265)+ (scaled_Rut_Avg*0.0932599)+ (scaled_IRI_Avg*-0.208492)+ (scaled_Texture_MPD*-0.117315)+ (scaled_Air Temp*0.0726845)+ (scaled_TreatmentAge*-0.241787)+ (scaled_Treatment_Class*-0.0241347)];
perceptron_layer_0_output_19 = sigma[0.0551069 + (scaled_ALCR_H*-0.0459564)+ (scaled_ALCR_M*0.0733528)+ (scaled_ALCR_L*0.0318089)+ (scaled_LONG_H*-0.0757795)+ (scaled_LONG_M*-0.0057755)+ (scaled_LONG_L*0.448602)+ (scaled_TRAN_H*0.151879)+ (scaled_TRAN_M*0.170641)+ (scaled_TRAN_L*-0.164659)+ (scaled_Rut_Avg*0.189321)+ (scaled_IRI_Avg*0.0467969)+ (scaled_Texture_MPD*0.0535255)+ (scaled_Air Temp*-0.0436712)+ (scaled_TreatmentAge*0.214834)+ (scaled_Treatment_Class*0.158708)];
perceptron_layer_1_output_0 = sigma[0.104129 + (perceptron_layer_0_output_0*-0.647455)+ (perceptron_layer_0_output_1*-0.463054)+ (perceptron_layer_0_output_2*-0.117682)+ (perceptron_layer_0_output_3*-0.426503)+ (perceptron_layer_0_output_4*0.102697)+ (perceptron_layer_0_output_5*0.0127523)+ (perceptron_layer_0_output_6*-0.361424)+ (perceptron_layer_0_output_7*0.0302036)+ (perceptron_layer_0_output_8*0.0206867)+

(perceptron_layer_0_output_9*0.481093)+ (perceptron_layer_0_output_10*0.672798)+
(perceptron_layer_0_output_11*-0.445851)+ (perceptron_layer_0_output_12*-0.436892)+
(perceptron_layer_0_output_13*0.197316)+ (perceptron_layer_0_output_14*0.0109793)+
(perceptron_layer_0_output_15*0.0363113)+ (perceptron_layer_0_output_16*0.479775)+
(perceptron_layer_0_output_17*-0.0245799)+ (perceptron_layer_0_output_18*0.664737)+
(perceptron_layer_0_output_19*-0.171711)];
perceptron_layer_1_output_1 = sigma[-0.0393673 + (perceptron_layer_0_output_0*-0.286207)+
(perceptron_layer_0_output_1*-0.342754)+ (perceptron_layer_0_output_2*-0.0678882)+
(perceptron_layer_0_output_3*0.22177)+ (perceptron_layer_0_output_4*0.506602)+
(perceptron_layer_0_output_5*-0.025757)+ (perceptron_layer_0_output_6*0.011196)+
(perceptron_layer_0_output_7*0.567944)+ (perceptron_layer_0_output_8*0.829358)+
(perceptron_layer_0_output_9*-0.639976)+ (perceptron_layer_0_output_10*0.701926)+
(perceptron_layer_0_output_11*-0.266449)+ (perceptron_layer_0_output_12*-0.411725)+
(perceptron_layer_0_output_13*0.352304)+ (perceptron_layer_0_output_14*0.179891)+
(perceptron_layer_0_output_15*-0.206907)+ (perceptron_layer_0_output_16*-0.328637)+
(perceptron_layer_0_output_17*-0.402519)+ (perceptron_layer_0_output_18*0.41976)+
(perceptron_layer_0_output_19*-0.129849)];
perceptron_layer_1_output_2 = sigma[-0.00245605 + (perceptron_layer_0_output_0*-0.0886572)+
(perceptron_layer_0_output_1*-0.262526)+ (perceptron_layer_0_output_2*-0.0494305)+
(perceptron_layer_0_output_3*0.571301)+ (perceptron_layer_0_output_4*-0.018864)+
(perceptron_layer_0_output_5*-0.231792)+ (perceptron_layer_0_output_6*0.204848)+
(perceptron_layer_0_output_7*0.35224)+ (perceptron_layer_0_output_8*-0.143354)+
(perceptron_layer_0_output_9*0.0864728)+ (perceptron_layer_0_output_10*-0.397163)+
(perceptron_layer_0_output_11*-0.0628193)+ (perceptron_layer_0_output_12*-0.422776)+
(perceptron_layer_0_output_13*-0.00217053)+ (perceptron_layer_0_output_14*0.137665)+
(perceptron_layer_0_output_15*0.0732777)+ (perceptron_layer_0_output_16*0.148644)+
(perceptron_layer_0_output_17*0.575857)+ (perceptron_layer_0_output_18*-0.357959)+
(perceptron_layer_0_output_19*0.219029)];
perceptron_layer_1_output_3 = sigma[-0.000914043 + (perceptron_layer_0_output_0*-0.762549)+
(perceptron_layer_0_output_1*0.573241)+ (perceptron_layer_0_output_2*-0.15534)+
(perceptron_layer_0_output_3*-0.0789128)+ (perceptron_layer_0_output_4*-0.778963)+
(perceptron_layer_0_output_5*-0.102185)+ (perceptron_layer_0_output_6*-0.23921)+
(perceptron_layer_0_output_7*0.389359)+ (perceptron_layer_0_output_8*0.0725975)+
(perceptron_layer_0_output_9*-0.388972)+ (perceptron_layer_0_output_10*1.01237)+
(perceptron_layer_0_output_11*0.741025)+ (perceptron_layer_0_output_12*0.589996)+
(perceptron_layer_0_output_13*-0.0214207)+ (perceptron_layer_0_output_14*-0.155855)+
(perceptron_layer_0_output_15*-0.641227)+ (perceptron_layer_0_output_16*0.566636)+
(perceptron_layer_0_output_17*0.181435)+ (perceptron_layer_0_output_18*0.256578)+
(perceptron_layer_0_output_19*-0.0252222)];
perceptron_layer_1_output_4 = sigma[0.0912095 + (perceptron_layer_0_output_0*-0.212683)+
(perceptron_layer_0_output_1*0.224718)+ (perceptron_layer_0_output_2*-0.331596)+
(perceptron_layer_0_output_3*-0.42372)+ (perceptron_layer_0_output_4*-0.0374133)+
(perceptron_layer_0_output_5*0.517585)+ (perceptron_layer_0_output_6*0.176383)+
(perceptron_layer_0_output_7*-0.0494262)+ (perceptron_layer_0_output_8*0.541378)+
(perceptron_layer_0_output_9*-0.375518)+ (perceptron_layer_0_output_10*-0.137543)+
(perceptron_layer_0_output_11*0.194293)+ (perceptron_layer_0_output_12*-0.220046)+
(perceptron_layer_0_output_13*-0.340809)+ (perceptron_layer_0_output_14*-0.564586)+
(perceptron_layer_0_output_15*0.0759475)+ (perceptron_layer_0_output_16*0.0675301)+
(perceptron_layer_0_output_17*-0.0543994)+ (perceptron_layer_0_output_18*0.300475)+
(perceptron_layer_0_output_19*-0.0833018)];
perceptron_layer_1_output_5 = sigma[0.0150812 + (perceptron_layer_0_output_0*-0.225553)+
(perceptron_layer_0_output_1*1.27801)+ (perceptron_layer_0_output_2*0.5063)+
(perceptron_layer_0_output_3*0.110221)+ (perceptron_layer_0_output_4*0.235721)+
(perceptron_layer_0_output_5*0.455489)+ (perceptron_layer_0_output_6*-0.178922)+
(perceptron_layer_0_output_7*-0.459178)+ (perceptron_layer_0_output_8*0.570087)+

(perceptron_layer_0_output_9*0.529425)+ (perceptron_layer_0_output_10*-1.01236)+
(perceptron_layer_0_output_11*-0.09215)+ (perceptron_layer_0_output_12*0.299105)+
(perceptron_layer_0_output_13*-0.848634)+ (perceptron_layer_0_output_14*0.183107)+
(perceptron_layer_0_output_15*0.248131)+ (perceptron_layer_0_output_16*0.0624211)+
(perceptron_layer_0_output_17*0.63752)+ (perceptron_layer_0_output_18*-0.266351)+
(perceptron_layer_0_output_19*-0.0421653)];
perceptron_layer_1_output_6 = sigma[0.140997 + (perceptron_layer_0_output_0*-0.320128)+
(perceptron_layer_0_output_1*-0.722233)+ (perceptron_layer_0_output_2*-0.634231)+
(perceptron_layer_0_output_3*-0.518926)+ (perceptron_layer_0_output_4*0.133228)+
(perceptron_layer_0_output_5*0.264434)+ (perceptron_layer_0_output_6*-0.264307)+
(perceptron_layer_0_output_7*-0.450357)+ (perceptron_layer_0_output_8*-0.0378957)+
(perceptron_layer_0_output_9*0.644327)+ (perceptron_layer_0_output_10*0.00930418)+
(perceptron_layer_0_output_11*-0.987714)+ (perceptron_layer_0_output_12*-0.12189)+
(perceptron_layer_0_output_13*-0.186738)+ (perceptron_layer_0_output_14*0.654085)+
(perceptron_layer_0_output_15*0.611409)+ (perceptron_layer_0_output_16*1.05726)+
(perceptron_layer_0_output_17*-0.492375)+ (perceptron_layer_0_output_18*0.181717)+
(perceptron_layer_0_output_19*0.107978)];
perceptron_layer_1_output_7 = sigma[0.00992885 + (perceptron_layer_0_output_0*0.213493)+
(perceptron_layer_0_output_1*-0.348485)+ (perceptron_layer_0_output_2*-0.63226)+
(perceptron_layer_0_output_3*0.425482)+ (perceptron_layer_0_output_4*-0.309112)+
(perceptron_layer_0_output_5*0.0559224)+ (perceptron_layer_0_output_6*-0.106595)+
(perceptron_layer_0_output_7*-0.765396)+ (perceptron_layer_0_output_8*0.308053)+
(perceptron_layer_0_output_9*-0.00705839)+ (perceptron_layer_0_output_10*0.14452)+
(perceptron_layer_0_output_11*-0.0425433)+ (perceptron_layer_0_output_12*0.72481)+
(perceptron_layer_0_output_13*0.529747)+ (perceptron_layer_0_output_14*0.418808)+
(perceptron_layer_0_output_15*0.324123)+ (perceptron_layer_0_output_16*-0.00981759)+
(perceptron_layer_0_output_17*-0.410643)+ (perceptron_layer_0_output_18*-0.513359)+
(perceptron_layer_0_output_19*0.343509)];
perceptron_layer_1_output_8 = sigma[0.0841339 + (perceptron_layer_0_output_0*0.18932)+
(perceptron_layer_0_output_1*-0.364488)+ (perceptron_layer_0_output_2*0.234958)+
(perceptron_layer_0_output_3*-0.358541)+ (perceptron_layer_0_output_4*-0.683927)+
(perceptron_layer_0_output_5*-0.573169)+ (perceptron_layer_0_output_6*-0.147334)+
(perceptron_layer_0_output_7*0.155274)+ (perceptron_layer_0_output_8*-0.56877)+
(perceptron_layer_0_output_9*0.294535)+ (perceptron_layer_0_output_10*-0.074846)+
(perceptron_layer_0_output_11*-0.374231)+ (perceptron_layer_0_output_12*0.332629)+
(perceptron_layer_0_output_13*0.21968)+ (perceptron_layer_0_output_14*-0.533664)+
(perceptron_layer_0_output_15*-0.232337)+ (perceptron_layer_0_output_16*0.0249636)+
(perceptron_layer_0_output_17*0.782919)+ (perceptron_layer_0_output_18*0.25349)+
(perceptron_layer_0_output_19*-0.0262325)];
perceptron_layer_1_output_9 = sigma[0.180579 + (perceptron_layer_0_output_0*-0.285551)+
(perceptron_layer_0_output_1*0.450489)+ (perceptron_layer_0_output_2*-1.1589)+
(perceptron_layer_0_output_3*-0.155952)+ (perceptron_layer_0_output_4*-0.115562)+
(perceptron_layer_0_output_5*0.642331)+ (perceptron_layer_0_output_6*0.543477)+
(perceptron_layer_0_output_7*0.154178)+ (perceptron_layer_0_output_8*0.0285512)+
(perceptron_layer_0_output_9*-0.703009)+ (perceptron_layer_0_output_10*0.0724089)+
(perceptron_layer_0_output_11*0.322703)+ (perceptron_layer_0_output_12*0.29117)+
(perceptron_layer_0_output_13*0.159017)+ (perceptron_layer_0_output_14*-1.43495)+
(perceptron_layer_0_output_15*0.435078)+ (perceptron_layer_0_output_16*-0.467226)+
(perceptron_layer_0_output_17*0.271442)+ (perceptron_layer_0_output_18*0.0709253)+
(perceptron_layer_0_output_19*0.144978)];
perceptron_layer_1_output_10 = sigma[-0.0428299 + (perceptron_layer_0_output_0*1.29226)+
(perceptron_layer_0_output_1*0.407154)+ (perceptron_layer_0_output_2*0.855228)+
(perceptron_layer_0_output_3*-0.763886)+ (perceptron_layer_0_output_4*-0.187987)+
(perceptron_layer_0_output_5*-0.476374)+ (perceptron_layer_0_output_6*-0.770667)+
(perceptron_layer_0_output_7*-0.539959)+ (perceptron_layer_0_output_8*-0.231548)+

(perceptron_layer_0_output_9*0.499138)+ (perceptron_layer_0_output_10*-0.0528767)+
(perceptron_layer_0_output_11*-0.0988023)+ (perceptron_layer_0_output_12*0.875404)+
(perceptron_layer_0_output_13*0.400277)+ (perceptron_layer_0_output_14*0.0485476)+
(perceptron_layer_0_output_15*-0.524975)+ (perceptron_layer_0_output_16*-0.960977)+
(perceptron_layer_0_output_17*-0.153716)+ (perceptron_layer_0_output_18*0.18447)+
(perceptron_layer_0_output_19*-0.244899)];
perceptron_layer_1_output_11 = sigma[-0.109835 + (perceptron_layer_0_output_0*-0.360745)+
(perceptron_layer_0_output_1*0.725951)+ (perceptron_layer_0_output_2*0.524029)+
(perceptron_layer_0_output_3*0.0633128)+ (perceptron_layer_0_output_4*0.446789)+
(perceptron_layer_0_output_5*-0.0596406)+ (perceptron_layer_0_output_6*-0.0541092)+
(perceptron_layer_0_output_7*0.0966427)+ (perceptron_layer_0_output_8*-1.27166)+
(perceptron_layer_0_output_9*-0.151159)+ (perceptron_layer_0_output_10*0.350376)+
(perceptron_layer_0_output_11*0.451807)+ (perceptron_layer_0_output_12*0.459832)+
(perceptron_layer_0_output_13*-0.0459603)+ (perceptron_layer_0_output_14*0.151605)+
(perceptron_layer_0_output_15*0.103857)+ (perceptron_layer_0_output_16*-0.587936)+
(perceptron_layer_0_output_17*0.0850952)+ (perceptron_layer_0_output_18*-0.239675)+
(perceptron_layer_0_output_19*-0.183904)];
perceptron_layer_1_output_12 = sigma[-0.0636751 + (perceptron_layer_0_output_0*0.229817)+
(perceptron_layer_0_output_1*-0.241241)+ (perceptron_layer_0_output_2*-0.118595)+
(perceptron_layer_0_output_3*0.526445)+ (perceptron_layer_0_output_4*0.137826)+
(perceptron_layer_0_output_5*-0.472089)+ (perceptron_layer_0_output_6*-0.230998)+
(perceptron_layer_0_output_7*-0.335204)+ (perceptron_layer_0_output_8*-0.769894)+
(perceptron_layer_0_output_9*0.496304)+ (perceptron_layer_0_output_10*0.148846)+
(perceptron_layer_0_output_11*-0.159306)+ (perceptron_layer_0_output_12*0.345878)+
(perceptron_layer_0_output_13*0.738948)+ (perceptron_layer_0_output_14*0.23119)+
(perceptron_layer_0_output_15*0.277352)+ (perceptron_layer_0_output_16*-0.522592)+
(perceptron_layer_0_output_17*0.211607)+ (perceptron_layer_0_output_18*-0.553513)+
(perceptron_layer_0_output_19*0.161351)];
perceptron_layer_1_output_13 = sigma[-0.10502 + (perceptron_layer_0_output_0*-0.500209)+
(perceptron_layer_0_output_1*0.229218)+ (perceptron_layer_0_output_2*0.033073)+
(perceptron_layer_0_output_3*0.176962)+ (perceptron_layer_0_output_4*-0.804388)+
(perceptron_layer_0_output_5*-0.473094)+ (perceptron_layer_0_output_6*-0.855443)+
(perceptron_layer_0_output_7*-0.271593)+ (perceptron_layer_0_output_8*-0.132431)+
(perceptron_layer_0_output_9*0.0245375)+ (perceptron_layer_0_output_10*-0.0969262)+
(perceptron_layer_0_output_11*0.578016)+ (perceptron_layer_0_output_12*-0.284102)+
(perceptron_layer_0_output_13*0.0188249)+ (perceptron_layer_0_output_14*-0.1232)+
(perceptron_layer_0_output_15*-0.68993)+ (perceptron_layer_0_output_16*0.0112806)+
(perceptron_layer_0_output_17*1.29396)+ (perceptron_layer_0_output_18*-0.328657)+
(perceptron_layer_0_output_19*0.0170515)];
perceptron_layer_1_output_14 = sigma[-0.101441 + (perceptron_layer_0_output_0*-0.619721)+
(perceptron_layer_0_output_1*0.319952)+ (perceptron_layer_0_output_2*0.519276)+
(perceptron_layer_0_output_3*0.271251)+ (perceptron_layer_0_output_4*0.314272)+
(perceptron_layer_0_output_5*-0.112718)+ (perceptron_layer_0_output_6*0.405138)+
(perceptron_layer_0_output_7*0.941607)+ (perceptron_layer_0_output_8*-0.70465)+
(perceptron_layer_0_output_9*-0.170341)+ (perceptron_layer_0_output_10*-0.134428)+
(perceptron_layer_0_output_11*0.330101)+ (perceptron_layer_0_output_12*-0.839122)+
(perceptron_layer_0_output_13*-0.539271)+ (perceptron_layer_0_output_14*-0.206852)+
(perceptron_layer_0_output_15*-0.16918)+ (perceptron_layer_0_output_16*0.119347)+
(perceptron_layer_0_output_17*0.572762)+ (perceptron_layer_0_output_18*-0.0048373)+
(perceptron_layer_0_output_19*-0.176654)];
perceptron_layer_2_output_0 = tanh[-0.0515816 + (perceptron_layer_1_output_0*0.0115157)+
(perceptron_layer_1_output_1*0.777746)+ (perceptron_layer_1_output_2*-0.301778)+
(perceptron_layer_1_output_3*0.33521)+ (perceptron_layer_1_output_4*0.616651)+
(perceptron_layer_1_output_5*-0.79815)+ (perceptron_layer_1_output_6*-0.548399)+
(perceptron_layer_1_output_7*0.418034)+ (perceptron_layer_1_output_8*-0.614436)+

(perceptron_layer_1_output_9*1.86947)+ (perceptron_layer_1_output_10*-0.786414)+
(perceptron_layer_1_output_11*0.0939117)+ (perceptron_layer_1_output_12*-0.0317761)+
(perceptron_layer_1_output_13*-0.775472)+ (perceptron_layer_1_output_14*-0.23829)];
perceptron_layer_2_output_1 = tanh[0.0771865 + (perceptron_layer_1_output_0*0.54885)+
(perceptron_layer_1_output_1*0.439384)+ (perceptron_layer_1_output_2*-0.103083)+
(perceptron_layer_1_output_3*0.779023)+ (perceptron_layer_1_output_4*0.365638)+
(perceptron_layer_1_output_5*-0.570964)+ (perceptron_layer_1_output_6*1.26494)+
(perceptron_layer_1_output_7*0.876298)+ (perceptron_layer_1_output_8*-0.0439346)+
(perceptron_layer_1_output_9*-0.119801)+ (perceptron_layer_1_output_10*-0.769536)+
(perceptron_layer_1_output_11*-1.46119)+ (perceptron_layer_1_output_12*-0.557027)+
(perceptron_layer_1_output_13*-0.0523497)+ (perceptron_layer_1_output_14*-1.08494)];
perceptron_layer_2_output_2 = tanh[0.0708365 + (perceptron_layer_1_output_0*1.07773)+
(perceptron_layer_1_output_1*0.480015)+ (perceptron_layer_1_output_2*-0.0271292)+
(perceptron_layer_1_output_3*-0.00791797)+ (perceptron_layer_1_output_4*0.493717)+
(perceptron_layer_1_output_5*-0.312098)+ (perceptron_layer_1_output_6*0.945348)+
(perceptron_layer_1_output_7*-1.17068)+ (perceptron_layer_1_output_8*-0.097628)+
(perceptron_layer_1_output_9*0.228513)+ (perceptron_layer_1_output_10*-1.28345)+
(perceptron_layer_1_output_11*0.244885)+ (perceptron_layer_1_output_12*-0.850968)+
(perceptron_layer_1_output_13*-0.560397)+ (perceptron_layer_1_output_14*1.1239)];
perceptron_layer_2_output_3 = tanh[-0.22606 + (perceptron_layer_1_output_0*-0.0169065)+
(perceptron_layer_1_output_1*-1.12511)+ (perceptron_layer_1_output_2*-0.0149653)+
(perceptron_layer_1_output_3*-0.772869)+ (perceptron_layer_1_output_4*0.356059)+
(perceptron_layer_1_output_5*0.328785)+ (perceptron_layer_1_output_6*0.0112813)+
(perceptron_layer_1_output_7*-0.308074)+ (perceptron_layer_1_output_8*1.09141)+
(perceptron_layer_1_output_9*0.968087)+ (perceptron_layer_1_output_10*0.521971)+
(perceptron_layer_1_output_11*-0.280261)+ (perceptron_layer_1_output_12*-0.0990795)+
(perceptron_layer_1_output_13*0.817331)+ (perceptron_layer_1_output_14*-0.278106)];
perceptron_layer_2_output_4 = tanh[0.0713997 + (perceptron_layer_1_output_0*-0.0151948)+
(perceptron_layer_1_output_1*-0.0244298)+ (perceptron_layer_1_output_2*0.289455)+
(perceptron_layer_1_output_3*0.0692509)+ (perceptron_layer_1_output_4*-0.200404)+
(perceptron_layer_1_output_5*-0.0105239)+ (perceptron_layer_1_output_6*-0.0726341)+
(perceptron_layer_1_output_7*0.188801)+ (perceptron_layer_1_output_8*0.393852)+
(perceptron_layer_1_output_9*-0.189215)+ (perceptron_layer_1_output_10*-0.116173)+
(perceptron_layer_1_output_11*-0.187855)+ (perceptron_layer_1_output_12*0.168359)+
(perceptron_layer_1_output_13*0.633273)+ (perceptron_layer_1_output_14*0.0189201)];
perceptron_layer_2_output_5 = tanh[0.0242839 + (perceptron_layer_1_output_0*0.192147)+
(perceptron_layer_1_output_1*0.137419)+ (perceptron_layer_1_output_2*-0.00722273)+
(perceptron_layer_1_output_3*0.0803185)+ (perceptron_layer_1_output_4*0.0575513)+
(perceptron_layer_1_output_5*0.264942)+ (perceptron_layer_1_output_6*-0.10443)+
(perceptron_layer_1_output_7*-0.0121484)+ (perceptron_layer_1_output_8*-0.125224)+
(perceptron_layer_1_output_9*0.118655)+ (perceptron_layer_1_output_10*0.0255666)+
(perceptron_layer_1_output_11*-0.0354069)+ (perceptron_layer_1_output_12*0.0720154)+
(perceptron_layer_1_output_13*0.452785)+ (perceptron_layer_1_output_14*-0.0695702)];
perceptron_layer_2_output_6 = tanh[0.0428046 + (perceptron_layer_1_output_0*0.632282)+
(perceptron_layer_1_output_1*0.546215)+ (perceptron_layer_1_output_2*-0.832424)+
(perceptron_layer_1_output_3*0.309039)+ (perceptron_layer_1_output_4*-0.0923444)+
(perceptron_layer_1_output_5*-0.859496)+ (perceptron_layer_1_output_6*0.080085)+
(perceptron_layer_1_output_7*-0.0238451)+ (perceptron_layer_1_output_8*0.401167)+
(perceptron_layer_1_output_9*-0.585601)+ (perceptron_layer_1_output_10*1.86954)+
(perceptron_layer_1_output_11*0.0846662)+ (perceptron_layer_1_output_12*0.0291675)+
(perceptron_layer_1_output_13*-0.586069)+ (perceptron_layer_1_output_14*-0.876303)];
perceptron_layer_2_output_7 = tanh[-0.125646 + (perceptron_layer_1_output_0*0.443633)+
(perceptron_layer_1_output_1*-0.769235)+ (perceptron_layer_1_output_2*-0.201459)+
(perceptron_layer_1_output_3*-0.266465)+ (perceptron_layer_1_output_4*-0.589437)+
(perceptron_layer_1_output_5*-0.382495)+ (perceptron_layer_1_output_6*1.17852)+

(perceptron_layer_1_output_7*0.87177)+ (perceptron_layer_1_output_8*-0.0513616)+
(perceptron_layer_1_output_9*-0.278691)+ (perceptron_layer_1_output_10*-0.0494555)+
(perceptron_layer_1_output_11*0.759153)+ (perceptron_layer_1_output_12*1.16022)+
(perceptron_layer_1_output_13*-0.534969)+ (perceptron_layer_1_output_14*-0.485407)];
perceptron_layer_2_output_8 = tanh[0.076846 + (perceptron_layer_1_output_0*-0.44366)+
(perceptron_layer_1_output_1*-0.514749)+ (perceptron_layer_1_output_2*-0.586535)+
(perceptron_layer_1_output_3*0.214326)+ (perceptron_layer_1_output_4*0.635968)+
(perceptron_layer_1_output_5*1.27726)+ (perceptron_layer_1_output_6*0.175517)+
(perceptron_layer_1_output_7*0.147926)+ (perceptron_layer_1_output_8*-0.758864)+
(perceptron_layer_1_output_9*0.341131)+ (perceptron_layer_1_output_10*0.175421)+
(perceptron_layer_1_output_11*-0.0138599)+ (perceptron_layer_1_output_12*-0.881938)+
(perceptron_layer_1_output_13*-0.238935)+ (perceptron_layer_1_output_14*-0.368469)];
perceptron_layer_2_output_9 = tanh[0.115453 + (perceptron_layer_1_output_0*0.252942)+
(perceptron_layer_1_output_1*0.366401)+ (perceptron_layer_1_output_2*0.290764)+
(perceptron_layer_1_output_3*-1.63351)+ (perceptron_layer_1_output_4*0.0139699)+
(perceptron_layer_1_output_5*0.0358202)+ (perceptron_layer_1_output_6*1.06232)+
(perceptron_layer_1_output_7*0.298764)+ (perceptron_layer_1_output_8*-0.367329)+
(perceptron_layer_1_output_9*-0.0875363)+ (perceptron_layer_1_output_10*0.0659216)+
(perceptron_layer_1_output_11*-0.724673)+ (perceptron_layer_1_output_12*0.172028)+
(perceptron_layer_1_output_13*0.0997577)+ (perceptron_layer_1_output_14*-0.503945)];

perceptron_layer_3_output_0 = [-0.874511 + (perceptron_layer_2_output_0*1.15473)+
(perceptron_layer_2_output_1*0.29924)+ (perceptron_layer_2_output_2*0.798893)+
(perceptron_layer_2_output_3*-1.28086)+ (perceptron_layer_2_output_4*-0.587111)+
(perceptron_layer_2_output_5*-0.453524)+ (perceptron_layer_2_output_6*1.1361)+
(perceptron_layer_2_output_7*1.00465)+ (perceptron_layer_2_output_8*-0.222842)+
(perceptron_layer_2_output_9*-0.773392)];
perceptron_layer_3_output_1 = [-0.0795494 + (perceptron_layer_2_output_0*0.61723)+
(perceptron_layer_2_output_1*-0.436573)+ (perceptron_layer_2_output_2*0.419307)+
(perceptron_layer_2_output_3*-0.0486632)+ (perceptron_layer_2_output_4*-0.177654)+
(perceptron_layer_2_output_5*-0.0771434)+ (perceptron_layer_2_output_6*0.612371)+
(perceptron_layer_2_output_7*0.388196)+ (perceptron_layer_2_output_8*-0.125711)+
(perceptron_layer_2_output_9*1.3535)];
perceptron_layer_3_output_2 = [-0.068214 + (perceptron_layer_2_output_0*-0.160699)+
(perceptron_layer_2_output_1*0.326086)+ (perceptron_layer_2_output_2*-1.99688)+
(perceptron_layer_2_output_3*1.02411)+ (perceptron_layer_2_output_4*0.0373337)+
(perceptron_layer_2_output_5*0.0932715)+ (perceptron_layer_2_output_6*0.938757)+
(perceptron_layer_2_output_7*0.349139)+ (perceptron_layer_2_output_8*0.875471)+
(perceptron_layer_2_output_9*-0.227882)];
perceptron_layer_3_output_3 = [0.38366 + (perceptron_layer_2_output_0*0.3724)+
(perceptron_layer_2_output_1*1.62623)+ (perceptron_layer_2_output_2*-0.317544)+
(perceptron_layer_2_output_3*-0.506848)+ (perceptron_layer_2_output_4*-0.0947874)+
(perceptron_layer_2_output_5*-0.0532409)+ (perceptron_layer_2_output_6*0.0571476)+
(perceptron_layer_2_output_7*-0.290821)+ (perceptron_layer_2_output_8*0.997162)+
(perceptron_layer_2_output_9*0.286679)];
perceptron_layer_3_output_4 = [-0.502993 + (perceptron_layer_2_output_0*-1.636)+
(perceptron_layer_2_output_1*0.0326612)+ (perceptron_layer_2_output_2*0.290805)+
(perceptron_layer_2_output_3*0.219077)+ (perceptron_layer_2_output_4*0.284986)+
(perceptron_layer_2_output_5*-0.0688725)+ (perceptron_layer_2_output_6*-0.237891)+
(perceptron_layer_2_output_7*1.40269)+ (perceptron_layer_2_output_8*-0.00362269)+
(perceptron_layer_2_output_9*0.133773)];
perceptron_layer_3_output_5 = [-0.252238 + (perceptron_layer_2_output_0*0.116763)+
(perceptron_layer_2_output_1*-0.0205817)+ (perceptron_layer_2_output_2*-0.949327)+
(perceptron_layer_2_output_3*-0.930831)+ (perceptron_layer_2_output_4*0.14604)+
(perceptron_layer_2_output_5*-0.270317)+ (perceptron_layer_2_output_6*-1.38478)+

(perceptron_layer_2_output_7*0.423476)+ (perceptron_layer_2_output_8*-0.481026)+
(perceptron_layer_2_output_9*0.0522649)];
perceptron_layer_3_output_6 = [0.0682961 + (perceptron_layer_2_output_0*0.326936)+
(perceptron_layer_2_output_1*1.89607)+ (perceptron_layer_2_output_2*-0.544361)+
(perceptron_layer_2_output_3*-0.563213)+ (perceptron_layer_2_output_4*0.489797)+
(perceptron_layer_2_output_5*0.368514)+ (perceptron_layer_2_output_6*0.502648)+
(perceptron_layer_2_output_7*-0.0591276)+ (perceptron_layer_2_output_8*-0.742663)+
(perceptron_layer_2_output_9*0.249041)];
perceptron_layer_3_output_7 = [-0.0435656 + (perceptron_layer_2_output_0*-0.48458)+
(perceptron_layer_2_output_1*0.134001)+ (perceptron_layer_2_output_2*-0.0334211)+
(perceptron_layer_2_output_3*0.40259)+ (perceptron_layer_2_output_4*0.164364)+
(perceptron_layer_2_output_5*-0.386075)+ (perceptron_layer_2_output_6*0.953877)+
(perceptron_layer_2_output_7*0.773478)+ (perceptron_layer_2_output_8*-1.51577)+
(perceptron_layer_2_output_9*0.651387)];
perceptron_layer_3_output_8 = [0.214984 + (perceptron_layer_2_output_0*-1.77644)+
(perceptron_layer_2_output_1*-0.460648)+ (perceptron_layer_2_output_2*-1.11863)+
(perceptron_layer_2_output_3*-0.719199)+ (perceptron_layer_2_output_4*0.125237)+
(perceptron_layer_2_output_5*0.0613257)+ (perceptron_layer_2_output_6*1.37642)+
(perceptron_layer_2_output_7*-0.127539)+ (perceptron_layer_2_output_8*-0.413662)+
(perceptron_layer_2_output_9*-0.140022)];

ALCR_H1=
unscaling_layer_output_0 = perceptron_layer_3_output_0*(786.8939819-0)/(1+1)+0+1*(786.8939819-
0)/(1+1);
ALCR_M1=
unscaling_layer_output_1 = perceptron_layer_3_output_1*(1779.189941-0)/(1+1)+0+1*(1779.189941-
0)/(1+1);
ALCR_L1=
unscaling_layer_output_2 = perceptron_layer_3_output_2*(1898.599976-0)/(1+1)+0+1*(1898.599976-
0)/(1+1);
LONG_H1=
unscaling_layer_output_3 = perceptron_layer_3_output_3*(402.519989-0)/(1+1)+0+1*(402.519989-
0)/(1+1);
LONG_M1=
unscaling_layer_output_4 = perceptron_layer_3_output_4*(412.0960083-0)/(1+1)+0+1*(412.0960083-
0)/(1+1);
LONG_L1=
unscaling_layer_output_5 = perceptron_layer_3_output_5*(387.8299866-0)/(1+1)+0+1*(387.8299866-
0)/(1+1);
TRAN_H1=
unscaling_layer_output_6 = perceptron_layer_3_output_6*(613.5440063-0)/(1+1)+0+1*(613.5440063-
0)/(1+1);
TRAN_M1=
unscaling_layer_output_7 = perceptron_layer_3_output_7*(1397.579956-0)/(1+1)+0+1*(1397.579956-
0)/(1+1);
TRAN_L1=
unscaling_layer_output_8 = perceptron_layer_3_output_8*(761.5599976-0)/(1+1)+0+1*(761.5599976-
0)/(1+1);